PHASE SELECTION AND MEASUREMENT IN A SUPERCONDUCTING CYCLOTRON

By

James Donald Bailey

A DISSERTATION

Submitted to
Michigan State University
in partial fulfillment of the requirements
for the degree of

DOCTOR OF PHILOSOPHY

Department of Physics and Astronomy

1994

ABSTRACT

PHASE SELECTION AND MEASUREMENT IN A SUPERCONDUCTING CYCLOTRON

By

James Donald Bailey

Phase selection hardware has been installed in the K1200 superconducting cyclotron. These phase slits have successfully selected a beam pulse with a single peak of FWHM of 2.4° in RF phase, from an initial pulse of FWHM of 14.1° in RF phase. This reduced pulse transmitted 20% of the unreduced internal beam current. An internal Si PIN diode detector has been developed to measure the beam time spectrum. This timing probe was installed and successfully tested in the K1200. A phase selection simulation was developed using the MSU/NSCL orbit integration codes MYAXIAL, INFLECTOR, and Z3CYCLONE. The simulation began in the axial injection line ~3 m below the K1200 median plane. Details of the phase selection which were measured with the internal timing probe were reproduced by the simulation. Aspects of injection and acceleration were explored and related to phase selection, with suggestions made for future improvements in the phase selection hardware.

To my parents,

Floyd & Sally Bailey,

in gratitude for

their love and moral support.

ACKNOWLEDGEMENTS

I would like to express my gratitude for Jerry Nolen, for his guidance, support, and friendship, and for taking me on as his student. I am deeply gratefull for Felix Marti, who trained me in the details of the MSU cyclotron codes, and assisted me throughout these studies, his friendship and motivation was invaluable. I am also thankfull for Henry Blosser and Mort Gordon, for their having trained me in Accelerator Physics.

This project required the assistance of much of the staff of the National Superconducting Cyclotron Laboratory, all of whom deserve my thanks. Especially John Yurkon and Dennis Swan, for their assistance with detectors and electronics, John Kuchar and Jack Ottarson for their work in designing the phase slits and timing probe, and the entire operations staff, who have assisted and trained me in the operation of the K1200.

This work was supported by the National Science Foundation through the National Superconducting Cyclotron Laboratory. They, together with the College of Natural Sciences and the Physics and Astronomy Department at Michigan State University, have financially supported my graduate career.

Finally, I would like to give my thanks and appreciation for my wife, Kitty. Thank you for your support, encouragement, and motivation.

TABLE OF CONTENTS

LIST OF TABLES

LIST OF FIGURES

CHAPTER 1

INTRODUCTION

1.1 AN INTRODUCTION TO THE K1200 CYCLOTRON

The K1200 cyclotron, built at the National Superconducting Cyclotron Laboratory at Michigan State University by H. Blosser, who led the design, construction, and inauguration[1], has been operated for Nuclear Physics research since 1988[2]. The K1200 has proven itself a versatile and reliable accelerator[3]. Beams as light as a hydrogen molecule, and as heavy as uranium have been extracted with energies as low as 18 MeV/u ($^{20}Ne^{3+}$), and as high as 200 MeV/u ($^{16}O^{8+}$ on 2/2/94[4, 5].) This work is a study of the time and energy aspects of single particle dynamics in the K1200 cyclotron, with a goal of providing improved beam quality, and is a continuation of studies done by Milton at MSU/NSCL with the K500 cyclotron[6, 7, 8], the world's first operating superconducting cyclotron.

Michigan State University's K1200 cyclotron is a compact, isochronous cyclotron with superconducting main coils. The use of two split main coils, together with 21 independent trim coils per hill, allows for the production of isochronous fields over a range of $3 - 5$ Tesla for many different q/m's, and final energies. To be isochronous $\omega = qB/m$ must be constant, so $B_z(r)$ must be approximately γB_0, where γ is the relativistic mass increase $m = \gamma m_0$. The median plane cross-section is depicted in Figure 1.1. Three spiral shaped pole tips, or hills, produce an azimuthally varying

field, which provides vertical focusing, except in the center. Acceleration is achieved with three spiral shaped dees located in the valleys between hills, which operate between $9 - 27$ MHz. The final velocity is a function of charge to mass, magnetic field and radius, often expressed as a bending limit on the final energy, $E/A = K_b(Q/A)^2$, with a K_b value of 1200 MeV for the K1200 cyclotron. The extraction radius is approximately 1 m. A second limit comes from focusing capabilities, and is expressed as $E/A = K_f(Q/A)$, with $K_f = 400$ MeV. Hence the maximum achievable energy of 200 MeV/u is focussing limited with $Q/A = 0.5$[2].

The cyclotron is currently operated in first harmonic mode with on-axis injection through a spiral inflector to fixed central region electrodes which are depicted in Figure 2.4. Three Electron Cyclotron Resonance Ion Sources (ECR's) are operated as external sources, providing the wide range of ion's and charge states mentioned above. The injection, inflection, and acceleration voltages are adjusted to obtain the same orbit path through the central region electrodes for every ion[2, 9]. Centering of orbits is achieved through a first harmonic magnetic field bump applied with trim coil 1 as the beam initially crosses the radial focussing resonance, $\nu_r = 1$, [9]. Precessional extraction is used, with trim coil 21, producing a first harmonic bump near the second and final crossing of the $\nu_r = 1$ resonance. The beam is then separated with an electrostatic deflector and guided through the yoke with electrostatic and magnetic channels[10, 11]. Between injection and extraction, the beam traverses approximately $750 - 800$ turns. The $\nu_r - 2\nu_z = 0$ difference resonance, coupling the transverse planes of motion, must also be crossed, usually before extraction, but the force is amplitude dependent, so with good beam centering, it is not a problem. The typical unbunched acceptance of the cyclotron is 10% of the current entering the spiral inflector, with the buncher tripling the injected current. Total transmission from the 90 deg. charge selection magnet, following the ECR's,

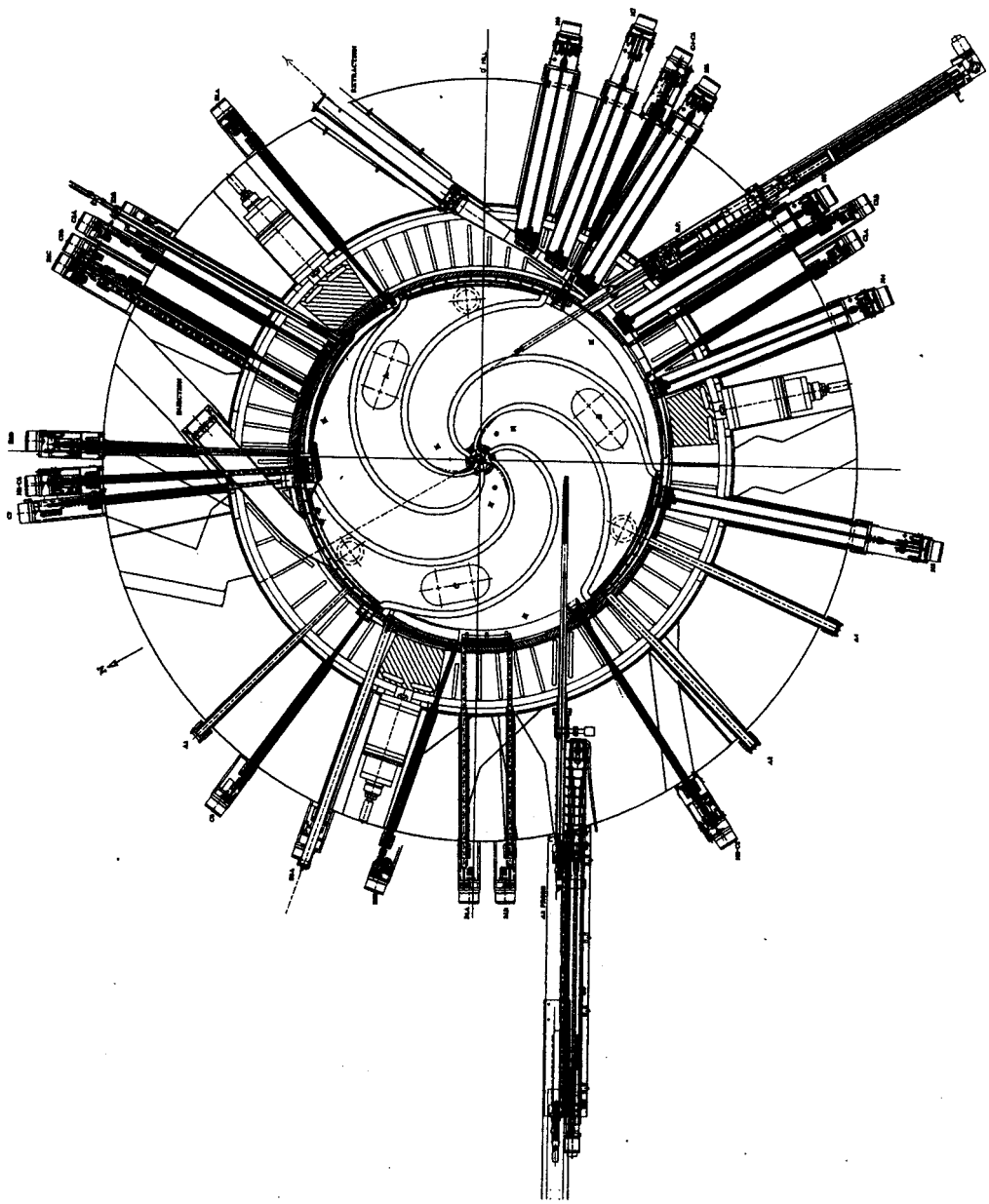

Figure 1.1: K1200 Median Plane Overview.
The K1200 median plane is depicted with extraction elements and probes. The spiral dees are marked with 'racetracks', where the dees are coupled to the dee stems. The A2 (lower right quadrant) and A5 (upper right quadrant) probes have been drawn fully inserted above grounded pole-tips, or hills. The central region detail can be seen in Figure 2.4. The two circles, just to the right, and closest to the central region, are the locations of the phase slits.

through extraction averages 1.4% with a high of 11.3%. Extracted currents range from highs of ~200 pnA (particle nano-Amps) down to sub ppA, primarily from production rates of the particular charge state in the ECR sources[12].

1.2 MOTIVES FOR REDUCING THE PHASE SPREAD

There has been a constant stream of accelerator improvements over the years. From Lawrence's first cyclotron, the world has seen a host of different types of cyclotrons, betatrons, synchrotrons, synchro-cyclotrons, and linacs, with uses from molecular through elementary particle physics, and applications in medicine, carbon-dating, wear analysis, and the production of semiconducting devices and ultra-fine filters. The use of computers has greatly facilitated many of these developments, but studies done on computers, just like experiments done on individual machines, are device dependent. This makes it difficult to generalize the results, and even when general results are derived, simulations are often necessary to implement these results on new machines.

For cyclotrons, one such development achieved in the 1960's, was the introduction of slits to remove all but a very narrow pulse of particles in time. The improved understanding of particle orbits provided by computer simulations in the central region demonstrated couplings between radial[13] (and sometimes axial[14, 15]) motion, and the particles time with respect to the accelerating RF voltage. (Commonly referred to as RF phase. Unless explicitly denoted otherwise, the word phase will refer to the RF phase of particles inside the machine.) One of the first groups to use this new technique was MSU, with their K50 cyclotron[13]. A phase dependent centering effect was exploited, with the computer finding the locations of maximum radial spread for both a parallel orbit which was initially displaced in r, and an

initially divergent orbit which was started on the same point. Then with two slits inserted, one for each of those locations, the phase width was reduced from a FWHM of 23° RF to 1.4° RF (3.4 ns to 0.2 ns)[13]. It is important to note that maintaining these cuts requires stable frequency, voltages, and magnetic fields.

By itself, this type of reduction is highly useful for experimenters using the Time-of-Flight (TOF) technique for energy measurement. The reduced duty cycle provides better intrinsic resolution, in the same manner that a smaller spot provides better resolution in a spectrograph. But it also permits the achievement of single-turn extraction[16]. With the remaining beam centered, the radius of a particle is energy dependent, but the energy is phase dependent. The spot size is reduced, permitting separation of turns with precessional extraction. 100% of the beam is then extracted[13], greatly reducing the activation of parts inside the machine, and removing the power dumped on extraction elements. Furthermore, this reduced energy spread permits precision measurements of energy levels, such as those found in nuclear bound states[17]. These precision beam characteristics were then made optional, in that the slits could be removed, allowing the experimenter to select the beam characteristics most suitable for the particular experiment.

It is also important to note that these advances in Accelerator Physics were also associated with advances in diagnostic instrumentation, particularly the differential probe to measure precessional effects and turn separation[18, 14]. A common method to measure phase is the capacitive pickup, a non-intercepting probe that measures currents associated with image charges produced by the beam. While the first harmonic of the accelerating frequency is swamped by the RF pickup, the higher harmonics left by the beam pulse can be used to give the beam phase[19, 20]. These non-intercepting probes need intense beam bunches, but recent advances have worked with 10 nA currents[21]. Phase spectra are often measured externally with

such devices as multi-channel plates to see electrons or x-rays produced by the beam[20, 22], and BaF detectors or fast plastics to see γ-rays or other secondary beam products[13, 21]. Measuring phase structure internally is more difficult.

1.3 EARLIER PHASE STUDIES

Collins continued the study of mechanisms producing the phase cuts in the K50 cyclotron, finding phase dependent centering and energy gain effects both contributing to the cuts. He also showed in his simulations that the magnitudes of each of these effects varies in machines with different basic characteristics such as the number of hills and the electric fields in the central region[23].

At this point it will be appropriate to review a few basic equations pertaining to acceleration inside a cyclotron. In each gap, an ion will see an accelerating voltage $V_{Dee_i} \sin(\omega_{RF} t + \Phi_i)$. To accelerate an ion, the voltage on a Dee must go from negative to positive while the particle is traversing that Dee. Thus, with all the Dee voltages held to the same value, the maximum voltage seen in one revolution is

$$V_0 = 2V_{Dee} N_{Dee} \sin \frac{hD}{2}, \tag{1.1}$$

with N_{Dee}, the number of Dees, D, the azimuthal width of the Dees, and h, the harmonic number of the cyclotron resonant frequency at which the accelerating voltage is operated, defined by $\omega_{RF} = h\omega_0$. The kinetic energy gain per turn is then

$$\frac{dE}{dn} = qV_0 \cos\phi, \tag{1.2}$$

where q is the particle's charge, and ϕ is the position, or phase, of the particle with respect to the RF accelerating voltage, with $\phi = \langle \omega_{RF} t - h\theta \rangle$ averaged over many gap crossings[24]. This ϕ is designed such that the earlier a particle arrives at a azimuth, the more negative is its value of ϕ, while later particles are more positive.

In an isochronous cyclotron then, for particles within the same turn, with small $\Delta\phi$,

$$\frac{\Delta E}{E} \simeq -\frac{(\Delta\phi)^2}{2}, \tag{1.3}$$

and,

$$\Delta R \simeq \frac{m}{q^2 \bar{B}^2 R}\Delta E. \tag{1.4}$$

When $B(r)$ is not perfectly isochronous, the phase of a particle changes according to

$$\frac{d\phi}{dn} = 2\pi h\left(\frac{\omega_{RF}}{h\omega} - 1\right) = 2\pi h\left(\frac{B_0 - B}{B}\right) = 2\pi h\Omega(E). \tag{1.5}$$

Combining dE/dn and $d\phi/dn$, one can solve for ϕ as a function of E

$$\sin\phi(E) = \sin\phi_0 + \frac{2\pi h}{qV_0}\int_{E_0}^{E}\Omega(E)dE. \tag{1.6}$$

Now ΔE has a first order component[23]

$$\Delta E_n = -(\Delta\phi)\int_{E_0}^{E}\sin\phi dE. \tag{1.7}$$

This is the cause of the E-ϕ correlation that Collins found. The top graph in Figure 1.2 shows an azimuthally averaged magnetic field in the median plane of the K1200 cyclotron as a function of radius. This magnetic field is that of our 'standard' operating point, which is used to start the machine after a long shutdown, and is often used in orbit studies. Overlaid on this field is the isochronous field for the same operating point. The deviations from isochronism result in the $\sin(\phi)$ curve shown in the lower half of the graph, which was calculated with Equation 1.6.

The phase dependent centering correlation is produced by the time dependent accelerating voltage[25]. When particles enter gaps with different times, they are

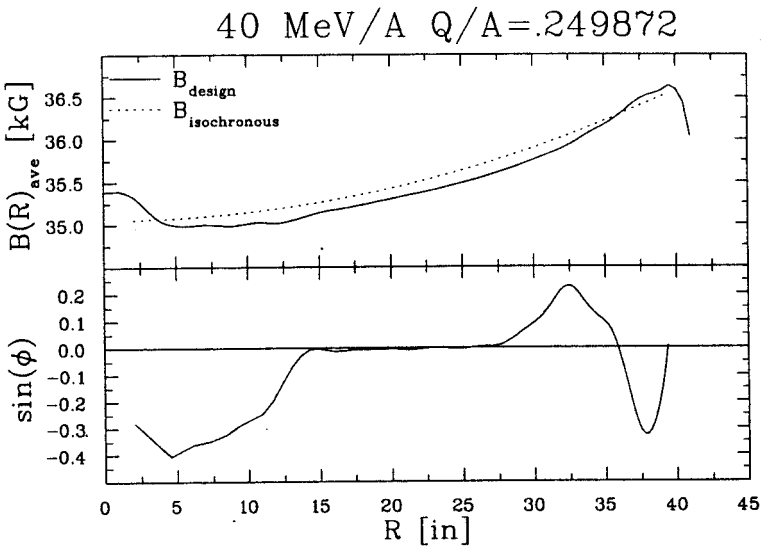

Figure 1.2: $B(r)$ and $\sin(\phi)$ for the 'Standard' Operating Point.
The median plane magnetic field for the 'standard' operating point, and the isochronous field for that operating point. Note the central cone, used to bring down the initially high values of ϕ. Also note the roll off at the edge, where the magnetic field starts to fall to zero, and the second $\nu_r = 1$ crossing occurs. Here, a first harmonic magnetic 'bump' forces the beam to precess, increasing the radial separation at extraction. The $\sin(\phi)$ curve resulting from these deviations from isochronism, see Equation 1.6, is shown in the lower graph. The field is trimmed so that at extraction, $\int \sin(\phi) dE = 0$, for $\sin(\phi) = 0$.

accelerated by different amounts, displacing their orbit centers differently. This effect is more significant when the velocities of the affected particles are lower. As this effect accumulates, and the particle orbits precess, places can be found with r-ϕ correlations. The two r-ϕ correlations are cumulative, adding to or canceling each other.

The K500 presented new complications, with higher magnetic fields reducing the size of the central region. Also the strong spiral of the hills, with smaller gaps between pole faces restricted access to the central region. Vertical holes had been drilled in the yoke at 7 in. radius, and Milton explored using these locations to cut the phase. The position of the holes was determined by machine constraints such as finding room amongst trim coils, current leads, and dee stems[6]. SOMA, a second order matrix algorithm, was developed to include non-linear effects in

the computer simulations[26]. And new techniques were explored to measure the particle phases[7].

What Milton found is that a pin inserted into the beam can simulate a slit by removing particles with greater radii as the beam pulse is first intercepted by the pin, then on the following turn removing the particles with lower radii. Essentially he was using the phase dependent energy gain effects to make his cuts with two slits placed 120° apart to increase the chance that one will be away from the crossover region due to centering. In practice, the two slits, each off-centered on a rotatable shaft, combined with a coarse central region cut, made it possible to limit the RF phase width to 4° FWHM[8]. The studies that were made on the K500 were made difficult by the need to continually correct the machine's drifting away from a good tune. (Being the world's first super-conducting cyclotron, much was learned in operating the K500 that was used to improve the design and operation of Texas A&M's K500 and MSU's K1200 super-conducting cyclotrons.)

Measuring the internal phase in the more compact and enclosed K500 cyclotron was a difficult challenge. The spiral of the hills meant that the internal probes were only visible through the viewing ports over a small radial range. The higher energies to which the K500 accelerated heavy ions, together with beam losses at these energies created a bright γ-ray background which swamped signals from the beam. To overcome these difficulties, a PIN diode was inserted immediately behind the probe head, which intercepted the beam[7, 8]. This detector was radiation and temperature sensitive, and was sometimes swamped by ions, which stripped of more charges by the probe, returned to strike the detector itself, but it was useful for studying the use of the slits. Ronningen continued the search for a more robust detector system, exploring avalanche diodes[27], but these studies were interrupted by the changeover from the K500 to the K1200 cyclotron.

1.4 MOTIVES FOR K1200 PHASE STUDIES

The K1200 is basically a larger version of the K500. Its extraction radius is 101.2±1.7 cm[11, 28], instead of 67.5±.5 cm[29]. They both have the same range of central magnetic fields, B_0 = 3 T to 5 T, though the pole tip gap is also slightly larger, 7.62 cm instead of 6.35 cm[30, 31]. Since the spiral on the hills is approximately the same as in the K500, the greater radius of the K1200 makes access to the center of the machine even more difficult. However, the dee stems are also further out, leaving more room on the cap for drive mechanisms and phase slit installation. The central region designs are basically the same, with interchangeable spiral inflectors, though the K1200 central region was rebuilt to operate at lower dee voltages[3]. As mentioned earlier, the design of the K1200 took advantage of experience with the K500, with the result being that it is much more stable. Finally, the vertical access holes in the yoke were machined at the same radius as in the earlier machine.

In summary then, the center of the K1200 has the same basic functionality as the K500, and slits can be installed which will function in a similar fashion. Even though the slits won't function exactly the same way, because of small differences in B(r), voltage gain per turn, and the central region, the stability of the K1200 will allow a more detailed study of these slits. The greater extraction radius though makes single-turn extraction more difficult, and limits measurements to long distances from the slits.

The basic improvement that has been made in computers over the years is raw speed and computing power. There are now programs to calculate 3-D electric and magnetic fields, and ray-tracing orbits is no longer prohibitively expensive or time consuming. The following studies use ray-tracing to study the single particle motion through the inflector to the slits, since injection through a spiral inflector involves

non-linear coupled motion between the transverse planes of motion[32].

There being no existent timing detectors for the K1200 a new detector was developed to provide clean internal time spectra for the cyclotron beam. Together with computer simulations, this detector enables the study of the time and energy aspects of acceleration in the same way that the internal TV probe has shown detailed aspects of the $\nu_r = 2\nu_z$ Walkinshaw resonance[33, 34].

1.5 CHAPTER SUMMARIES

Chapter 2 develops the initial conditions which will be used in subsequent calculations. Source conditions, injection line characteristics, and central region geometry are described so that reasonable starting conditions and necessary approximations can be developed. Descriptions of the programs used in simulating K1200 operation are presented. Then the chapter finishes with an exploration of the K1200 acceptance.

Chapter 3 presents the use and testing of a Si PIN diode to directly measure the time spectra of a beam. Included are descriptions of the necessary electronics and the data collection and display routines developed for on-line use. A simulation of detector response closes the chapter, demonstrating understanding of its use. It then describes the modifications necessary to use such a detector as an internal beam phase probe. The implications of overlapping turns inside the machine are followed to their effects on the measured phase spectra, including the deleterious effects of off-centered beams. Also described are the effects of RF pickup as the probe approaches a dee, and the variation of signal strength with ion type and energy, and the resulting limits on the effective use of this detector. The effectiveness of the timing probe is demonstrated by measuring the phase curve followed by the beam,

with comparisons to curves calculated from design magnetic fields.

Chapter 4 furthers the understanding and use of 'Milton' type phase slits in the K1200 Minor improvements incorporated in the slit design and installation are presented. Then clean spectra measured with the timing probe, the improved performance of the K1200 cyclotron, and advances in computing speed are taken advantage of in understanding and exploring the use of these slits. Finally, it explores the modification of the magnetic field to control the energy dependent phase - radius correlation.

Chapter 5 presents extraction measurements using the timing probe and slits, and simple conditions necessary for single turn extraction. It then summarizes the results obtained in this study and suggests possible courses to take for further improvements in K1200 beam quality.

CHAPTER 2

INITIAL CONDITIONS

In searching for a reasonable simulation of the K1200 internal beam for use in modeling the phase slits, the realization was made, that an understanding of the injection process would be necessary. Simulations starting immediately after inflection into the central region, while useful[8, 35], leave out possible effects from the spiral inflector's coupling of the injection phase space coordinates. Also, transmission into and through the central region proves to be aperture limited by both the inflector, and the central region electrodes[9, 36]. Central region calculations alone, then, have a greater uncertainty as to whether the selected phase space is reasonable, or even physically possible. Starting before injection also allows simulations of the buncher, which include the time dependent effects of traversing the magnetic yoke, and the spiral inflector[9, 36].

The beginning of the vertical injection line, ~3 m below the cyclotron midplane was chosen as a reasonable starting point for these calculations. It is sufficiently removed to include both the yoke and the buncher, yet not so far as to divert the cyclotron timing study into an ECR to cyclotron emittance matching study. And the beam is DC at this point.

2.1 INJECTION SETUP, AND APPROXIMATIONS

Figure 2.1 shows the layout of the injection lines leading from the ECR's to the cyclotrons. Any of three different ECR's can be connected to the K1200 or the K500 cyclotrons. Each extracts downward, followed by a 90° analyzing magnet. In two of the three extraction lines, before the analyzing magnets, are focussing solenoids with slits that perform a crude selection on the charge to mass ratio (q/m). The analyzing magnets then perform a fine selection on q/m. All ions with the correct q/m are then transported through the injection line to a point below the cyclotron where a second 90° bending magnet guides them up the cyclotron axis to the spiral inflector.

2.1.1 Ion Sources

Xie's study on the extraction from the NSCL RT-ECR ion source[37] (room temperature) showed that it is space charge limited with low neutralization. This ECR has a focussing solenoid before the analyzing magnet, The spread in the beam envelope, caused by the space charge forces, completely fills the solenoid aperture, sampling both the spherical and solenoid aberrations of the solenoid, and causing an effective growth in the beam emittance[38]. This has been corrected in the NSCL SC-ECR (superconducting) by moving the solenoid closer to the source. The NSCL CP-ECR (compact) is closer to its analyzing magnet, and does not have a focussing solenoid before the analyzing magnet. The analyzing magnets will also distort the beam if the beam envelope is too large, so the solenoids are used to move the beam waist closer to the bending magnets. Xie showed that the emittance, before this growth

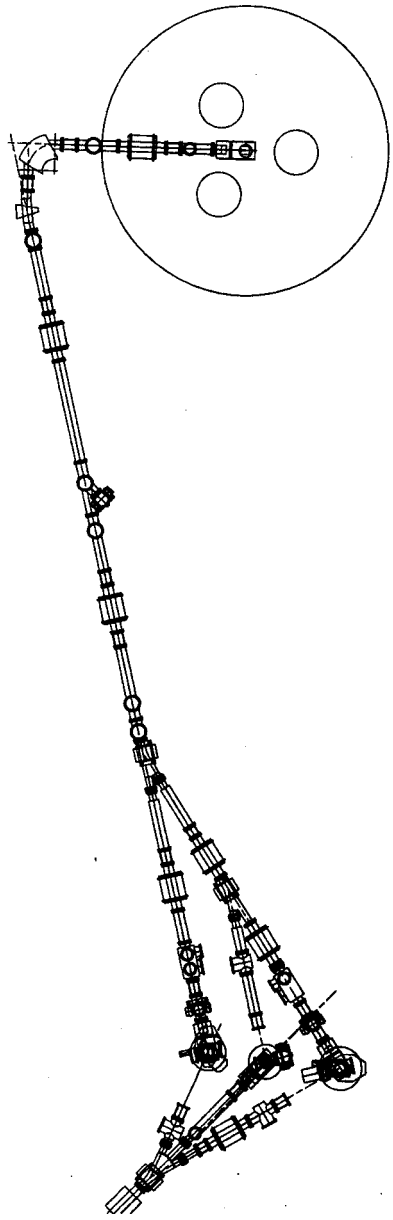

Figure 2.1: ECR Switch Yard and K1200 Injection Line.
The injection line from the ECR sources to the K1200 cyclotron is shown above. The analyzing magnets are directly below the ECR's. Solenoids are used to provide focusing.

occurs, is

$$\epsilon = \left|\frac{p_{\theta_f}}{p_z}\right| = r_a \left[\left(\frac{T_i}{2QV_{ECR}}\right)^{1/2} + A_{\theta_a}\left(\frac{Q}{2MV_{ECR}}\right)^{1/2}\right] \tag{2.1}$$

where A_{θ_a} is the azimuthal component of the vector potential at radius r_a in the extraction aperture, V_{ECR} is the extraction voltage, and T_i, Q, and M are respectively, the ion temperature (typically a few eV $\times$ Q), charge, and mass. Thus the unnormalized beam emittance can be 50 to 400 π mm·mrad after analysis[37].

Understanding injection line transmission after the analyzing magnet has been left to further studies. The analyzing magnet selects all but one charge to mass ratio of the ions extracted from the ECR, reducing the intensity of the beam. It is important to note, that attenuators have been installed in this part of the beam line[39]. They can be used to reduce the beam intensity by greater than 6 orders of magnitude. Their placement ensures that reductions in intensity are not accompanied by changes in the phase space of the beam, except for any subsequent space charge effects. The beam intensity drops even further during injection, reducing the magnitude of any space charge effects.

With the greatest extraction current to date being ~200 pnA, the cyclotron itself is relatively free from space charge effects. Inside a cyclotron, space charge effects have been separated into two main components. The transverse component adversely affects the focussing frequencies, with the smaller vertical focussing being of prime concern. A formula estimating the limiting current for adverse vertical focussing was worked out as early as 1961 by Blosser and Gordon[40]

$$I_{lim} = b\,\epsilon_0\,\omega_0\,\nu_z^2\left(\frac{\Delta\phi}{2\pi}\right)\left(\frac{\Delta E_n}{q}\right) \tag{2.2}$$

with ΔE_n the energy gain per turn, q the charge, ω_0 the orbital frequency, $\Delta\phi$ the full phase width, b the vertical aperture, and ν_z the vertical focussing frequency of

the beam. ϵ_0 is the permittivity of free space, and all units are MKS. Note that the limit is dependent on the square of ν_z, which is smallest in the machine center, $\nu_z \sim 0.1$. More recently, a different estimate was derived by Joho to understand and increase the high intensity beams at PSI[41].

$$I_{lim} = \frac{1}{4}\left(\frac{A}{Q}\right) I_0 \beta \nu_z^2 \left(\frac{b\omega_0}{c}\right)^2 \left(\frac{\Delta\phi}{2\pi}\right) \tag{2.3}$$

Here I_0 is m_0c^2/eZ_0 with $Z_0 = 30\ \Omega$, and $\beta = v/c$. Note that now there is a dependance on the beam velocity. It can be shown that,

$$I_{lim}\ (\text{Joho}) = 2\pi N \left(\frac{\rho\, b}{\rho_f^2}\right) I_{lim}\ (\text{Blosser \& Gordon}) \tag{2.4}$$

where ρ is the average radius of curvature of the beam for one turn, N the total number of turns before extraction, and ρ_f the radius at extraction. With both being approximate estimates of a complex phenomena, the most pessimistic (Joho's) is chosen to estimate an upper bound for the K1200. For the high current beam, 25 MeV/u $^{16}O^{3+}$, $\beta = .0018$, and $\nu_z \simeq .1$ at injection, $b = 1.4$ cm, $f = 10.777$ MHz, and $\Delta\phi \approx 18°$ FWHM with the buncher on. Using these values, $I_{lim} = .37$ mA, two orders of magnitude higher than the highest current injected into the K1200 to date[12]. (It should be noted that Joho's estimate was not pessimistic enough. The $\nu_r + 2\nu_z = 4$ resonance reduced the maximum possible current by a factor of 4 from his calculation[41].)

Since this effect is not significant in the K1200 operation, experiments can be conducted at extremely low currents with the attenuators, and the resulting measurements (a study of single particle beam dynamics) will not be far from full current operation. There is one regime though where distortions of the beam bunch by space charge may be of concern. The effects of the longitudinal component will be presented in Chapter 5, where single turn extraction will be discussed.

2.1.2 Traversal of the Yoke

Figure 2.2 shows the last leg of the injection line in more detail. The first item to note is that the horizontal portion of the line requires magnetic shielding (not shown.) The magnetic field at 3 m below the midplane is sufficiently strong to deflect the ions into the pipe walls without this shielding. A 90° iron core bending magnet is used to deflect the beam upwards.

At various times, there have been different steering and focussing elements designed and/or installed in the axial injection line. Figure 2.2 shows only the naked solenoid (no iron), which is the only focussing element used in this study. The solenoid is 2.22 m below the median plane. Following the solenoid is a buncher. Designed to operate at both first and second harmonics of the RF accelerating wave, the buncher to date has only been run in the first harmonic with a sine wave driver. The accelerating gap is 7 mm between two wire grids, and the distance is 1.7 m below the median plane[9].

The last item to note in the injection line is that there is a sudden reduction of the hole radius at $z = 0.33$ m from the median plane in the iron center plug. As shown in Figure 2.3, $B(z)$ varies rapidly at this point. This rapid change in the magnetic field occurs in a distance approximately equal to the forward distance travelled during one revolution of the transverse motion. This rules out any adiabatic approximations such as the one used to describe magnetic mirrors.

2.1.3 Spiral Inflector Injection

The spiral inflector was patterned after the Grenoble spiral inflector, designed by Belmont and Pabot[42]. It has a 4 mm diameter entrance aperture, a 6 mm diameter exit aperture, and the electrodes have a 1.75 cm radius of curvature with a gap

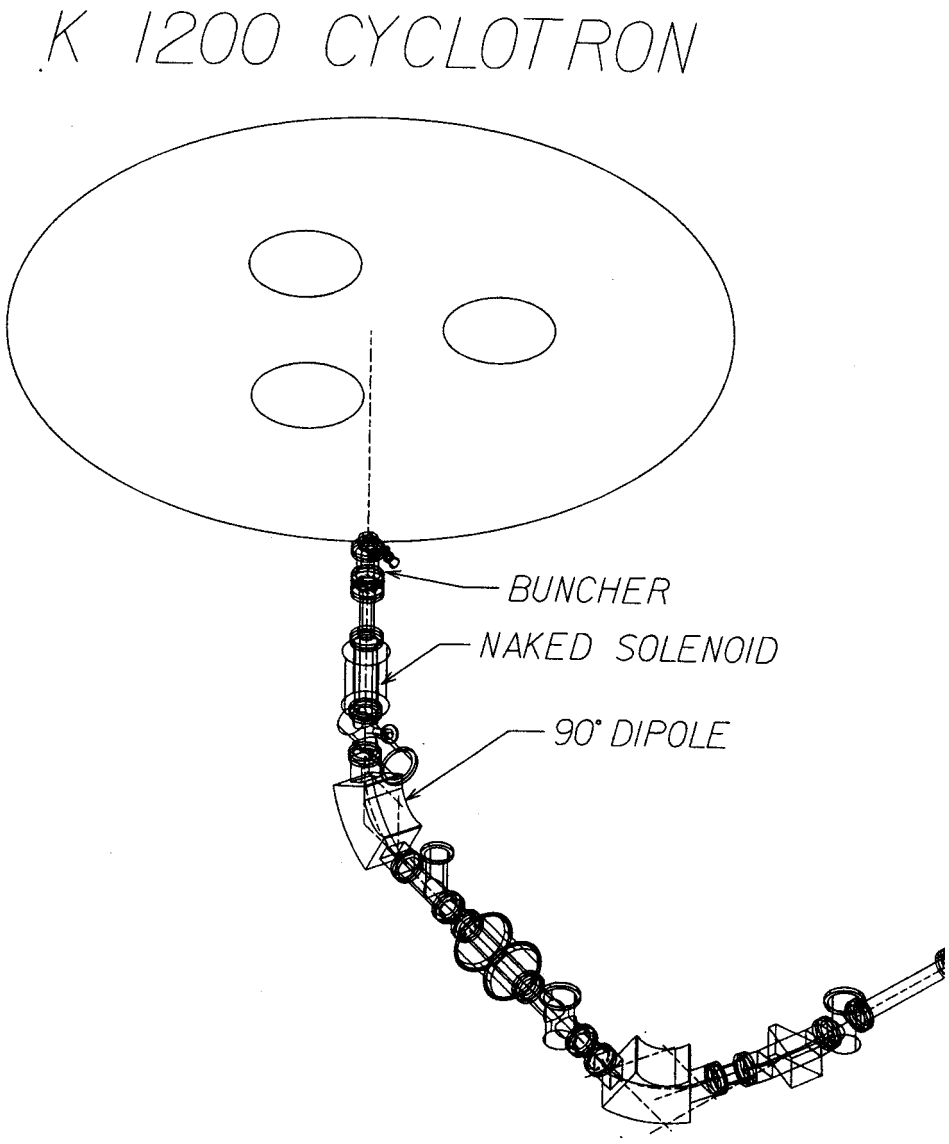

Figure 2.2: K1200 Axial Injection Line.
Portion of injection line in the K1200 vault. The axial segment is used in the injection studies to determine the initial conditions for cyclotron orbit calculations. Depicted are the buncher, focussing solenoid, and 90° bending magnet. The horizontal section preceding the last bending magnet has been magnetically shielded.

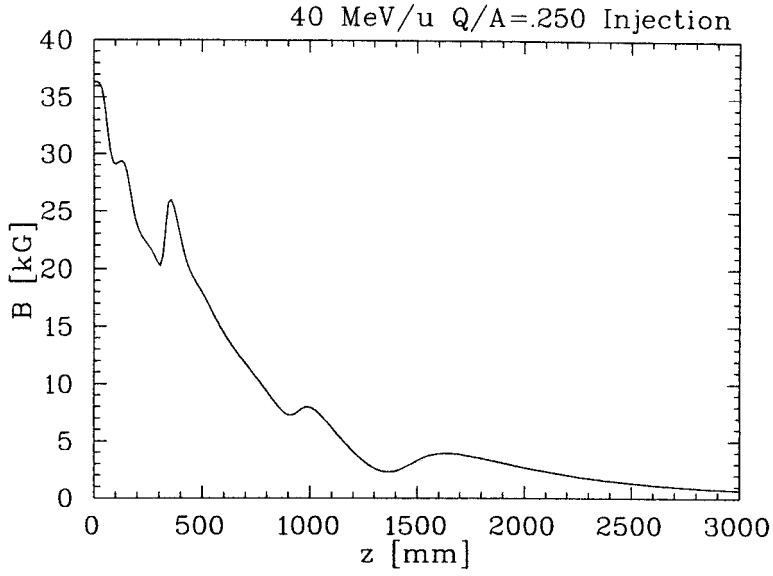

Figure 2.3: K1200 Axial Magnetic Field.
The axial magnetic field from a cylindrically symmetric calculation for the K1200 'Standard' operating point Q/A = 0.25 at 40 MeV/u. The yoke begins at 1.46 m and the center plug narrows at 0.94 m and 0.33 m. The remaining structure is caused by the reduction of iron at 0.16 m and and the opening up of the midplane from 0.08 m to 0.05 m. The rapid changes in $\vec{B}$, particularly at 0.33 m, prevent the use of adiabatic approximations.

spacing of 4 mm[9]. Baartman and Kleeven worked out an infinitesimal transfer matrix for an ideal spiral inflector[32], which unfortunately leaves out edge effects, which are significant. This study surmounts this obstacle by raytracing through an electric field which includes the fringe field.

2.1.4 Central Region Selection

The central region is depicted in Figure 2.4. The median plane electrodes are shown, together with equipotential contours for each dee. Overlaid on the potential map are central rays for starting times of 185° to 240° relative to the accelerating voltage on the first dee. A 45° range can be seen to clear the central region. Also visible is the time dependent spread of orbit centers, none of which is correctly centered at this point. The behavior of ions displaced from the central ray has been considered by

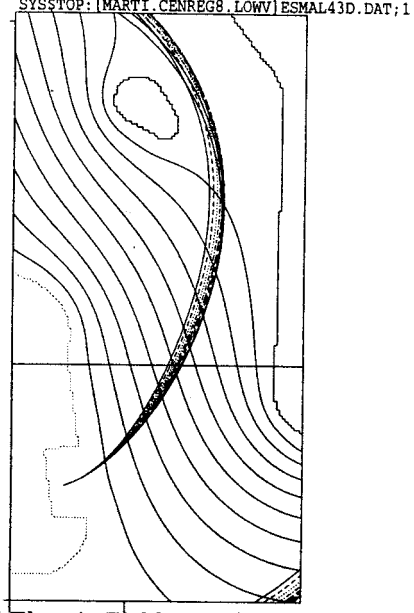

(a) Small Electric Field Map (midplane K1200 source to puller)

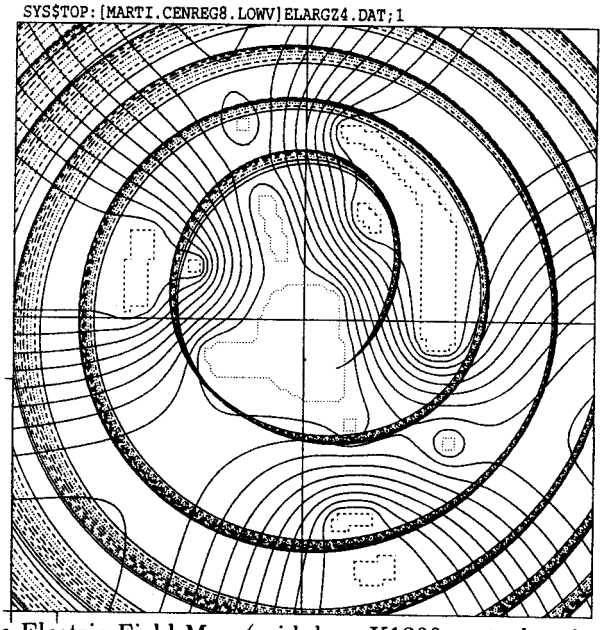

(b) Large Electric Field Map (midplane K1200 central region)

Figure 2.4: K1200 Central Region Orbits in the Low Voltage Central Region.
Central ray orbits, for starting times $\tau_0 = 185° - 240°$ in 5° steps, are overlaid on median plane cross-sections of K1200 central region equipotential maps which were created using RELAX3D. Figure 2.4(a) represents the gap between the source and the puller, measures 1.0×2.0 in^2 and is used in the first part of the orbit program Z3CYCLONE. Figure 2.4(b) is a closeup from the central region map used in the SUPERCYCLONE subroutine of Z3CYCLONE, and is 5.0×5.0 in^2. The dotted electrodes are at ground and the dashed electrodes are connected to the dees, with equipotential lines marked at 10% intervals.

Gordon and Marti[24]. They demonstrated that each particle should be associated with a central ray whose time difference from the particle is,

$$\phi = \omega_{RF}t - h\theta + h\frac{p_x}{p}\nu_r^2, \tag{2.5}$$

a correction to the ϕ used in Equation 1.2, so that each with a given ϕ will have the same energy gain per turn later in the machine. Here p_x is $p_r - p_{r_0}$, where p_{r_0} is for the reference particle or central ray, and ν_r is the horizontal focussing frequency.

Having fixed electrodes in the central region requires that beams for every operating point travel the same path in the machine. This is accomplished by selecting B_0, V_{ECR}, and V_{DEE} such that the ion in question will have the same bending radius in every case, 0.795 cm[43]. With B_0 and V_{DEE} determined by the orbit characteristics inside the cyclotron, V_{ECR} is constrained to provide the requisite energy. V_{SP} then follows, providing the correct radius of curvature in the inflector. Note that this means V_{ECR} is not a free parameter in determining the emittance of the injected beam.

2.1.5 Injection Matching

The concept of an eigen-ellipse in phase space, which maps back to itself after one complete traversal of a repetitive transport system, has been extended to cyclotrons[16], in that the particles displacement from the central ray is the coordinate system in which the map is performed. This eigen-ellipse about an accelerated equilibrium orbit is then the preferred orientation of particles in phase space for transport through the machine. Injection matching is the process of trying to match this eigen-ellipse with the injected beam. Failure means that the emittance will effectively grow as the beam samples non-linearities in the magnetic and electric fields. The choice of injection method, and the design of the central region, as well

as the availability of injection line focussing elements are the major determinants of the feasibility as well as the practicality of injection matching for a particular machine.

This study extends this concept from the transverse motion of the beam to the longitudinal or time and energy coordinates. The non-linearities of transport through the spiral inflector and central region present an extra challenge towards achieving good phase selection inside the machine.

2.1.6 A Non-Cylindrically Symmetric $\vec{B}$

One further complication must be considered before modelling injection. The iron in the injection line shielding and bending magnet attract magnetic flux of the cyclotron fringe field[2]. This causes the magnetic field immediately following the bending magnet to be asymmetric. The real magnetic field is difficult to map and to simulate. The higher the magnetic field, the closer the beam has to be steered to the inside edge of the bending magnet in order to guide it into the inflector. This study will ignore this, leaving an understanding of this effect to future injection line studies, and its removal to future modifications. The solenoid used in this study cannot be used for focussing until a solution is found where the beam can be steered through its center. The K500 cyclotron does not have this problem, and its solenoid can be used to focus the injected beam.

2.1.7 Final Choice of Initial Conditions

This study uses ray tracing through a cylindrically symmetric magnetic field, derived from an axial magnetic field calculation,

$$B_z(z,r) = B(z) - \frac{r^2}{2}B''(z) + O(r^4) \tag{2.6}$$

$$B_r(z,r) = -\frac{r}{2}\left(B'(z) - \frac{r^2}{8}B'''(z)\right) + O(r^5) \tag{2.7}$$

starting immediately after the 90° bending magnet, through the solenoid to the buncher. The buncher, when used, will use a small gap approximation

$$\delta v = \frac{qV_0}{m}\frac{2}{g_1 v_0}\sin\frac{g_1}{2\rho}\sin(\omega_{RF}t_i - \Phi_b) \tag{2.8}$$

to obtain a delta impulse for the longitudinal velocity of the beam, where v_0 is the initial velocity of the particle, ρ it's bending radius in machine center, t_i it's time of arrival at the buncher, and Φ_b the phase of the buncher with respect to the RF accelerating voltage. The ray will continue through the inflector, which is represented by potential field map from which the electric field can be calculated. The particle will be transferred into the electric field two grid points away from the map boundaries to avoid edge inaccuracies in the potential map. This requires an approximation for the effects of traversing the first part of the field,

$$v_{i_{\text{enter}}} = v_i\left(\frac{\sqrt{v^2 - v_0^2(\text{Pot}(x,y,z) - .5)\frac{V_{SP}}{V_{ECR}}}}{v^2}\right) \tag{2.9}$$

which is repeated upon leaving the electric field,

$$v_{i_{\text{exit}}} = v_i\left(\frac{\sqrt{v^2 + v_0^2(\text{Pot}(x,y,z) - .5)\frac{V_{SP}}{V_{ECR}}}}{v^2}\right). \tag{2.10}$$

Here $\text{Pot}(x,y,z)$ is the relative potential, on a scale of 0 for minimum to 1 for maximum, at the (x,y,z) of the particle as it enters (or exits) the electric field, V_{SP} is the voltage across the inflector electrodes, and V_{ECR} is the ECR extraction voltage. (The path through the electric field being unknown, all three velocity components are scaled the same, which adds a small systematic error in the path of the particles.) The final coordinates will then be transferred to a central region orbit

code program which integrates in a magnetic field, derived from a midplane map, and an electric field, derived first from two successively larger electric potential maps, see Figures 2.4(a) & subfig:cr, then after 8 turns, the electric field is represented by an impulse approximation at the gaps between dee and hill.

The initial phase space transmitted through the inflector from the starting point ~3 m below the median plane, will first be mapped. Then the intersection of 100 π mm·mrad phase spaces in x-x' and y-y' , represented on a uniform grid spaced every 2 mm and every 2 mrad (approximately 7000 particles), will be used to study the full 4-D acceptance. (100 π mm·mrad was the area initially used for the design of the inflector[43], with the initial design of the beam transport system forming a double waist immediately after the last 90° bending magnet[44].) This will then be repeated every 5° RF, mapping out the acceptance of the central region for DC beams. The buncher studies will have similar pulses spaced every 2° RF. Since the ion temperature is of the order of a few eV × q, see Section 2.1.1, and the extraction voltage is ~10 kV, the initial energy spread is ignored. Particles passing too close to electrodes will be removed, and the r and ϕ of the particles at the slit locations will be saved for simulations of the slits.

2.2 PROGRAMS USED/MODIFIED FOR THIS STUDY

The National Superconducting Cyclotron Laboratory has a number of programs for use in designing and simulating various components of the cyclotron. The following are those used in this study.

MONSTER[45] is a multi-function program written in house for the creation of operational settings to be used when running the K1200 cyclotron. At its root is a collection of measured K1200 median plane magnetic field maps. Added to these

are charge sheet trim coil approximations (since at 3 T the iron is saturated), bar fields for every magnetic element in the extraction channel, and a first harmonic bump profile for precessional extraction. Layered above these are orbit codes and display and analysis routines. The current settings for both main coils, and all the trim coils are predicted for each operating point by interpolating amongst the measured fields and superimposing the trim coils, bump, and magnetic channels. With satisfactory internal orbit characteristics, settings for all electric and magnetic extraction elements are determined by first optimizing the precessional extraction, then tracing extracted orbits through the elements. This program has proven very successful in predicting operating set points greatly reducing tuning time for the operators. The magnetic fields designed with MONSTER can be saved and stored for use in other lab orbit codes. All cyclotron midplane magnetic fields used in this study have been created by MONSTER. MONSTER has also been used to obtain some non-standard field settings, such as those used in the phase curve studies in Section 3.3.

POISSON[46, 47], a code written at Lawrence Berkeley Laboratory to create 2-D magnetic fields, and now maintained at Los Alamos National Lab[48], has been used to obtain axial magnetic fields for use in studying injection. Current settings for the coils are first obtained by MONSTER, then used in the original geometry used to design the magnet (obtained from Marti.)

RELAX3D[49], written at TRIUMF, is used to obtain 3-D electric potential maps for various electrode geometries. There are separate maps for the spiral inflector, the source to puller portion of the central region, and the central region extending out to 5.0 in. The orbit programs then take derivatives of the potential maps to obtain electric field strengths and directions.

Ray tracing of orbits is generally done with fourth order Runge-Kutta integration

routines. The axial injection is simulated with two ray tracing programs written by Marti at MSU[36]. Their function has partly been described in Section 2.1.7. The first, MYAXIAL, integrates the path of the particle as it goes up the axis of the cyclotron, including several possible beam line elements such as electrostatic deflectors, a solenoid, and a quadrupole. The second, INFLECTOR, integrates through the magnetic and electric fields in the spiral inflector. The two are merged together, following the same particles to the exit of the inflector, with several methods of displaying and analyzing the resultant ellipses. The author has modified these routines to include a first harmonic buncher, to stop integrating particles that hit electrodes or fail to clear apertures, and to create and run large sets of particles. The output has also been changed to facilitate the coupling of these routines to the cyclotron code.

The particles which have successfully made it through the inflector, and whose coordinates have been saved in the plane intercepting the starting point of, and perpendicular to, the central ray, are then ray traced through the central region in the program Z3CYCLONE[50]. Also written at MSU, Z3CYCLONE is a composite of three separate routines. The first integrates in the magnetic and detailed electric fields of the source to puller part of the central region, using time as the independent coordinate. The second, named SUPERCYCLONE, integrates in the magnetic and electric fields of the entire central region, using the azimuth as the independent coordinate. These two parts are added to the program SPIRALGAP, which then continues the orbit, integrating in the magnetic field and using an impulse approximation at the gaps for the electric field. The magnetic fields are derived from a map of the median plane magnetic field, and the electric fields from 3-D potential maps of the electrodes. This program has been altered in similar fashion to the MYAXIAL, and INFLECTOR programs, so that orbits intercepting electrodes are stopped,

and so that the orbits which were run through the inflector can be continued inside the cyclotron. It was necessary to force the transition from SUPERCYCLONE to SPIRALGAP to take place on the same turn, number 8, at the same hill center, the zero degree hill on the lower right side of Figure 2.4(b). The transfer needs to take place at a position where $\vec{E} = 0$ (hill and Dee centers), if not, the energy of the particle will be incorrect. Centering differences between the orbits on different spirals, shift the center of the resulting eigenellipse when that spiral is used to transfer between SUPERCYCLONE and SPIRALGAP. Otherwise the final phase space ellipse would be a composite of several different ellipse fragments, with offsets along the joints between fragments.

The slits are simulated in a separate display and analysis program written by Marti and the author. Every time an orbit intercepts the usable range of the slits, a modification to Z3CYCLONE saves the r and ϕ coordinates. The slit program then reads these coordinates, together with final ϕ coordinates of some subsequent turn. Using these coordinates, the program allows the user to interactively adjust the position of the slits with the resultant cuts displayed almost instantaneously, even when 200,000 particles are being searched. It can also display a two dimensional density plot of r vs ϕ at the slits. The program runs on VAX workstations, displayed with GKS software on any terminal using X-WINDOWS. The above results were for a VAXstation $\cdot$ 4000 $\cdot$ 90.

2.3 ACCEPTANCE OF THE CONTINUOUS (DC) BEAM IN THE K1200

The basic probe which will be used to explore transmission into the cyclotron will be a pulse of particles. All components of the injection line before the buncher are

time independent, so z of the buncher, 1.7 m from the midplane, will be where $t = 0$ for all particles. The starting position, though, will be immediately after the 90° bending magnet, 2.972 m below the median plane. Using a pulse of particles, all with the same starting time, one can see the spreading in time caused by the yoke and the spiral inflector. When studying the added time effects of the buncher and the central region, pulses with regularly spaced starting times will be used to cover the total range of useable times. For the DC portion of the studies, without the buncher and before the central region, the actual starting time is irrelevant, so one pulse is sufficient. All calculations will be done with 40 MeV/u, Q/A$\simeq$.25 'standard' set point used to start up the cyclotron, and often used in orbit calculations.

MYAXIAL is used to tune the solenoid for maximum transmission. An initial ellipse is started, and the solenoid field strength is adjusted to minimize the oscillations in the subsequent beam envelope. Figure 2.5 shows the envelopes for three field settings near this minimum, and for when the solenoid is off. Notice the abrupt change in behavior near .33 m. This is where the field from the yoke, see Figure 2.3, rapidly changes strength.

2.3.1 2-D Acceptance in Phase Space

2-D circular ellipses, with n equally spaced particles on each ellipse, were started in both x-x' and y-y' phase spaces, for each of the solenoid settings mentioned above. (Circular when x is in mm, and x' is in mrad. Ellipses will be described in this phase space with a the length of the major axis, b the length of the minor axis, and θ the clockwise rotation of the ellipse from an upright position.) The transmission for each setting, complete with coupling effects, is displayed in Figures 2.6–2.13. The radius of each circle was gradually increased until one was found where some particles were lost. Each figure shows x-x' and y-y' at the start, and x-v_x and y-v_y at

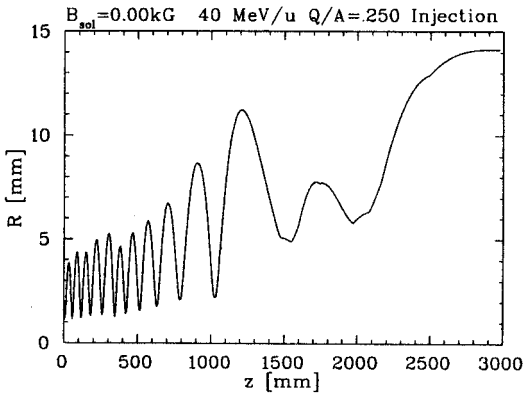

(a) Injection Envelope $B_{sol} = 0.00$ kG

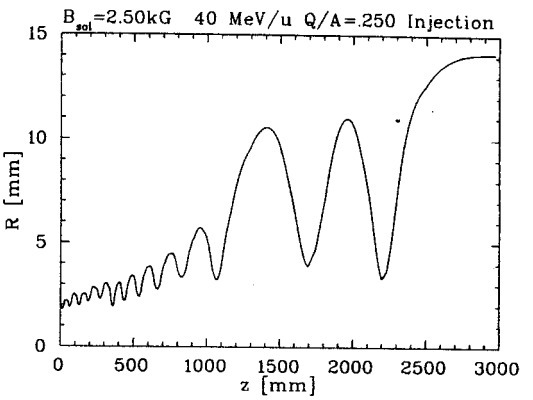

(b) Injection Envelope $B_{sol} = 2.50$ kG

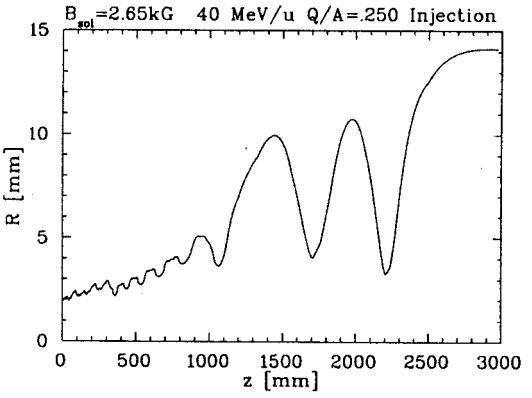

(c) Injection Envelope $B_{sol} = 2.65$ kG

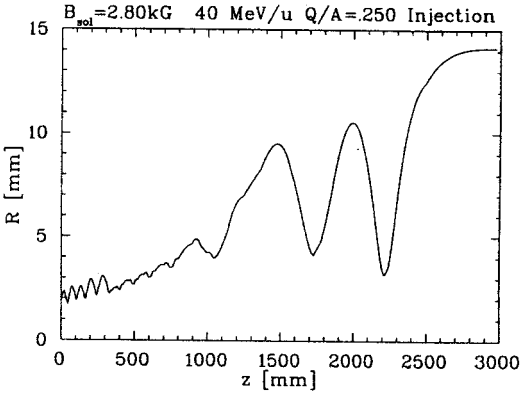

(d) Injection Envelope $B_{sol} = 2.80$ kG

Figure 2.5: Injection Beam Envelopes.
Beam envelopes for injection into the K1200 with varying solenoid strengths. Figure 2.5(c) has minimized the oscillations entering the inflector. Figures 2.5(b) & 2.5(d) are for nearby solenoid settings which are nearly as good. Figure 2.5(a) simulates the actual operating point, see Section 2.1.6. Transmission with all 4 settings is explored in Section 2.3.1. The inflector entrance aperture has a radius of 2 mm. The initial ellipse is 8 equally spaced particles simultaneously subscribing 100 π mm·mrad circles in both x-x' and y-y'. Abrupt changes in the frequency and amplitude of the oscillation occur where $\vec{B}$ changes rapidly, see Figure 2.3.

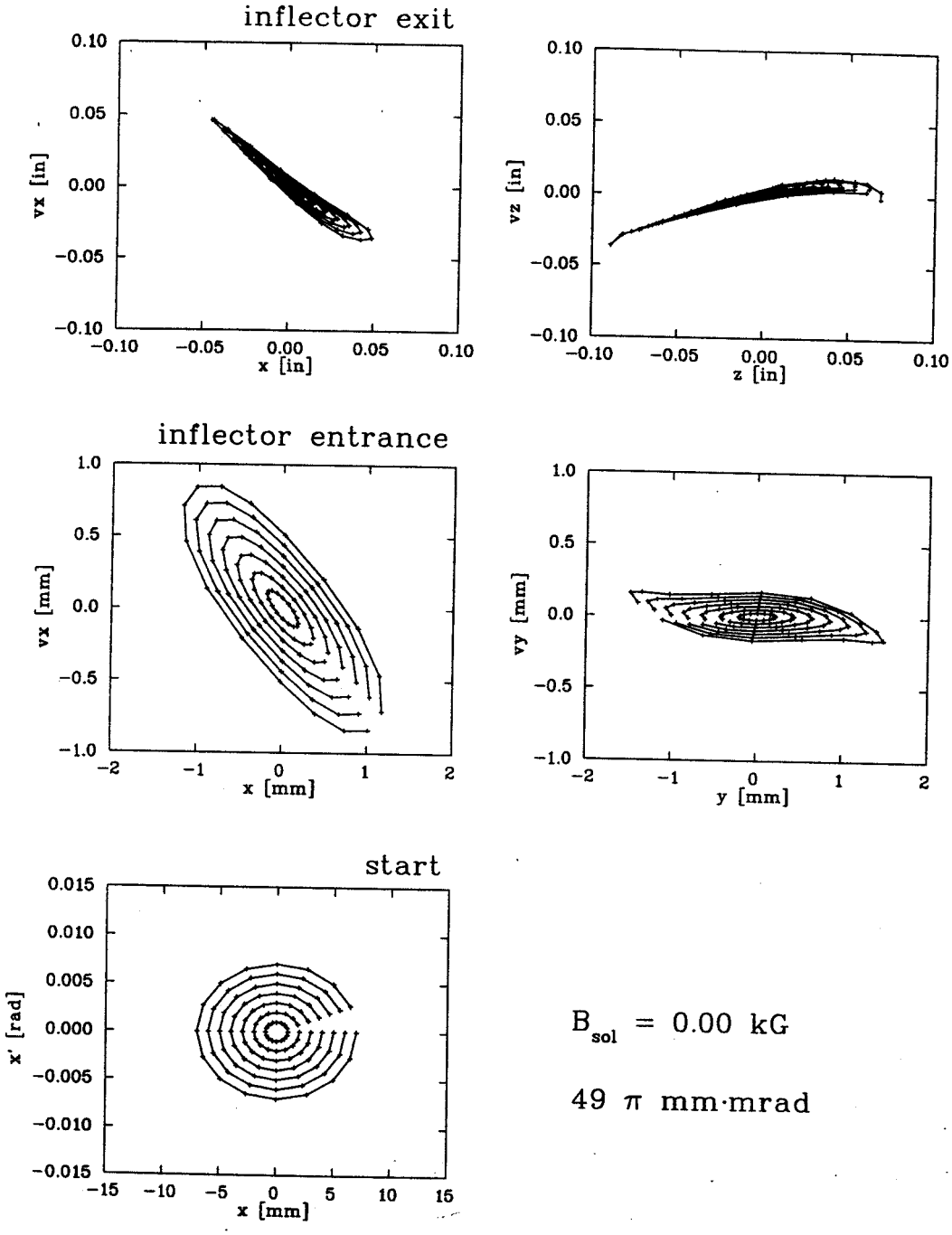

Figure 2.6: 2-D Injection Transport. Case 1, x-x'.
2-D ellipses, with $a = b$, in x-x' phase space are started on axis, ~3 m below the median plane, and followed through the inflector entrance to the exit of the inflector. The focusing solenoid is off, and the largest ellipse which entirely clears the inflector has an area of 49 π mm·mrad The velocities are expressed in units of $\frac{v}{\omega}$.

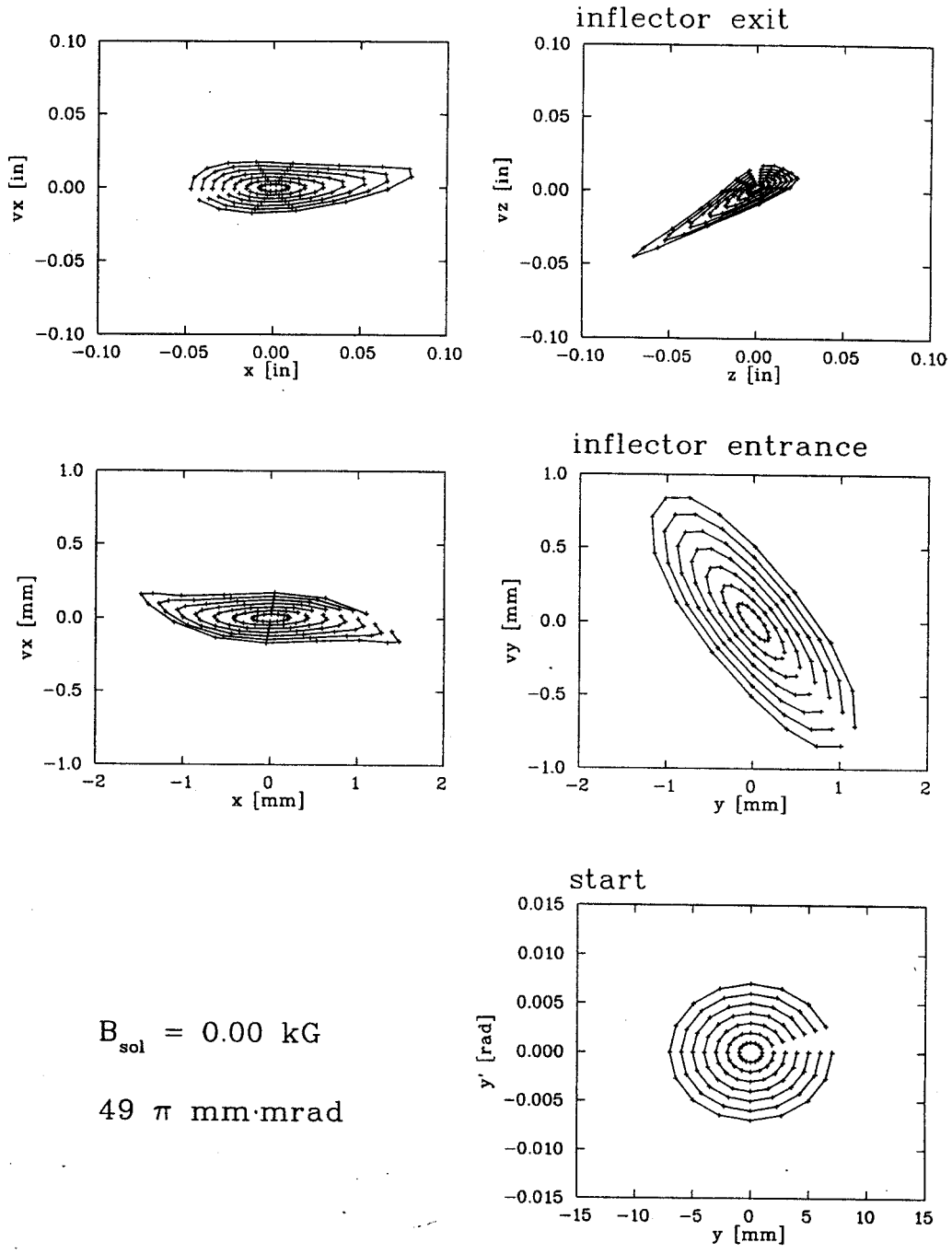

Figure 2.7: 2-D Injection Transport. Case 1, y-y'.
2-D ellipses, with $a = b$, in y-y' phase space are started on axis, ~3 m below the median plane, and followed through the inflector entrance to the exit of the inflector. The focusing solenoid is off, and the largest ellipse which entirely clears the inflector has an area of 49 π mm·mrad. The velocities are expressed in units of $\frac{v}{\omega}$.

the inflector entrance and the inflector exit for all the ellipses which are transmitted in their entirety. The velocities are expressed as a length by dividing by ω_{RF}. This is the same as the cyclotron momentum unit where p is divided by $m\omega$, so the units at the inflector exit are translated to inches for running in Z3CYCLONE, where it is convenient to use inches for r, p_r, z, and p_z.

The particles in each ellipse are connected by lines with one gap, giving the appearance of a spider web. Following the position of this gap within the web at different positions along the cyclotron axis, gives a visual sense of changes in the ellipse orientation. Figures 2.6 & 2.7, case 1, show the transmission of circular ellipses for this cyclotron operating point when the naked solenoid is off. These ellipses are not well matched, and display strong distortions caused by the non-linearities in the inflector. Also, the uncut transmission, which is represented by the area of the largest ellipse drawn in each figure, is relatively small, ~49 π mm·mrad of the initial phase space.

Figures 2.10 & 2.11, case 3, show the transmission with the solenoid tuned to 2.65 kG, to minimize the oscillations in the beam envelope, as in Figure 2.5. Using the solenoid improves the acceptance for these circular starting ellipses, from 49 to 169 π mm·mrad. The transmission for the two adjacent settings in Figure 2.5 are displayed in Figures 2.8 & 2.9, case 2, where B_{sol} is 2.50 kG, and in Figures 2.12 & 2.13, case 4, where B_{sol} is 2.80 kG. Case 2 has the largest acceptance, 196 π mm·mrad, with the acceptance falling to 121-144 π mm·mrad for case 4. Looking at the size and shape of the 'ellipses' at the inflector exit, one sees though that the matched solenoid setting, case 3, transmits the beam with the least distortion in the vertical coordinates. In Figures 2.8, 2.10, & 2.12, the x-x' starting ellipses, the distortions in the z-v_z phase space get worse as B_{sol} increases. In Figures 2.9, 2.11, & 2.13, the y-y' starting ellipses, the distortions in the z-v_z phase

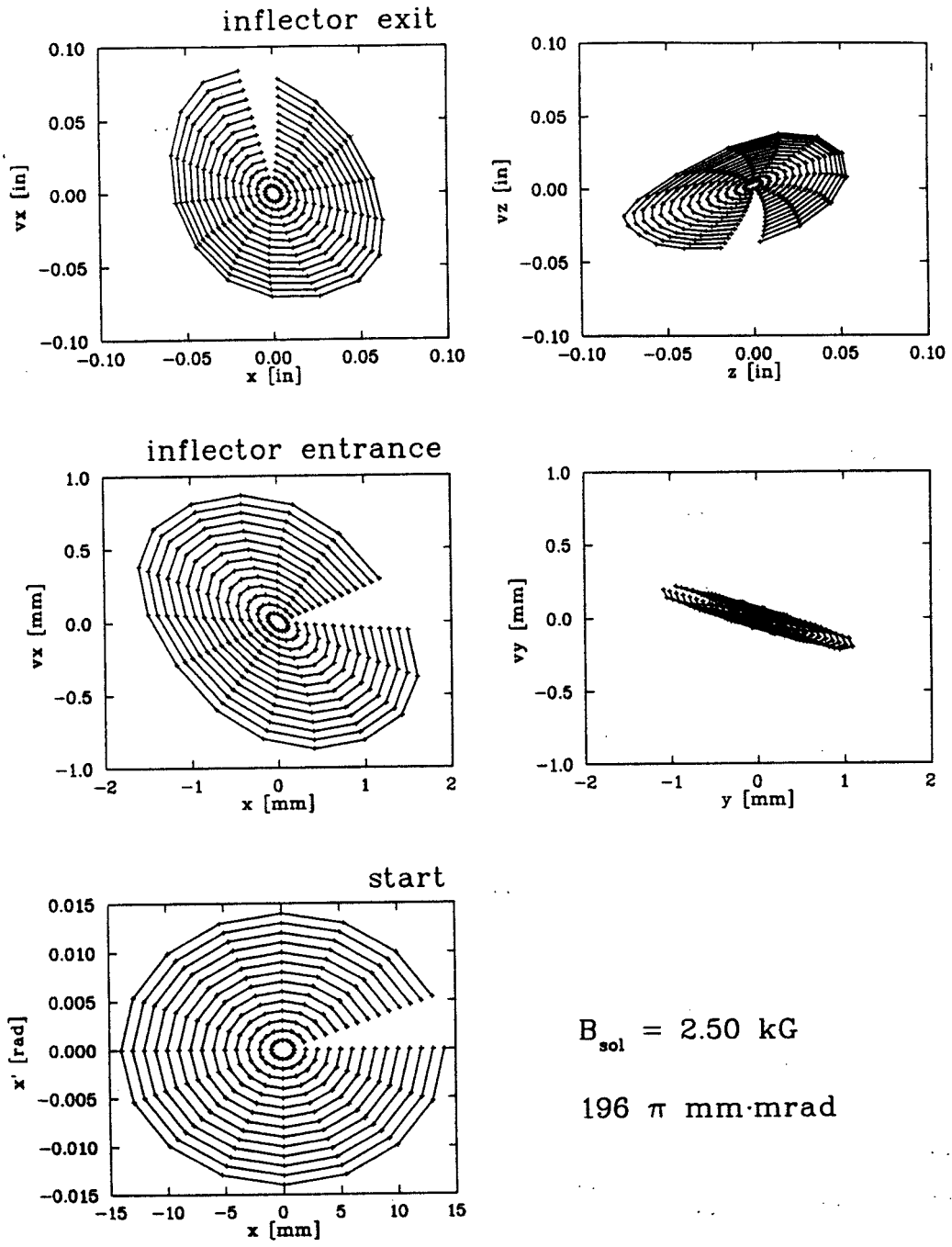

Figure 2.8: 2-D Injection Transport. Case 2, x-x'.
2-D ellipses, with $a = b$, in x-x' phase space are started on axis, ~3 m below the median plane, and followed through the inflector entrance to the exit of the inflector. The focusing solenoid is at 2.50 kG, and the largest ellipse which entirely clears the inflector has an area of 196 π mm·mrad. The velocities are expressed in units of $\frac{v}{\omega}$.

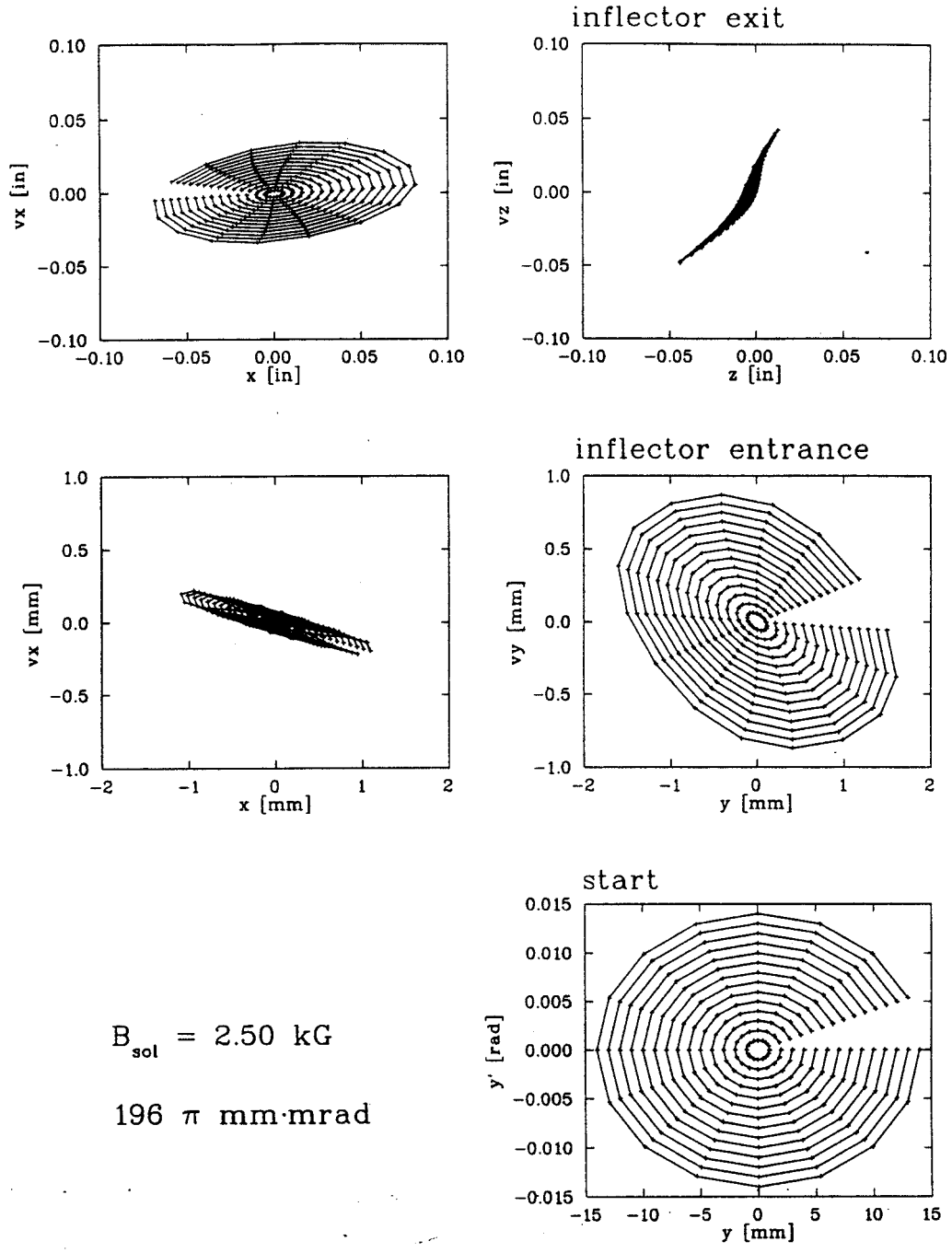

Figure 2.9: 2-D Injection Transport. Case 2, y-y'.
2-D ellipses, with $a = b$, in y-y' phase space are started on axis, ~3 m below the median plane, and followed through the inflector entrance to the exit of the inflector. The focusing solenoid is at 2.50 kG, and the largest ellipse which entirely clears the inflector has an area of 196 π mm·mrad. The velocities are expressed in units of $\frac{v}{\omega}$.

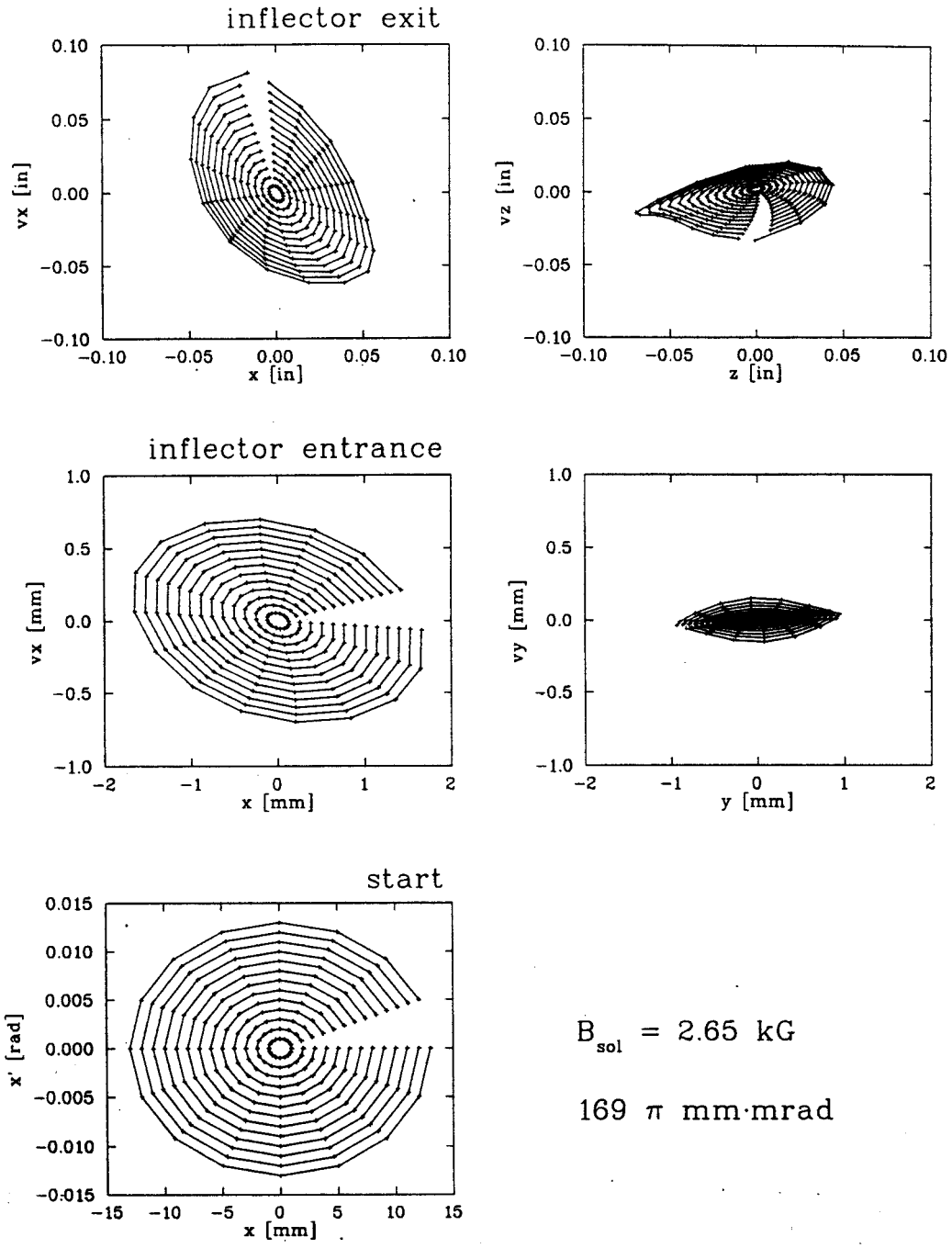

Figure 2.10: 2-D Injection Transport. Case 3, x-x'.
2-D ellipses, with $a = b$, in x-x' phase space are started on axis, ~3 m below the median plane, and followed through the inflector entrance to the exit of the inflector. The focusing solenoid is at 2.65 kG, and the largest ellipse which entirely clears the inflector has an area of 169 π mm·mrad. The velocities are expressed in units of $\frac{v}{\omega}$.

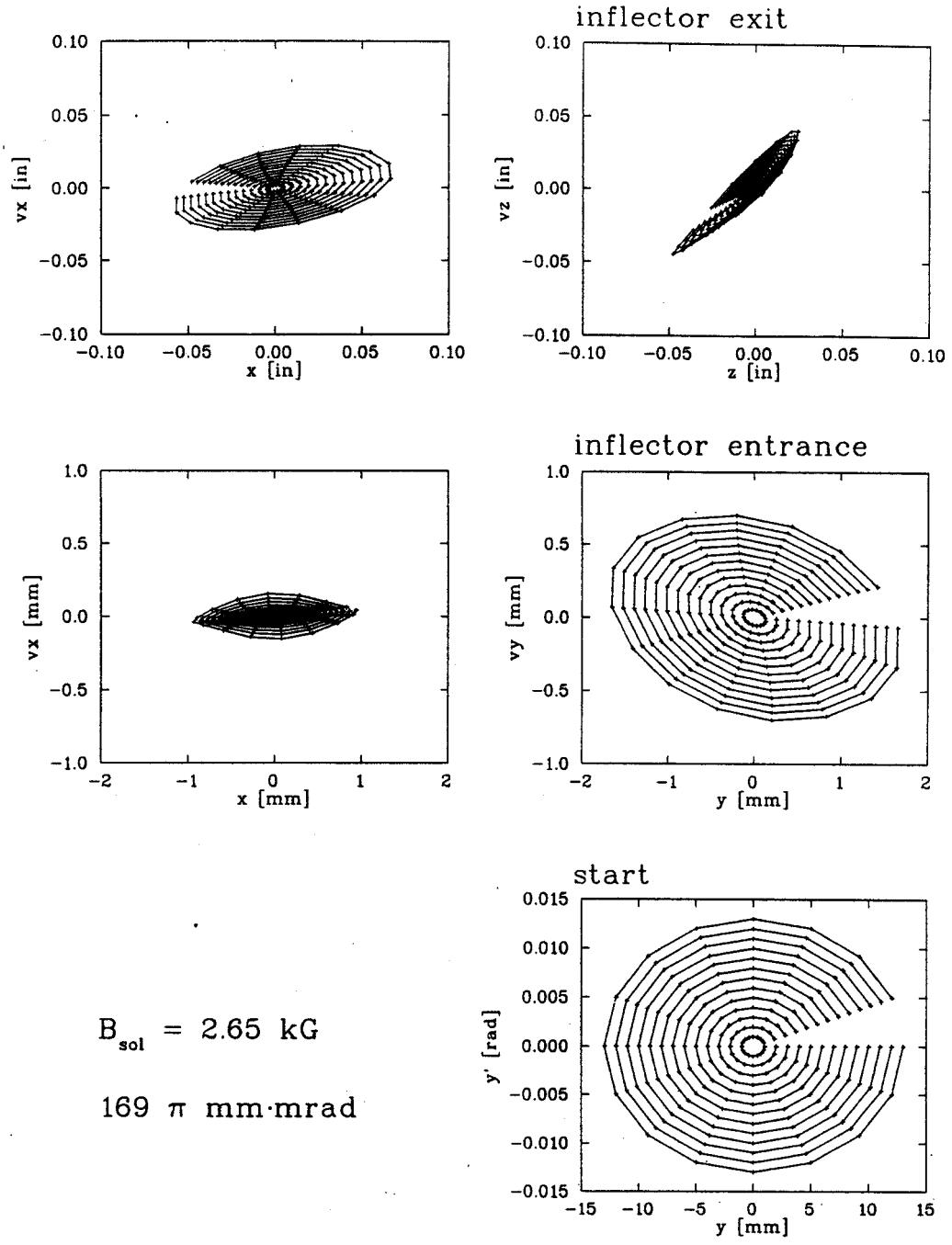

Figure 2.11: 2-D Injection Transport. Case 3, y-y'.
2-D ellipses, with $a = b$, in y-y' phase space are started on axis, ~3 m below the median plane, and followed through the inflector entrance to the exit of the inflector. The focusing solenoid is at 2.65 kG, and the largest ellipse which entirely clears the inflector has an area of 169 π mm·mrad. The velocities are expressed in units of $\frac{v}{\omega}$.

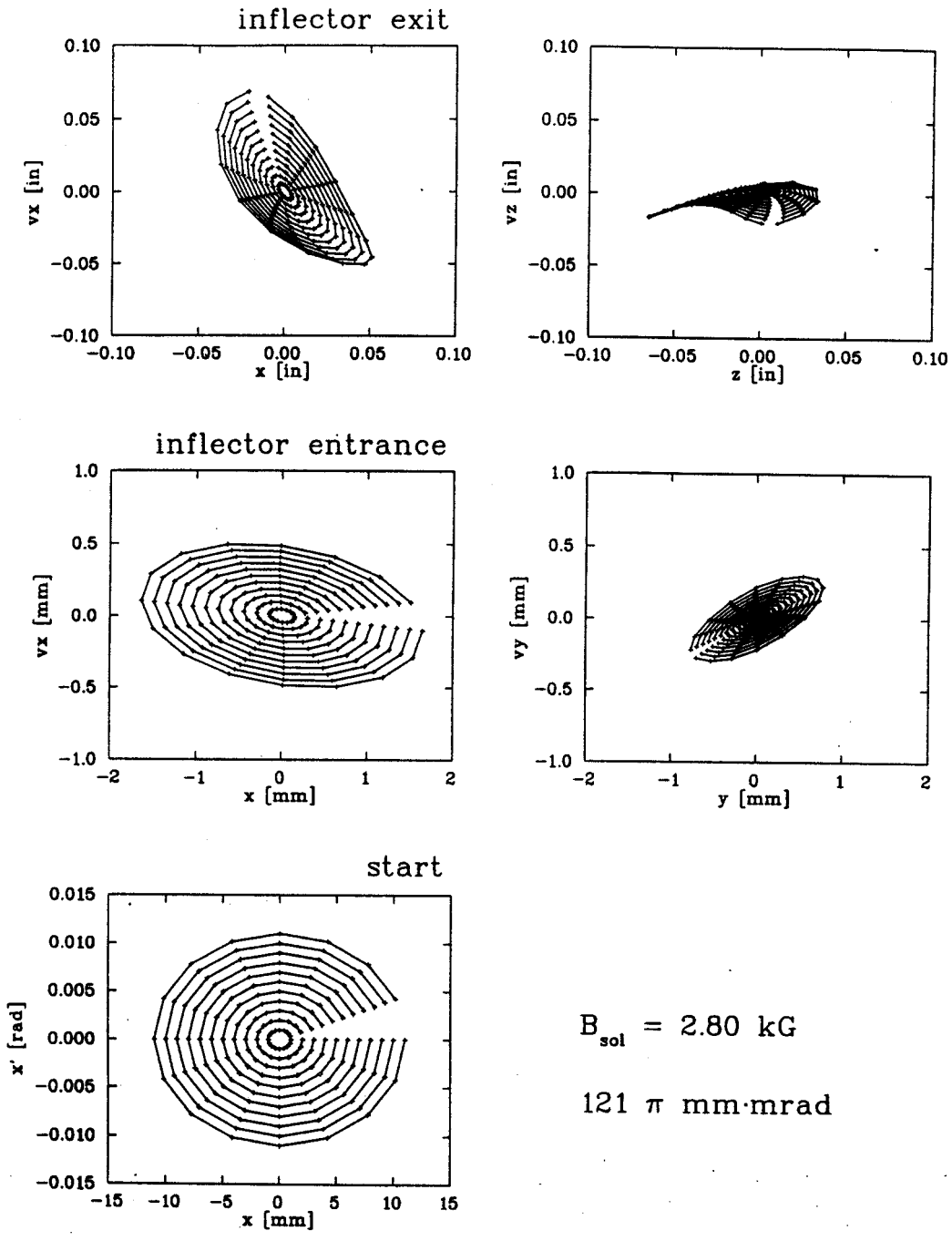

Figure 2.12: 2-D Injection Transport. Case 4, x-x'.
2-D ellipses, with $a = b$, in x-x' phase space are started on axis, ~3 m below the median plane, and followed through the inflector entrance to the exit of the inflector. The focusing solenoid is at 2.65 kG, and the largest ellipse which entirely clears the inflector has an area of 121 π mm·mrad. The velocities are expressed in units of $\frac{v}{\omega}$.

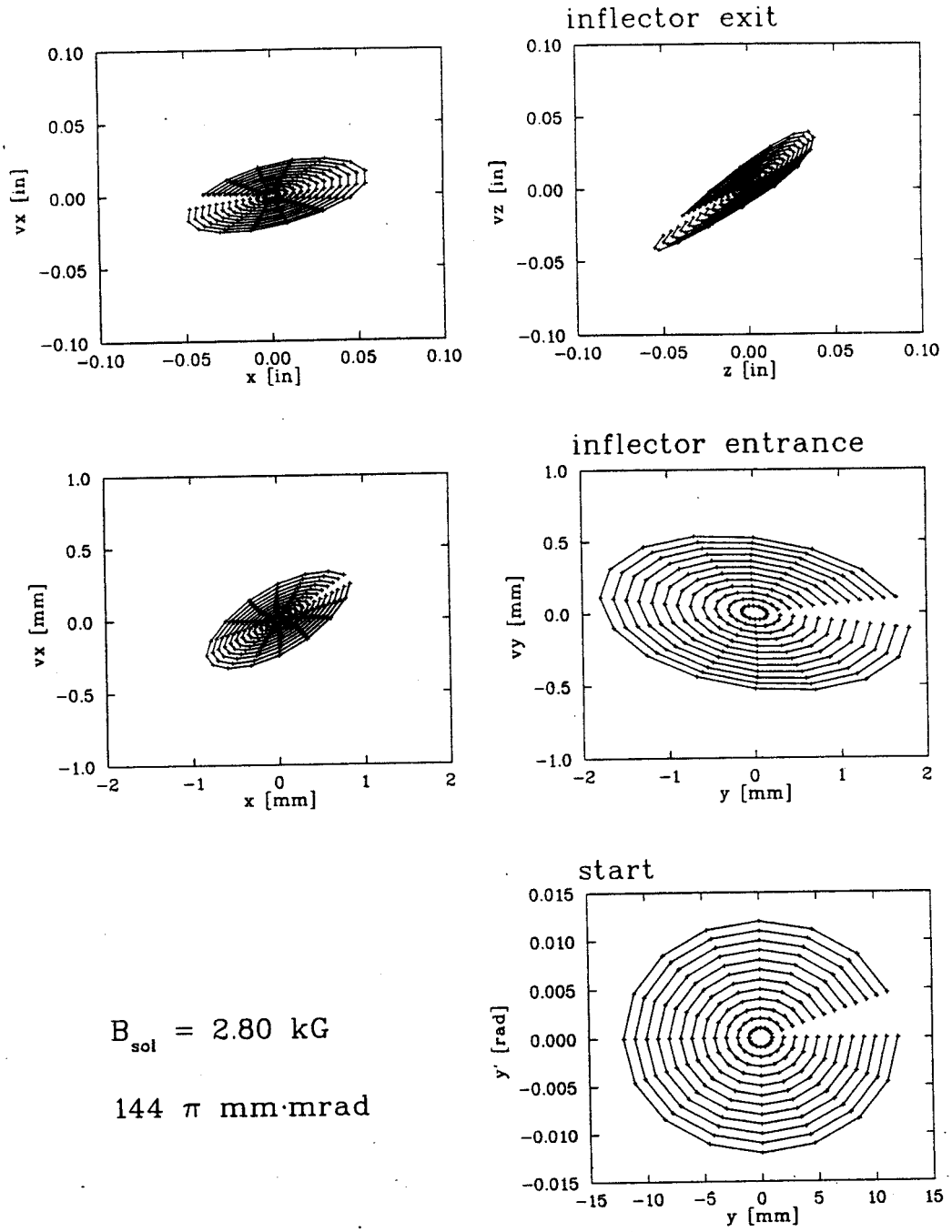

Figure 2.13: 2-D Injection Transport. Case 4, y-y'.
2-D ellipses, with $a = b$, in y-y' phase space are started on axis, ~3 m below the median plane, and followed through the inflector entrance to the exit of the inflector. The focusing solenoid is at 2.80 kG, and the largest ellipse which entirely clears the inflector has an area of 144 π mm·mrad. The velocities are expressed in units of $\frac{v}{\omega}$.

space get better as B_{sol} increases. For both the x-x' and y-y' starting ellipses, the x-v_x exit phase space gets smaller as B_{sol} increases. Case 3 is an acceptable compromise with some distortions, while still accepting a large initial phase space, though it is not the full ECR emittance discussed in Section 2.1.1.

An initially-circular phase space ellipse, though, is not necessarily the best ellipse to use with or without the solenoid. In the 4-D studies, an ellipse was found with much better transmission when $B_{sol} = 0$. Figure 2.14 and Figure 2.15, case 5, show the acceptance to be twice as large, 121 and 100 π mm·mrad , when the initial ellipse has $a = 3b$ and $\theta = -25°$, as that acceptance of the circular ellipses, 49 π mm·mrad , in case 1. Also, the exit phase space in case 5, while distorted, has less distortion than in case 1. Using these ellipses with B_{sol} set at 2.65 kG, case 6, the acceptance increases to areas equivalent to those of cases 2 & 3, 144 and 196 π mm·mrad. But comparing Figures 2.16 & 2.17, where the transmission of case 6 is displayed, to those of case 5, the distortion is clearly worse. In fact, it is comparable to that in Figures 2.6 & 2.7 of case 1, while the matched circular ellipses, Figures 2.10 & 2.11 of case 3, have the least distortion of all 6 cases.

While these 2-D transmission studies where done for only one K1200 operating set point, they have been sufficient to demonstrate that not only is a focussing element similar to the naked solenoid needed to match the injected beam for maximum transmission into the cyclotron, but a quadrapole type focussing element is also necessary to minimize the distortions in the transverse dimensions of phase space. This will be true for all the set points, even though the operational settings will vary. Overcoming the limitations presented by the nonaxial magnetic field during injection would be a valuable improvement in the injection and control of the cyclotron beam. A more detailed study of this problem is recommended, with the caveat that good diagnostics will be needed. The injection conditions which achieved the best

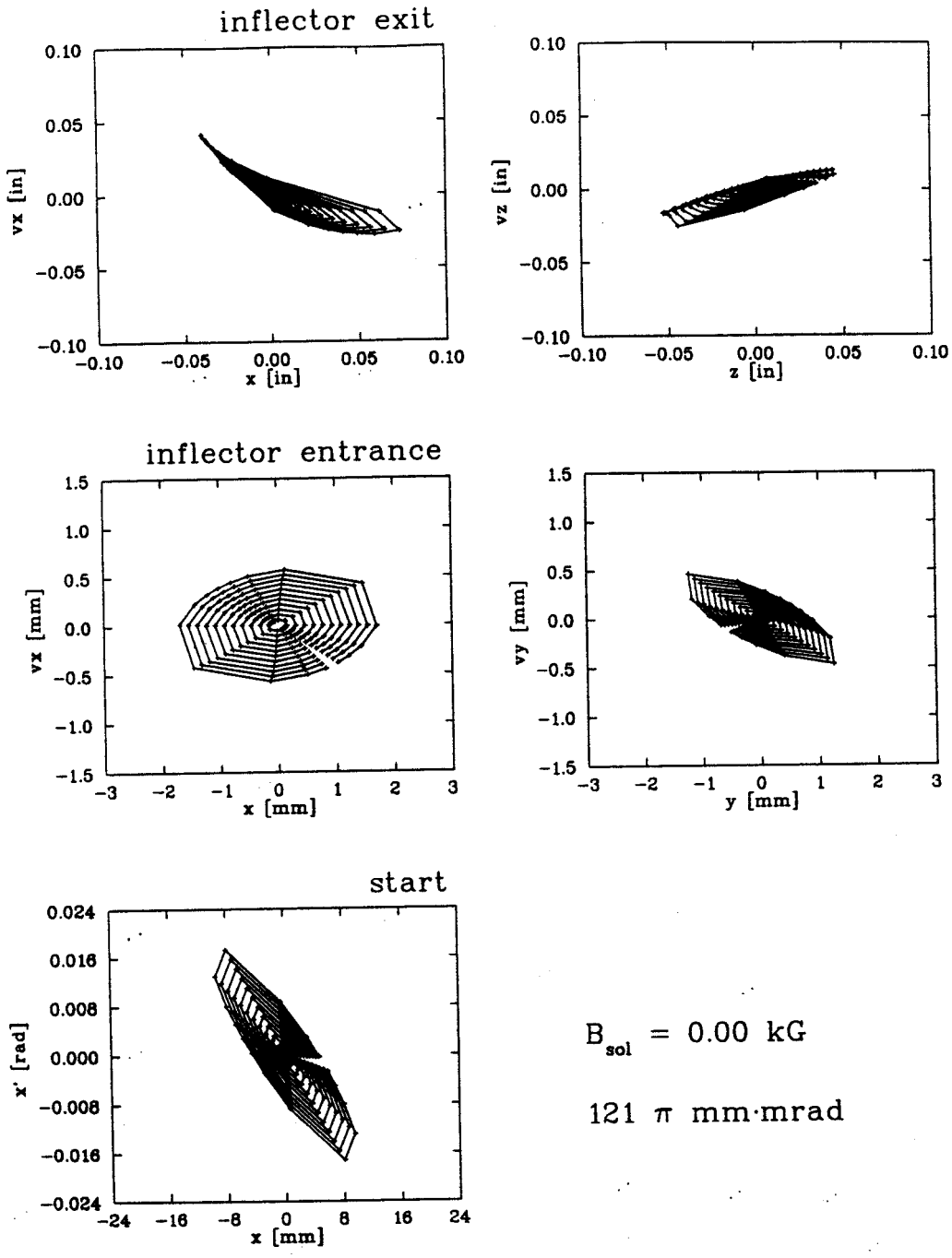

Figure 2.14: 2-D Injection Transport. Case 5, x-x'.
2-D ellipses, with $a = 3b$, in x-x' phase space are started on axis, ~3 m below the median plane, and followed through the inflector entrance to the exit of the inflector. The focusing solenoid is off, and the largest ellipse which entirely clears the inflector has an area of 121 π mm·mrad. The velocities are expressed in units of $\frac{v}{\omega}$, and the axis scales in cases 5 & 6 have been expanded from those in cases 1–4.

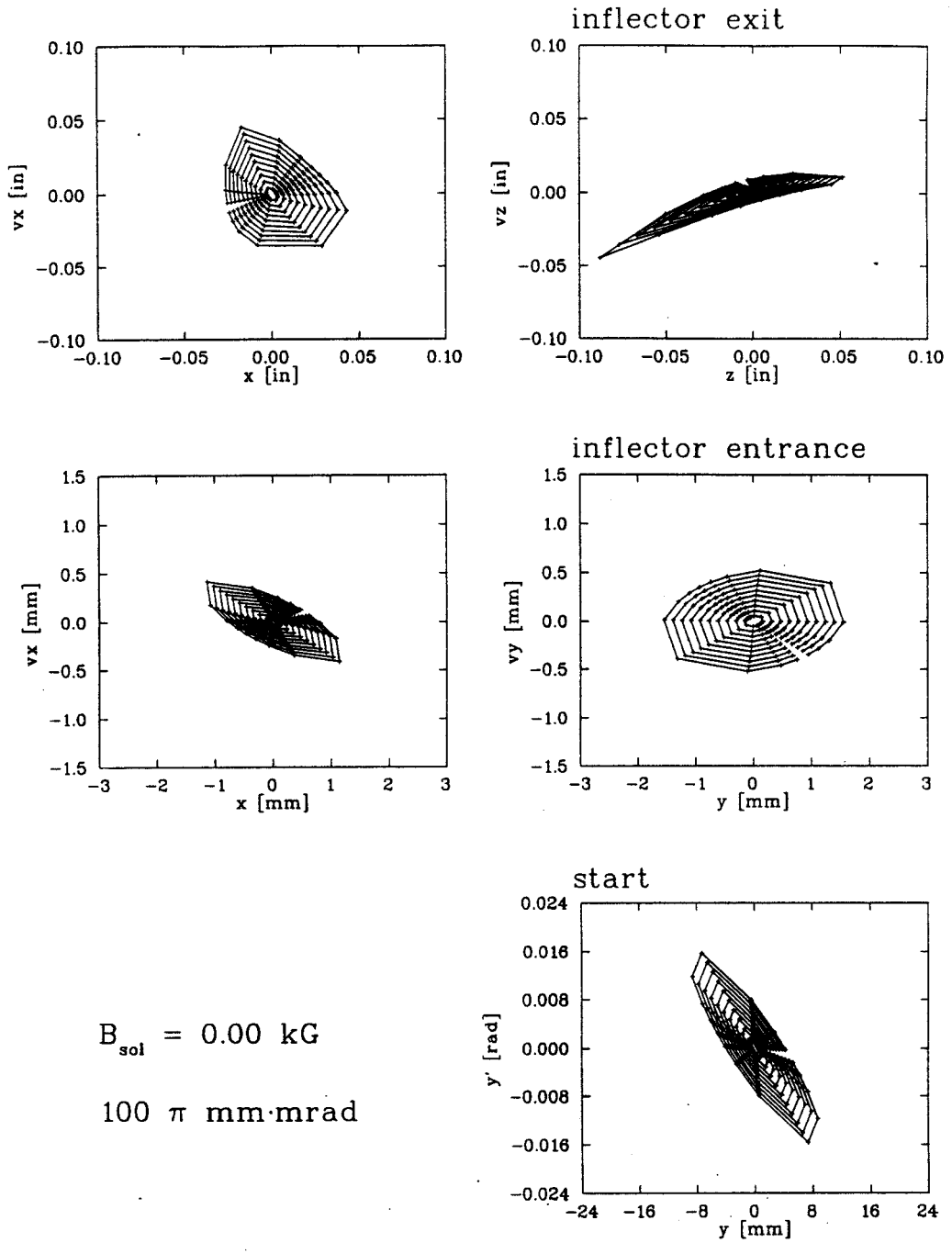

Figure 2.15: 2-D Injection Transport. Case 5, y-y'.
2-D ellipses, with $a = 3b$, in y-y' phase space are started on axis, ~3 m below the median plane, and followed through the inflector entrance to the exit of the inflector. The focusing solenoid is off, and the largest ellipse which entirely clears the inflector has an area of 100 π mm·mrad. The velocities are expressed in units of $\frac{v}{\omega}$, and the axis scales in cases 5 & 6 have been expanded from those in cases 1–4.

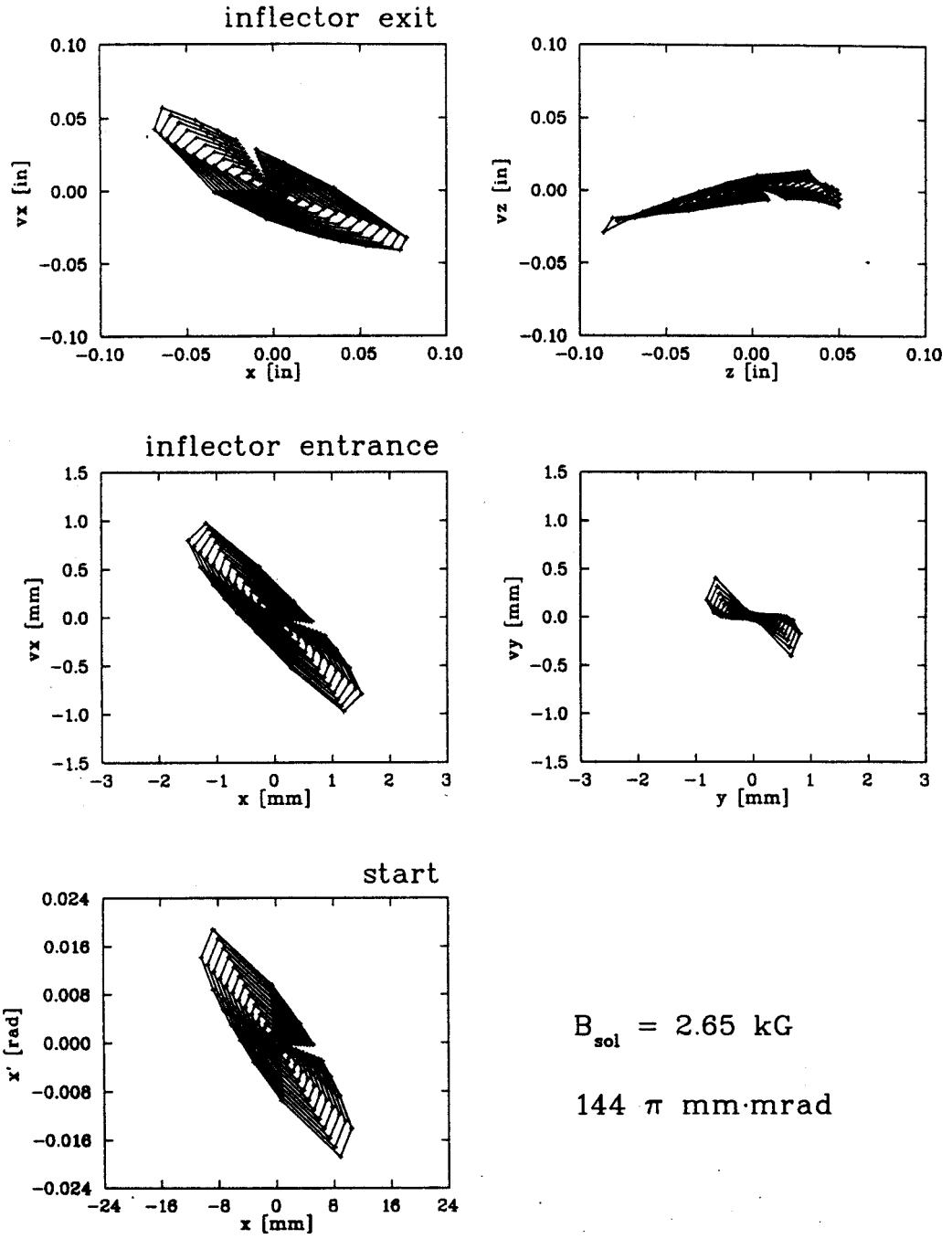

Figure 2.16: 2-D Injection Transport. Case 6, x-x'.
2-D ellipses, with $a = 3b$, in x-x' phase space are started on axis, ~3 m below the median plane, and followed through the inflector entrance to the exit of the inflector. The focusing solenoid is at 2.65 kG, and the largest ellipse which entirely clears the inflector has an area of 144 π mm·mrad. The velocities are expressed in units of $\frac{v}{\omega}$, and the axis scales in cases 5 & 6 have been expanded from those in cases 1–4.

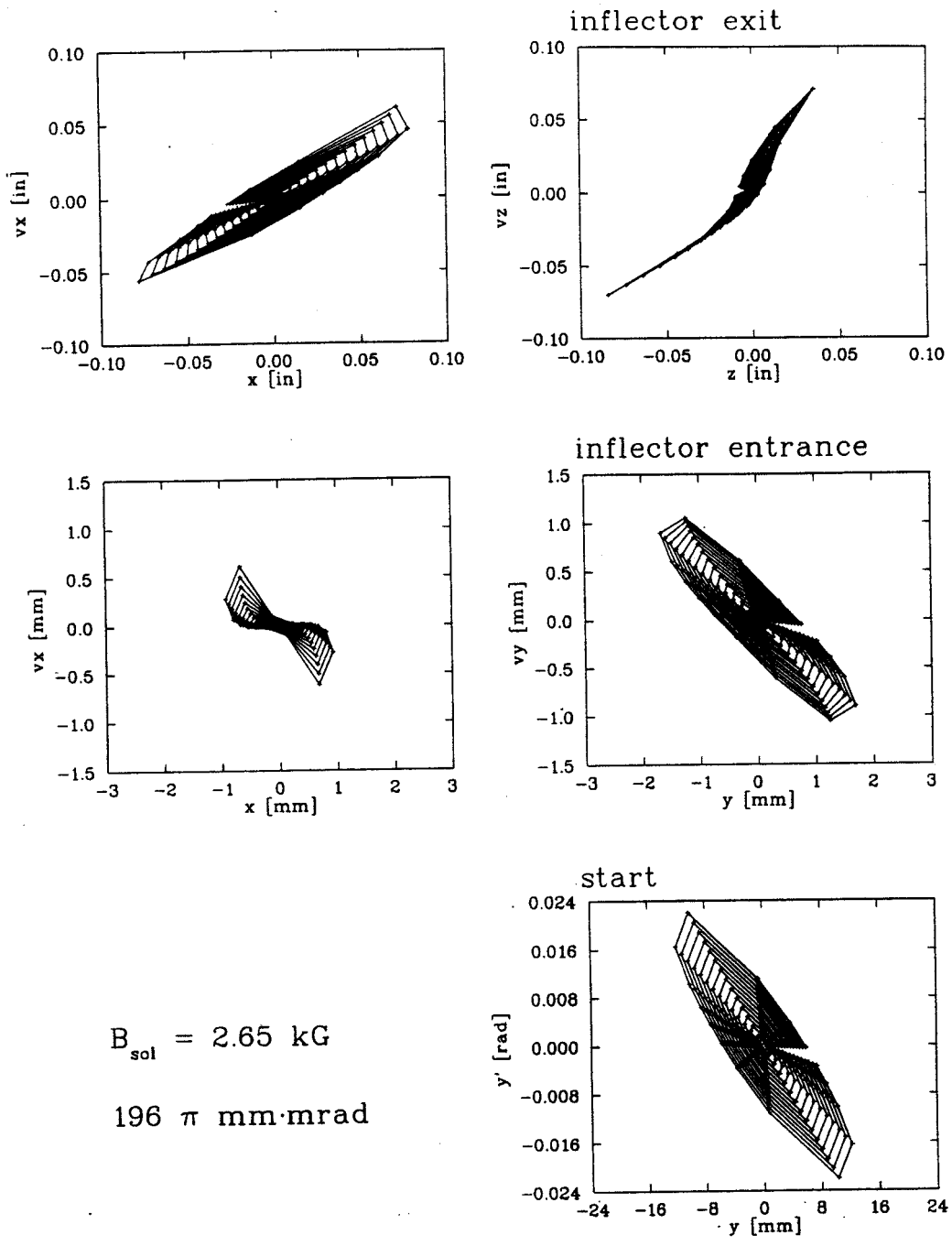

Figure 2.17: 2-D Injection Transport. Case 6, y-y'.
2-D ellipses, with $a = 3b$, in y-y' phase space are started on axis, ~3 m below the median plane, and followed through the inflector entrance to the exit of the inflector. The focusing solenoid is at 2.65 kG, and the largest ellipse which entirely clears the inflector has an area of 196π mm·mrad. The velocities are expressed in units of $\frac{v}{\omega}$, and the axis scales in cases 5 & 6 have been expanded from those in cases 1–4.

transmission through the inflector, case 3, was not synonymous with the largest accepted emittance, case 2, so a measurement of the total injected current will not be sufficient when tuning the injection line for optimum acceptance in the cyclotron.

2.3.2 4-D Transmission Through the Central Region

A full picture of the acceptance into the cyclotron requires the full coupling of the transverse planes of motion. To this end, a uniformly spaced four dimensional pulse of particles will be integrated up the axis of the cyclotron and through the spiral inflector. The same solenoid settings and ellipse shapes used in cases 1, 3, 5, & 6 will be used. The area, though, will be restricted to $\sim$100 π mm·mrad in each of the x-x' and y-y' planes, with starting positions centered at (0,0) and spaced every 2 mm and every 2 mrad. The full four dimensional starting conditions will consist of all coordinates satisfied by the conditions in both planes.

These 4-D pulses will be traced to the inflector, then out through the central region. Integrating in the central region requires that the dimension of time be fully sampled. To be consistent with calculations using the buncher, time will be introduced there, with pulses crossing the buncher every 5° RF. This requires that more pulses be used than if the inflector exit had been used, but gains the advantage that time at the inflector exit will be fully sampled due to the debunching of particles in the yoke and the inflector.

Figure 2.18 shows the distribution of these particles in the x-y plane at the inflector entrance, the radius of the inflector aperture, and the fraction of these particles which will be successfully transmitted through the inflector. The use of the solenoid to maximize acceptance into the inflector by minimizing the oscillations in the beam envelope, is dramatically demonstrated. For the cases where $B_{sol} = 0.0$ kG,

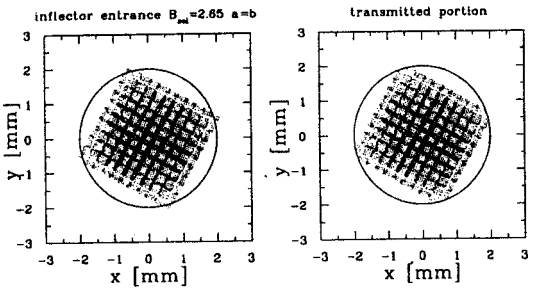

(a) Case 3: $B_{sol} = 2.65$ kG, a=b

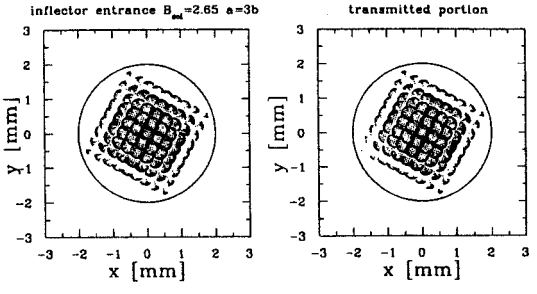

(b) Case 6: $B_{sol} = 2.65$ kG, a=3b

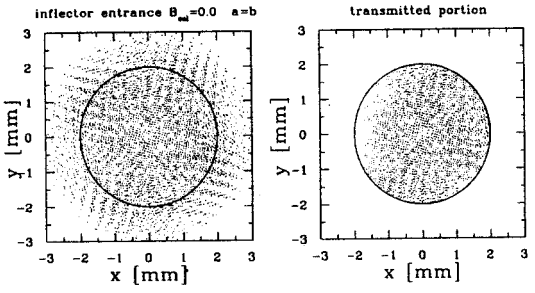

(c) Case 1: $B_{sol} = 0.00$ kG, a=b

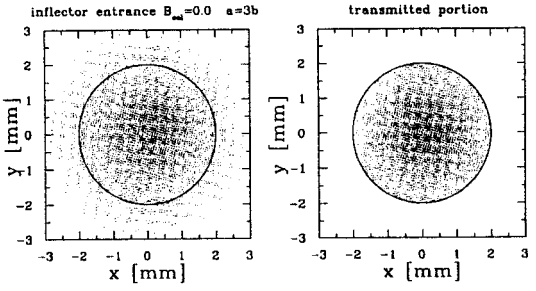

(d) Case 5: $B_{sol} = 0.00$ kG, a=3b

Figure 2.18: x-y Particle Distribution at the Inflector Entrance.
A 4-D uniform grid of particles, spaced every 2 mm and 2 mrad, were started within the 100 π mm·mrad x-x' and y-y' phase spaces of cases 1, 3, 5, & 6, described in Section 2.3.1, 3 m below the median plane. The position coordinates of each particle at the entrance of the inflector are represented by a point in each plot. The first plot in each subfigure is immediately before the entrance aperture, depicted by the solid circle, and the second plot shows the subset of those particles which successfully clear the electrodes, and the entrance and exit apertures. The structure is an artifact of the starting conditions.

the primary loss of particles is the entrance aperture, but a small region of particles with negative x can be seen to be lost on the inflector electrodes.

The square patterns, as well as the smaller circles and wedges, most pronounced in Figure 2.18(b), are byproducts of the starting conditions. The initial grid in x-y is a square. Each circle is associated with an initial point in x-y. Every point within one circle or wedge had a specific v_x and v_y. If it were in an infinitely long uniform solenoidal field, this particle would travel in a helix, which would return to the same x-y, at some later z. Every particle starting at this point, with the same value of $|v_\perp|$, would travel in a similar, though rotated, helix. So all particles with $|v_\perp|$ = constant will inscribe a circle, centered at the initial point in x-y, whose radius oscillates with a frequency, $\omega_s = qB/m$, reaching a maximum radius of $r_s = v_\perp/\omega_s$, and with a minimum radius of 0, as it travels down the length of the solenoid. (ω_s will be called the gyrofrequency, to distinguish it from ω_0, the specific cyclotron frequency inside the cyclotron.) Since $v_z = \sqrt{v_0^2 - v_\perp^2}$ and v_0 = constant (mono-energetic starting condition), at any given z, each set of particles with a given value of $v_\perp$, would be at a different point in their oscillation, and each point in x-y, will be surrounded by a disk of particles. With the starting conditions constrained to lie within an ellipse of area 100 π mm·mrad in both x-v_x and y-v_y phase spaces, when looking at the edges of the x-y distribution, $\vec{v}_\perp$ will be limited in size and direction, and a wedge will be seen. Since $\vec{B}$ is definitely not uniform, we are entering a solenoid, the whole distribution will be compressed, and there will be distortions, which will be greater at the edges. Note that there has also been a rotation of the entire starting grid which is most likely due to the drifts caused by *grad-B* and *field line curvature*[51].

Figure 2.19 shows the distribution of these particles in velocity coordinates at the same position as Figure 2.18. Once again, clear structure can be seen when the solenoid is used to focus the particles into the inflector. The distortions in all four

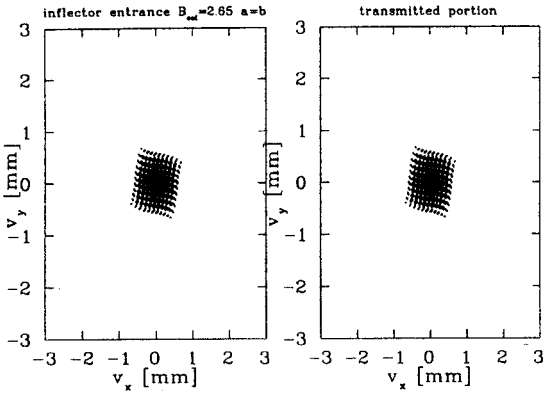

(a) Case 3: $B_{sol} = 2.65$ kG, a=b

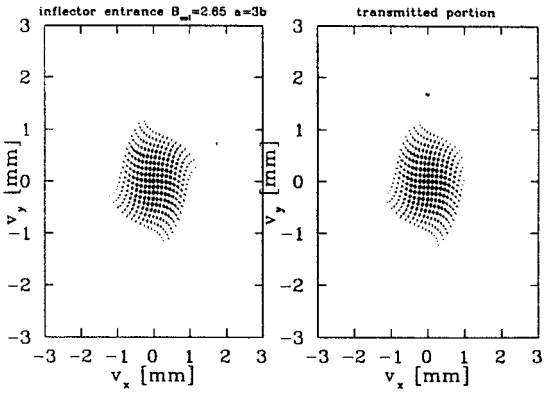

(b) Case 6: $B_{sol} = 2.65$ kG, a=3b

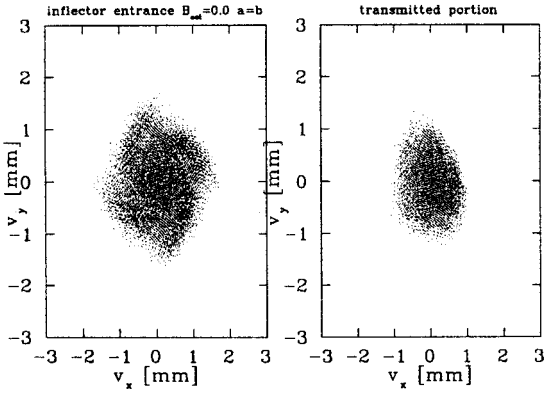

(c) Case 1: $B_{sol} = 0.00$ kG, a=b

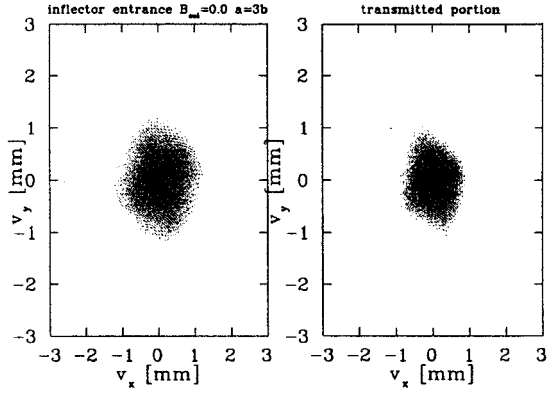

(d) Case 5: $B_{sol} = 0.00$ kG, a=3b

Figure 2.19: v_x-v_y Particle Distribution at the Inflector Entrance.
A 4-D uniform grid of particles, spaced every 2 mm and 2 mrad, were started within the 100 π mm·mrad x-x' and y-y' phase spaces of cases 1, 3, 5, & 6, described in Section 2.3.1, 3 m below the median plane. The velocity coordinates of each particle at the entrance of the inflector are represented by a point in each plot. The first plot in each subfigure is immediately before the entrance aperture, and the second plot shows the subset of those particles which successfully clear the electrodes, and the entrance and exit apertures. The structure is an artifact of the starting conditions.

cases demonstrate nonlinearities which result from expanding B to order r^2 while traversing the yoke. Notice that the matched ellipses, case 3 and case 5, matched to a particular solenoid setting, present a smaller area in velocity coordinates than do the associated unmatched ellipses. In a field that changes adiabatically, the magnetic moment would be constant, so

$$v_{\perp_f} = v_{\perp_i}\sqrt{B_f/B_i} = v_{\perp_i}\sqrt{36.3/.7}. \tag{2.11}$$

This is definitely not so, else for cases 1 & 3, $\max(v_{\perp_f})$ would be .81 mm, and in cases 5 & 6, $\max(v_{\perp_f})$ would be 1.3 mm. The solenoid has been used to optimize the crossing of the nonadiabatic regions described in Figure 2.3 so as to minimize the growth of $v_\perp$ at these points (see Figure 2.5.) Also noticeable, is the spreading of v_x and v_y with x_i and y_i. This is much worse without the focussing solenoid, removing most of the fine structure in cases 1 & 5 in both Figures 2.18 & 2.19. These two distinctions, focussing the solenoid in cases 3 & 6, and matching the ellipses in cases 3 & 5, which prove to be advantageous in increasing the acceptance of the spiral inflector in Section 2.3.1, can now be followed inside the cyclotron.

But first a digression to the central region acceptance, and phase compression in the first turn within the central region. Figure 2.20 shows the RF times of 11 central rays spaced 5° apart, centered about the starting time of $\tau_0 = 220.°$, at the inflector exit. These times are followed to a position inside the puller and every 360° in azimuth thereafter for 3 turns. (See Figure 2.4(b) for details of the central ray orbits in the central region.) The first turn quickly compresses the phase spread to half of its initial width. Calculations carried to the radii of the probes show that the spread will recover to 5/8ths of its initial width. This is a feature of this central region design.

The acceptance in time of the central region is displayed in Figure 2.21(a), where

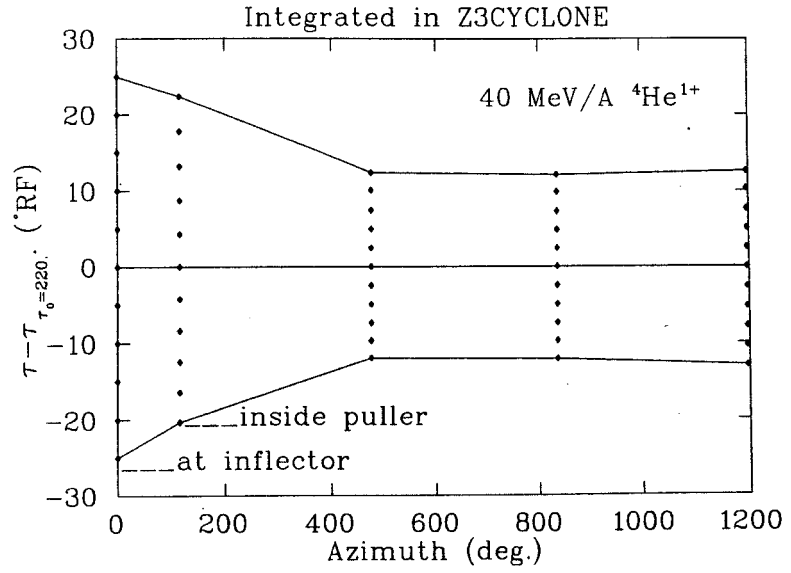

Figure 2.20: Phase Compression in the K1200 Low Voltage Central Region.
The starting times of 11 central ray orbits started 5° apart in time, and their times of arrival at an azimuth which includes the inside of the puller, all drawn relative to the time of the central ray whose starting time is 220°. Note the rapid compression in time during the first turn.

all particles clearing the central region were binned in 1° steps, and the maximum was normalized to 100%. In all four cases, with small variations, the base is 60°, the FWHM is 45°, and the transmission is flattopped for 30-40°. Figure 2.21(b) shows these same particles after integrating 11 turns through the central region. The phase compression has reduced the FWHM to 29°, but a non-linearity can be seen, in that it is no longer flattopped, since the trailing phases are compressed slightly more than the leading phases.

Figure 2.22(a) demonstrates that the phase and energy are very strongly correlated. With a slight broadening, these E-ϕ density plots follow Equation 1.2 quite closely. Figure 2.22(b) shows the r-ϕ curves corresponding to these E-ϕ curves. Note the broadening of the r-ϕ curves by the physical spot size of the beam in r and p_r. These graphs demonstrate that the E-ϕ correlations, resulting from having $\int \sin(\phi) \mathrm{d}E \neq 0$, can be used to turn radial cuts in the beam into time cuts.

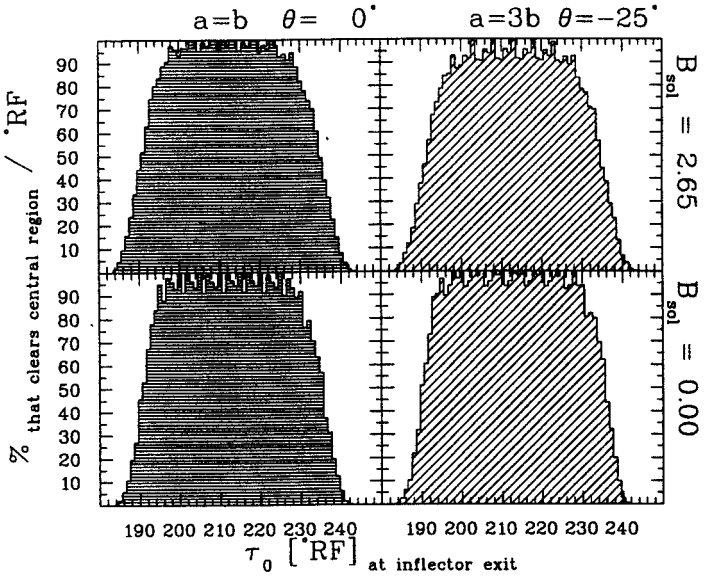

(a) K1200 Acceptance in RF Degrees

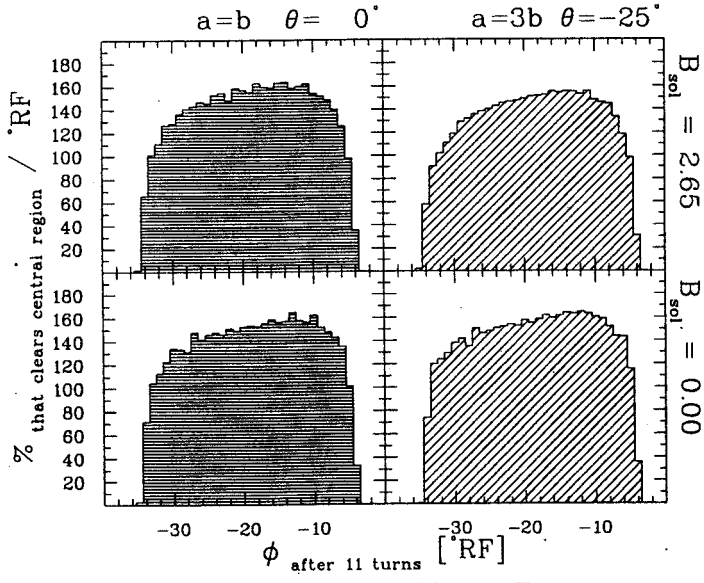

(b) Beam Phase After 11 Turns

Figure 2.21: K1200 Acceptance in Time for the Low Voltage Central Region.
K1200 DC time acceptance is histogrammed for all four 4-D transmission studies. The FWHM is $\sim 45°$ in each case, Figure 2.21(a). The central region compresses this to $\sim 29°$, for acceleration inside the cyclotron, Figure 2.21(b). The notation, used here and in the following graphs, above each graph describes the starting ellipses at the bottom of the injection line, and on the right side is the strength of the focussing solenoid, in kG.

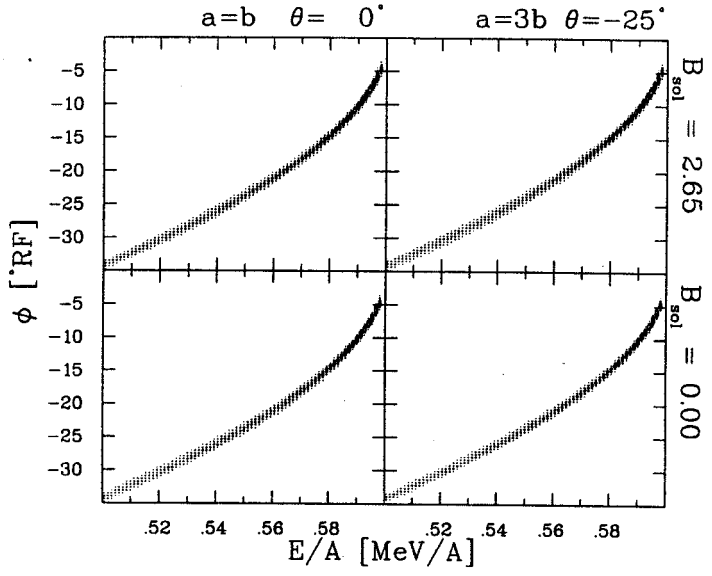

(a) E-ϕ Correlations After 11 Turns

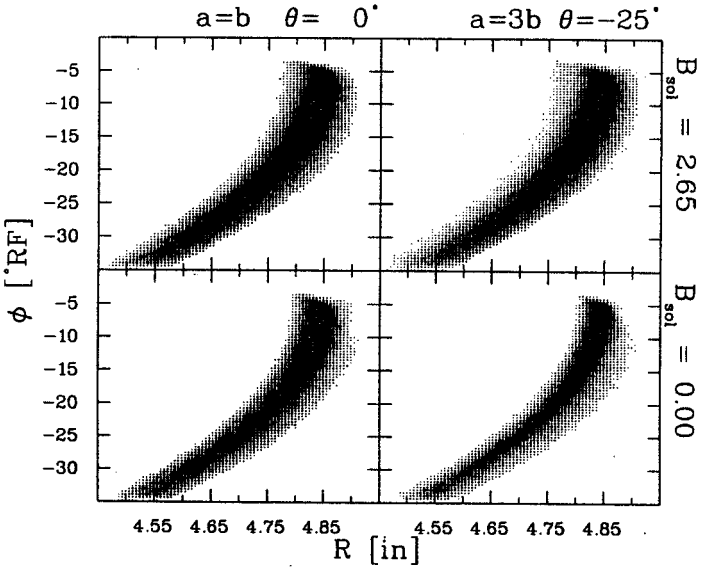

(b) r-ϕ Correlations After 11 Turns

Figure 2.22: E-ϕ and r-ϕ Correlations Inside the Cyclotron.
Figure 2.22(a) shows how the 4-D monoenergetic pulses distribute in E-ϕ after transmission through the central region. These are density plots where the size of the box increases as the density in that quadrant increases. Figure 2.22(b) depicts the resultant r-ϕ distribution. This r-ϕ distribution will be used later to cut the beam in time.

Figures 2.23, 2.24, & 2.25 are snapshots of the beam density in spatial coordinates after 11 turns of acceleration in the K1200 cyclotron. In Figure 2.23(a), the density of the beam in r-z is presented. The spot size is significantly larger when the solenoid is used to focus the beam spot into the inflector. Matching the injection phase space ellipses reduces the spot size. More importantly, judging from the shape of the intense core, it makes a more compact ellipse. Note that the behavior of the spot size here, is exactly opposite of that at the inflector entrance. In Figure 2.18, the spot size is smaller when the solenoid is being used to focus the beam into the inflector. The inflector has also left the beam strongly correlated in r and z.

Figure 2.23(b) has the p_r-p_z density plots, which correspond to the v_x-v_y plots in Figure 2.19. In the same manner as with the spot sizes, the smaller dispersion at the inflector entrance results in a greater dispersion inside the machine. This is the cause of the large spot size resulting from focussing the beam into the inflector. Also important is the correlation induced in the cases with unmatched ellipses. Matching the ellipse removes this correlation, and results in a smaller core of particles.

The only clear aperture cuts visible in these phase space plots can be seen in Figure 2.24(a). Here notches can be seen at the right edge near $r = 4.9$ in. These notches are from cuts made by the spiral inflector electrodes. These cuts at the edge are mirrored in the denser core, producing a distorted spot in r-p_r, in all but case 3 where the solenoid has been used with a matched ellipse. It is important to remember that in any graph with r as one of the axes, that the long spread in r is due to the E-ϕ correlation. Even so, there is still a small reduction in p_r when the injected beam is not focussed into the inflector. Matching, and you may get tired of hearing this, matches the core of the beam into a smaller spot in r-p_r phase space.

The same r-z correlation seen in Figure 2.23(a) can be seen in Figure 2.24(b), a plot of r-p_z. Matching the injection phase space ellipses, gives both a smaller

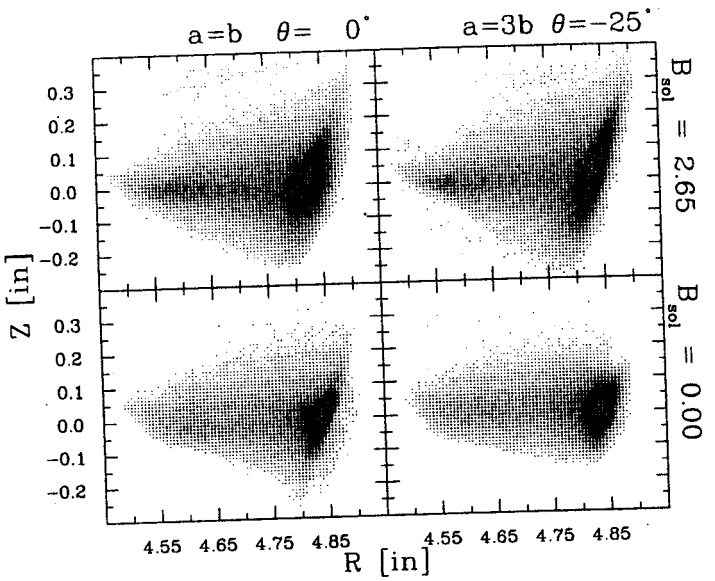

(a) r-z Density Plots After 11 Turns

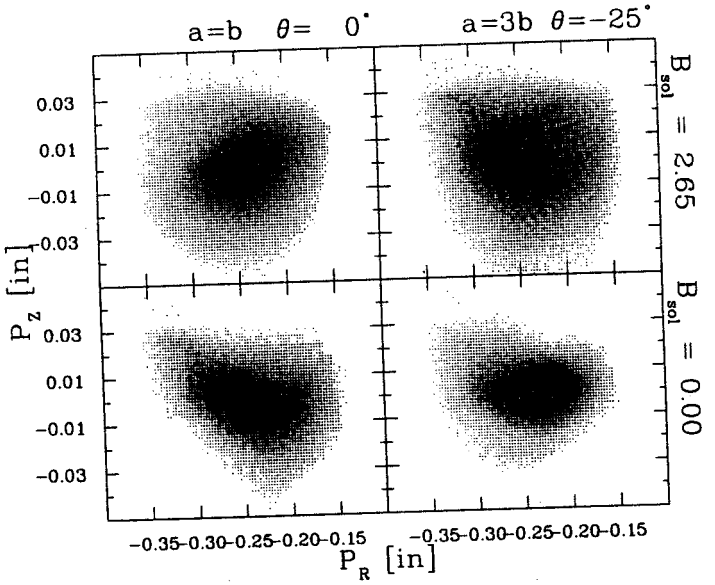

(b) p_r-p_z Density Plots After 11 Turns

Figure 2.23: r-z and p_r-p_z After 11 Turns.
These graphs correspond directly with those in Figure 2.18, and Figure 2.19. The use of the solenoid to get improved transmission through the inflector, results in a larger beam spot and a greater divergence inside the cyclotron, even though these traits were smaller at the inflector entrance. The matched starting ellipses, cases 3 & 5, also make the these traits smaller, though not as strongly as the solenoid. Also, the inflector has correlated r with z.

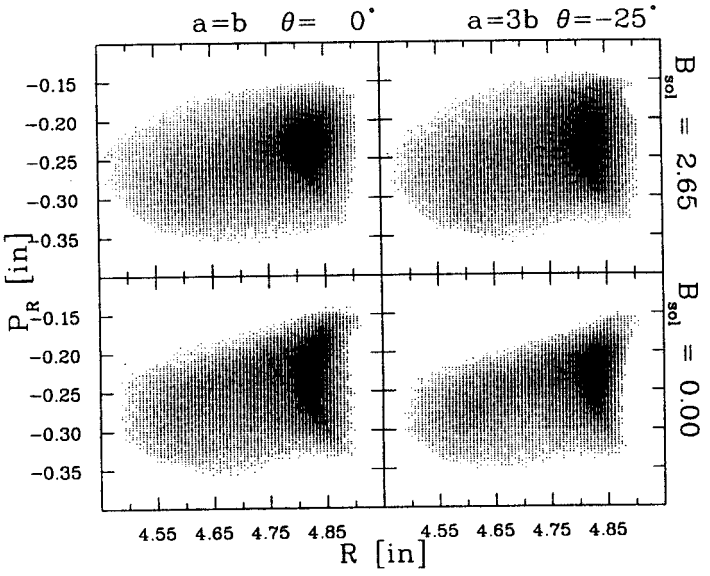

(a) r-p_r Density Plots After 11 Turns

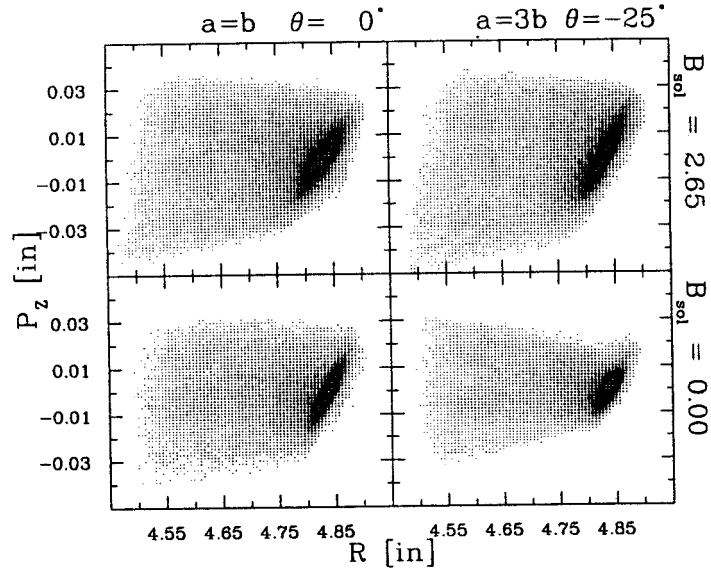

(b) r-p_z Density Plots After 11 Turns

Figure 2.24: r-p_r and r-p_z After 11 Turns.
The core of the r-p_r distribution is crescent shaped without the solenoid. The core becomes circular when the solenoid is used to maximize transmission through the inflector, and the injection ellipse has been matched. The notches to the right side of the r-p_r graphs are aperture cuts from the inflector electrodes. In both graphs, matching the starting ellipses improves the beam characteristics. In r-p_z, the beam spot is smaller without the solenoid.

total spot size (core + halo +tail), and a smaller, more compact core. The solenoid, having focussed the beam into the inflector, has given a larger spot in this pair of dimensions as well as in the three previous pairs.

The z-p_r graphs, in Figure 2.25(a), are very much like the p_r-p_z graphs from Figure 2.23(b). So r will be correlated with z and p_z by the inflector, but p_r need not be correlated with the vertical motion. It is fascinating, that in both sets of graphs, that the correlation in the halo is removed not by matching, as is the correlation in the core, but it is removed by focussing with the solenoid. Otherwise, focussing makes bigger spots than without focussing, and matching makes the spot size a little bit smaller regardless of the focussing.

Figure 2.25(b) shows the z-p_z motion during a defocussing period within the cyclotron, depicting part of the incoherent oscillations typical of cyclotron beams. (Focussing will rotate both the ellipse and the bowtie halo counter-clockwise.) Here, the response of the beam to injection conditions, remains the same as in the five previous couplings of the transverse phase spaces of the beam.

In summary, this study of the coupling of the transverse phase spaces resulting from injecting the beam axially through a spiral inflector has found that r will be coupled with z and p_z. Matching the injection phase space ellipses into the inflector will also match the injected beam into the cyclotron's acceptance, resulting in smaller transverse beam spots. Matching also removes the coupling of p_r with z and p_z. Focussing the injected beam into the inflector aperture makes the transverse beam spot larger.

Finally, with the 4-D injection studies completed, Table 2.1 presents transmission efficiencies for these four cases. On the left is a description of the injection parameters for each case, and on the right, the current in each stage is presented as

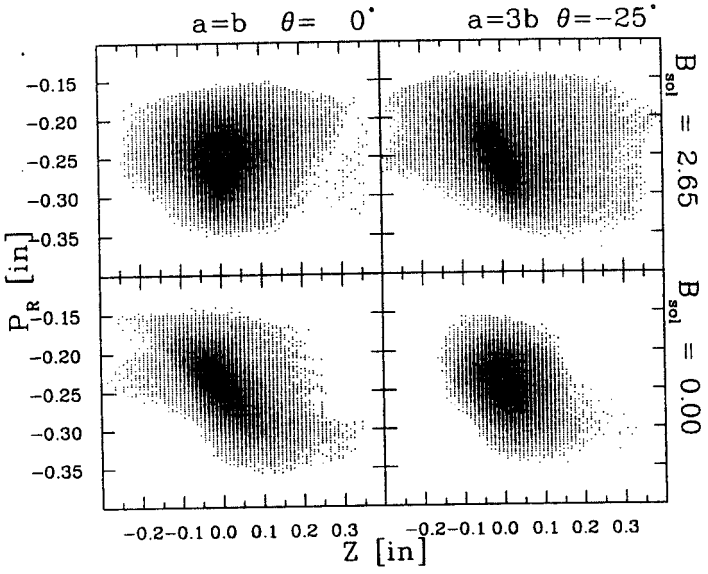

(a) z-p_r Density Plots After 11 Turns

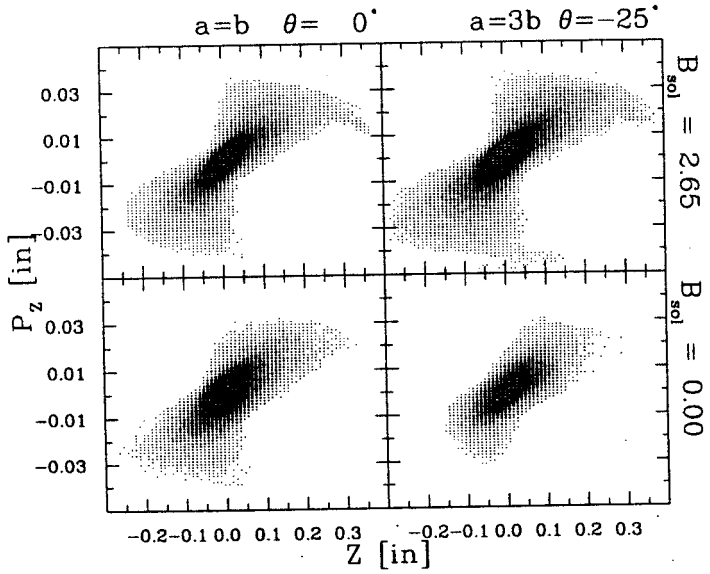

(b) z-p_z Density Plots After 11 Turns

Figure 2.25: z-p_r and z-p_z After 11 Turns.
Once again, the spot size is smaller without the solenoid. Matching the starting ellipses also continues to produce a smaller beam emittance. In z-p_r the unmatched cases produce a correlation which is removed with injection emittance matching.

Table 2.1: K1200 Cyclotron DC Acceptance.
Injection efficiencies are presented for the four 4-D DC acceptance studies. See text for explanation.

Case 1:				
$B_{sol} = 0.0$	$I_{inflector}$	=	60.5%	I_{start}
$\epsilon_{xx'} = 100\pi$ mm·mrad				
$a = b$	I_{exit}	=	89.1%	$I_{inflector}$
$\epsilon_{yy'} = 100\pi$ mm·mrad	I_{CR}	=	11.9%	I_{exit}
$a = b$		=	10.6%	$I_{inflector}$
		=	6.4%	I_{start}
Case 3:				
$B_{sol} = 2.65$	$I_{inflector}$	=	99.5%	I_{start}
$\epsilon_{xx'} = 100\pi$ mm·mrad				
$a = b$	I_{exit}	=	100.0%	$I_{inflector}$
$\epsilon_{yy'} = 100\pi$ mm·mrad	I_{CR}	=	12.0%	I_{exit}
$a = b$		=	12.0%	$I_{inflector}$
		=	11.9%	I_{start}
Case 5:				
$B_{sol} = 0.0$	$I_{inflector}$	=	76.0%	I_{start}
$\epsilon_{xx'} = 100\pi$ mm·mrad				
$a = 3b$	I_{exit}	=	95.4%	$I_{inflector}$
$\theta = -25°$				
$\epsilon_{yy'} = 100\pi$ mm·mrad	I_{CR}	=	12.3%	I_{exit}
$a = 3b$		=	11.7%	$I_{inflector}$
$\theta = -25°$		=	8.9%	I_{start}
Case 6:				
$B_{sol} = 2.65$	$I_{inflector}$	=	100.0%	I_{start}
$\epsilon_{xx'} = 100\pi$ mm·mrad				
$a = 3b$	I_{exit}	=	96.7%	$I_{inflector}$
$\theta = -25°$				
$\epsilon_{yy'} = 100\pi$ mm·mrad	I_{CR}	=	11.4%	I_{exit}
$a = 3b$		=	11.0%	$I_{inflector}$
$\theta = -25°$		=	11.0%	I_{start}

a percentage of the current of the previous stage. The four stages are at the start, I_{start}, inside the inflector aperture, $I_{inflector}$, inside the inflector exit, I_{exit}, and at the end of 11 turns of integration through the central region, I_{CR}. I_{CR} is also presented as a percentage of all the previous stages. At the time of these studies, $I_{inflector}$ and I_{CR} could be measured. A Faraday Cup has since been installed to measure I_{start}, as well as its spacial distribution.

The dominant stage is the central region time acceptance. The 45° FWHM calculated in Figure 2.21(a) is 1/8th of the RF period. The one ratio that could be measured, I_{CR}:$I_{inflector}$, gives 1/10th to 1/9th, which is in good agreement with the calculation in all four cases. The use of the solenoid to focus the beam into the inflector, cases 3 & 4, can eliminate practically all the losses incurred on the inflector apertures and electrodes. Matching the injection phase space ellipses improves this slightly. Between cases 1 & 6, without the focussing, is where matching can be seen to make a significant improvement in the transmission, increasing both the acceptance in the entrance aperture, and the transmission through the inflector. All told, for this one operating point, matching, by itself, can improve the total transmission into the cyclotron by 39%, and with the use of the solenoid, the transmission can be increased a by a total of 86%. This is 95% transmission during the central region's open time aperture, for a 100 π mm·mrad injection phase space, without space charge.

It is good to remember, though, that the focussing solenoid in the axial injection line can not be used since the beam needs to exit the 90° dipole off-axis to be injected into the K1200 cyclotron. The fact that the transmission into, and the beam inside the cyclotron, can be improved by matching the injection phase space will still be true, but the amount that the present injection can be improved is unknown.

2.4 TRANSMISSION STUDY WITH BUNCHING

The buncher was depicted in the axial injection line in Figure 2.2. It was designed after the Argonne Low Energy Buncher[52] It is capable of being driven at both 1st and 2nd harmonics of the RF accelerating voltage. The gap, which is 1.7 m from the median plane, consists of two wire meshes, spaced 7 mm apart, each of which can be driven independently. At the edge of the meshes, the electrodes extend out in a cone, with the entrance cone extending vertically for ~5 cm, and the exit cone extending vertically for ~10 cm. The radius of curvature of ions when entering the central region is always 7.95 mm. Thus the cones extend over the distance a particle travels in two RF periods for 2nd and 1st harmonics, respectively. This should average out the effect of the electric fields while approaching and leaving the buncher, so these portions will be left out of the buncher approximation.

The buncher gap is short enough, 7 mm, compared with the distance traveled in one RF period, 50 mm, that it can be treated as an instantaneous impulse on the beam. Equation 2.8 in Section 2.1.7 gave the small gap approximation which was added to MYAXIAL to represent the buncher. A buncher voltage of 1% of the ECR extraction voltage, gives the optimum tuning of this buncher formula for a gap of 7 mm and a drift of 1.7 m. Particles traveling on axis in the injection line should respond to the buncher like they were drifting, until they reach the inflector, where they will take different paths due to the energy spread imparted by the buncher. Figure 2.26 shows the time distribution of particles at the exit of the inflector, which were started on axis at the buncher, with the buncher voltage set at 1% of the ECR extraction voltage. There is little difference in the final result for these particles from those in an equivalent drift section, so the straight section optimization will be used to select the initial buncher voltages. Typically, the buncher is tuned to

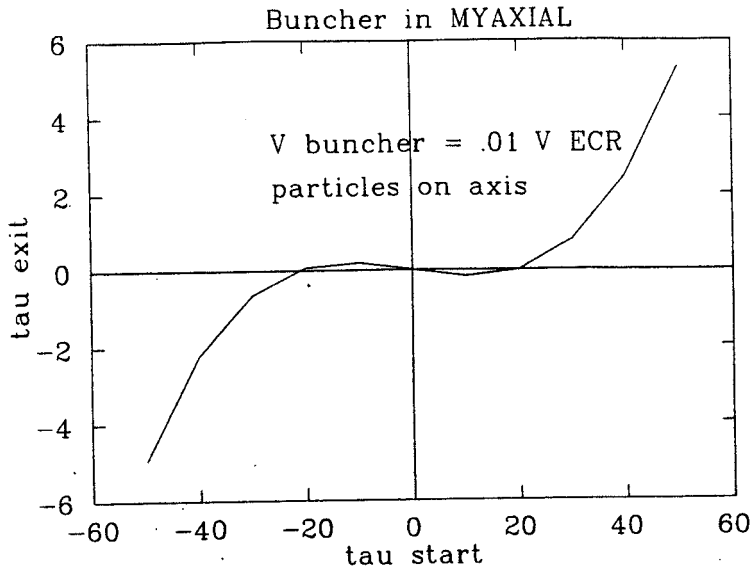

Figure 2.26: Buncher Test in the Program MYAXIAL.
A test of the small gap buncher approximation added to MYAXIAL. Particles traveling on axis should respond as if a drift followed the buncher, except for chromatic terms in the inflector. The approximation works correctly.

a value greater than this, overbunched, to maximize the current injected into the cyclotron, with the total current being increased by a factor of three[9].

2.4.1 Debunching in the Yoke

It is well known that particles travelling in a magnetic mirror towards increasing B, with $|v_\perp| \neq 0$, transfer kinetic energy from $v_\parallel$ to $v_\perp$[51]. This is true even when the field is not adiabatic, and the particles are not reflected by the mirror. This is the situation for the injected beam as it enters the solenoidal field of the cyclotron. The rate of travel of the particles will decrease if $|v_\perp| \neq 0$, with the rate of decrease being greater for greater initial values of $v_\perp$. These particles will take longer times to reach the inflector.

This behavior is shown in Figure 2.27, where the 4-D pulses used in cases 1, 3, 5, & 6 were assigned the time $t = 0$ as they crossed the plane of the buncher, which

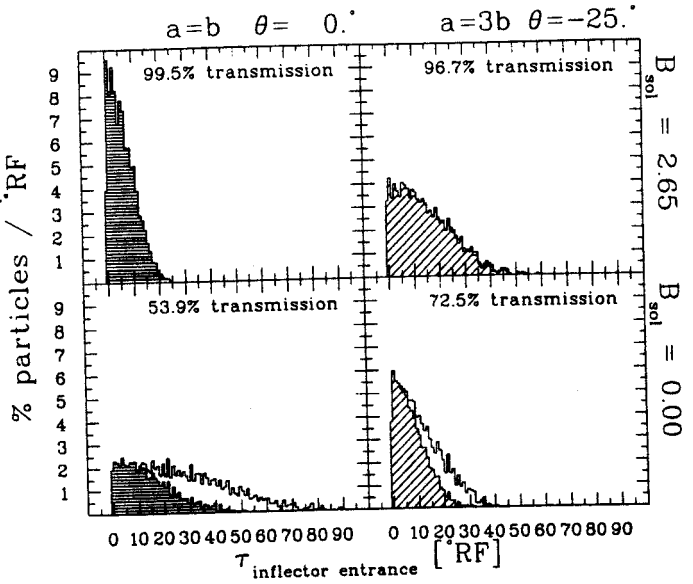

Figure 2.27: Debunching During Traversal of the Yoke.
The debunching of the four 4-D pulses as they travel from the buncher to the inflector entrance. The shaded portion is the fraction which is transmitted through the inflector. Matching the injection phase space, upper left and lower right, minimizes the debunching in the yoke. Using the solenoid to improve transmission also helps reduce the debunching in the yoke.

was turned off. This Figure demonstrates that both the solenoidal focussing, and the phase space matching are necessary when minimizing the debunching of the beam in the yoke. Using a smaller initial phase space would be the only way to further reduce this debunching, but that can only occur by throwing away a significant portion of the beam extracted from the ECRs.

2.4.2 Debunching in the Spiral Inflector

Marti showed that the spiral inflector used in the NSCL cyclotrons will debunch particles on the edge of a 100 π mm·mrad ellipse, an amount comparable to the debunching due to the yoke[36]. Figure 2.28 presents the total debunching that has occurred in the pulses shown in Figure 2.27, as they exit the inflector. The inflector has greatly expanded the tails, and significantly rounded off the tallest peak. The

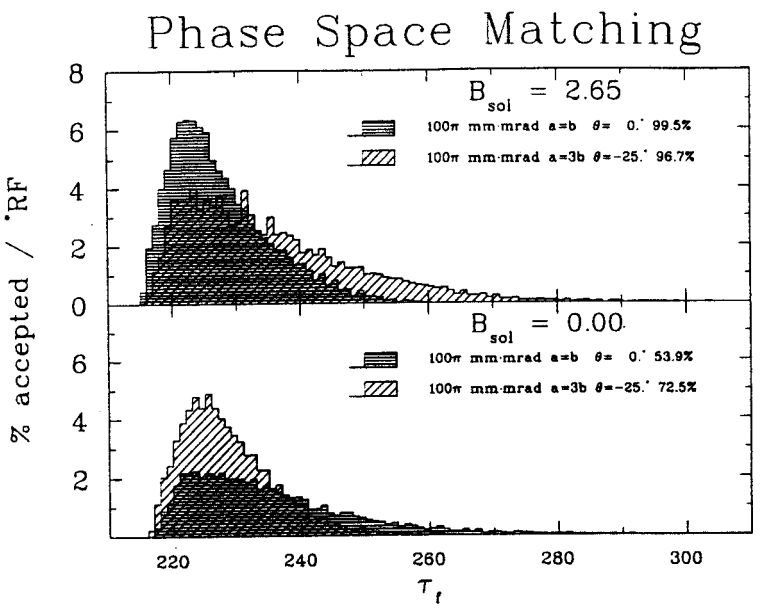

Figure 2.28: Total Debunching from the Yoke and Inflector.
The pulses displayed in Figure 2.27 have been followed to the inflector exit, with the phase of the buncher adjusted to put the axial ray with $\sin(\phi) = 0$ at $\tau = 220°$RF. The inflector has rounded off the peaks, significantly reducing the most focussed peak, and greatly extending all of the bases, leaving the FWHM approximately the same in each case.

FWHM though, has not been significantly changed for any of the starting conditions. This is because the debunching in these beams is dominated by the large initial phase space. Case 3, with the matched solenoid, where the debunching in the yoke has been minimized, is the case that is most significantly affected by the inflector.

This debunching presents an intrinsic limit on how tight the buncher can bunch the beam. Obtaining beam phase cuts narrower than these peaks will require that the peaks themselves be cut, with significant reductions in the intensity of the beam. Also, the buncher should not be tuned on the central ray, since the peak lags behind the central ray, and the center of the FWHM lags behind the peak.

2.4.3 Bunching Through the Spiral Inflector

To study the time properties of the buncher, a finer grid was used in time than in the DC studies. The grid in time, was reduced from a uniform spacing of every 5°

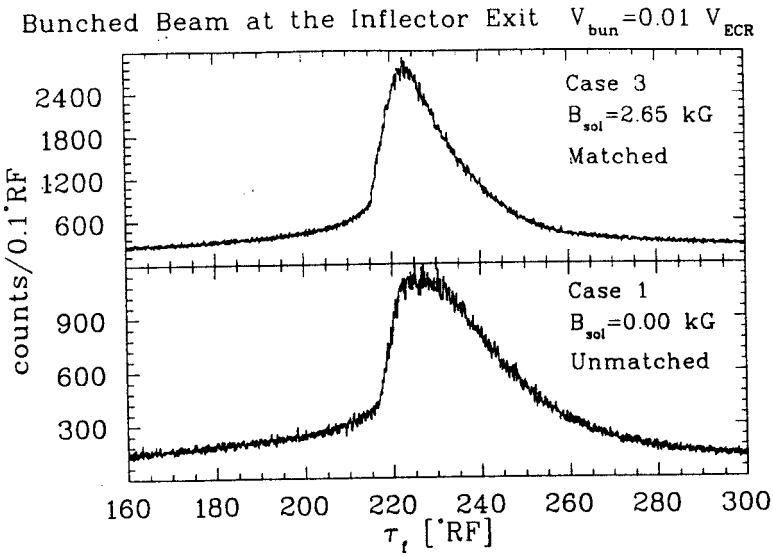

Figure 2.29: Bunched Beam at the Inflector Exit.
Intensity vs time at the exit of the inflector, for bunching cases 1 & 3 with $V_{bun} = 0.01 V_{EC}$. The peak width in both cases is due to the debunching demonstrated in Figure 2.28. Case 1 is for the normal injection settings used with the 'standard' operating point. Case 3 was focused with the solenoid, and matched the injection phase space, minimizing the debunching.

RF, to a uniform spacing of every 2° RF. To fully accommodate the buncher, this grid was extended to 135 grid points, representing a range of 270° RF. With the need to raytrace over 1 million particles for each case studied, the bunching study was limited to the two extreme cases. Case 1, with the poorest transmission, and not matched, is used to represent the real conditions for this operating point, and case 3 is used to represent a best case. It is possible for other operating points to be as good as case 3, or worse than case 1.

Figure 2.29 shows the the bunching of these beams at the exit of the inflector, using the same buncher voltage as above, 1% of V_{ECR}. The difference in these peaks is due solely to the debunching in the yoke and the inflector.

There is one minor modification to the phase space of the beam as it exits the inflector. Using $V_{bun} = 0.01 V_{ECR}$, adds a time dependent energy spread to

the beam. The more energetic particles are deflected by a slightly smaller amount when they travel through the spiral inflector. The beam then paints the exit phase space, adding a very small, starting time dependent, coherent oscillation inside the cyclotron.

Finally, the phase of the buncher, with respect to the accelerating RF, needs to be adjusted for transmission through the central region. This will be left for later, in the phase slit simulations.

CHAPTER 3

USING A Si PIN DIODE AS A TIMING DETECTOR

It was necessary to develop a new timing detector for the K1200 cyclotron. A considerable amount of effort had been put into detector development for the earlier MSU cyclotrons[7, 8, 27]. An interesting aspect of the PIN diode used by Milton to detect gammas, was that it sometimes was struck by heavier particles which left stronger signals[53]. If a detector could be made which would directly detect the beam, which consists, after all, of heavy ions, it would have the best chance of overcoming the noise from inside the cyclotron. (There are many gamma, x-ray, and neutron sources inside, as well as the RF itself.) There is also a lot of experience in nuclear physics in using solid state detectors for measuring E, ΔE, and sometimes t, in nuclear reaction by-products. A drawback is that these solid state detectors have a low count rate capability, though the K1200 injection line can accommodate this by attenuating the injected beam current, using a grid system, by as much as 6 orders of magnitude. Solid state detectors are damaged by heavy ions, Knoll estimates that Si detectors fail after $\sim 10^8$ incident heavy ions per square centimeter[54]. Si PIN diodes, being relatively inexpensive, were chosen to study the 'test of principle', and having succeeded as an external beam time detector, a specially designed Si detector was manufactured for testing and use inside the cyclotron.

3.1 EXPERIMENTAL DESCRIPTION

Three different types of Si detectors were used in external beam studies. The first, 5 mm × 5 mm × 300 μm, was used simply to show that a Si detector could be used to measure beam time spectra immediately outside of the cyclotron. The second type, two Hamamatsu 18 mm × 18 mm, 300 μm thick Si PIN photodiodes, was used to measure detector resolution, and to make measurements covering the entire beam cross sectional area. The last type, two transmission mounted, Micron Semiconductor, 3 cm × 3 cm × 300 μm, totally depleted ion implanted structure, Si detectors, was used in a TOF measurement as part of an atomics physics experiment[55]. The electronics and data taking programs developed from an ad-hoc adaptation of pre-existing equipment, to a dedicated setup with a specially written program to control data taking and display. The following descriptions of the electronics and data taking program will only cover the final configuration.

3.1.1 The Detector

The detectors were all operated in reverse bias, at full depletion. When an ion passes through the silicon, it excites electrons, taking 3.6 eV to create each electron-hole pair[54]. These pairs are then collected on opposite sides of the detector, the total charge collected being proportional to the energy deposited in the detector. (Heavy ions leave such intense tracks of electron-hole pairs, that the resulting plasma partially shields itself from the electric field, allowing some of the pairs to recombine, and lengthening the collection time[54].) The rapid rise in current during collection is then used as a reference for when the ion struck the detector. This fast signal has a rise time of 5 ns.

This reference signal is then compared to a second signal generated by the cy-

clotron's RF system. In this way, the position of each particle striking the detector is determined in time in such a way that it can be converted to a relative RF phase for use in cyclotron studies.

While possible, it would have been difficult to turn this measurement into an absolute measurement of RF phase. The RF signal is taken from a pickup loop which is inside the resonator of dee C. Before an electronic measurement of the absolute RF phase could be made, the phase of the signal in the pickup loop, relative to the voltage on the dee, would have to be calculated at each frequency for which data is taken. Then after measuring the propagation time of every cable, which is temperature dependent, and the processing time of each piece of electronics, an absolute measurement of the RF phase could be made.

Instead, when an absolute measurement was needed, a technique developed by Smith & Garren was used to get a reference point[56]. This technique, which will be explained in Section 3.3, consists of detuning the frequency, a somewhat lengthy process, until $\sin(\phi) = +1$ at some radius, and also to $\sin(\phi) = -1$ at the same radius. The relative position of the operating frequency to the two measured frequencies directly determines the operating value of $\sin(\phi(r))$.

3.1.2 The Electronics

A schematic of the detector electronics is shown in Figure 3.1. The bias on the detector, and its guard ring, is provided by a Tennelec Dual High Voltage Power Supply, Model TC953A, which is mounted in an Ortec 401A NIM bin in the operator's control room. The charge on the detector, is collected with a charge-sensitive Tennelec TC178 Quad Preamplifier, which is in the vault near the detector. Mounted immediately before the input into the charge-sensitive preamplifier is a LBL Time-

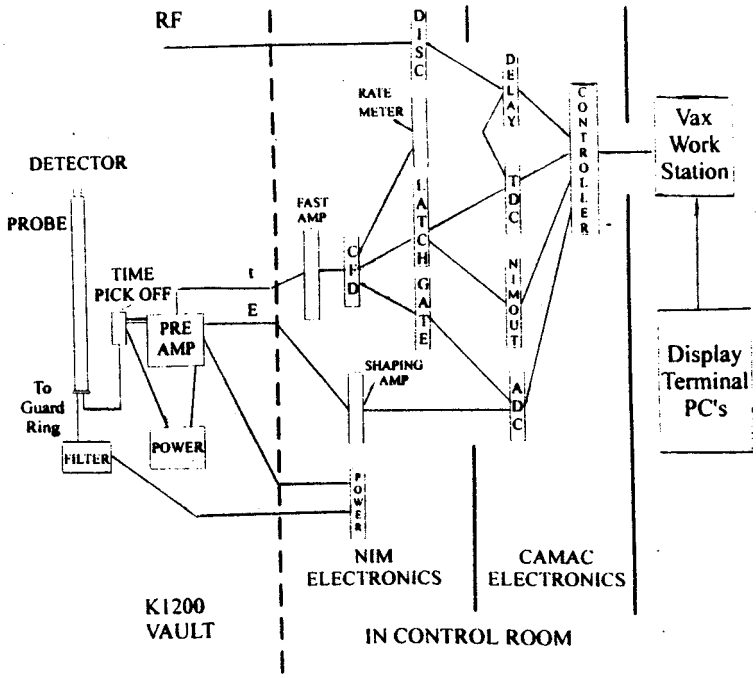

Figure 3.1: Timing Detector Electronics Schematic.
The general schematic of the electronics used to collect and process time and energy signals from the K1200 timing probe. The signal collection is controlled from a VAX computer, and the final spectra are displayed on a terminal, usually a PC. See text for a detailed explanation.

Pickoff fast amplifier. It uses a transformer to read the high frequency part of the signal coming from the detector, and amplifies it so that it can be sent to a remote location. Also in the cyclotron vault is a low pass filter, built in house for the guard ring power line. To accommodate the length of the probe on which the detector is mounted, and to allow for its travel, 25 feet of a thin coaxial Lemo cable is needed to connect the detector to the time pickoff, and the guard ring to its filter. This adds to the detector capacitance when estimating the detector noise. The external measurements did not have this problem. Homemade amplifiers mounted in the probe head immediately after the detector would be a better solution, provided that they are well shielded from the accelerating RF, and can survive in the harsh conditions inside the cyclotron (high radiation and a strong magnetic field.) As it

is, the electronics in the cyclotron vault are in a sizable magnetic fringe field. The signals from the two amplifiers, one proportional to the energy deposited, the other for the time, are then fed to the control room for processing.

In the NIM bin in the control room, the time signal is amplified again in a Phillips Scientific Model 778 fast preamplifier. A Tennelec Model TC455 Quad Constant Fraction Discriminator (CFD) is then used to uniformly determine the time of arrival of each pulse. (This is true for pulses of different amplitude, but not necessarily so for those of different shape. The CFD is set with a constant fraction of .2 and a delay of 3.3 ns.) Several output signals are then taken from the CFD, both of which are sent to a LBL designed quad gate and delay generator (QGDG). The leading edge of the first turns on a Latch which is turned off after all the signals have been processed. The output of the latch is used, in another portion of the QGDG, to create a gate signal whose leading edge represents, in a Time to Digital Converter (TDC), the time of arrival of the particle in the detector. The second output signal of the CFD is also used to create a gate which is delayed to coincide with the processed energy signal when it arrives in an Analog to Digital Converter (ADC). Also in the NIM bin is a Tennelec TC241 amplifier which is used to amplify and shape the energy signal before it is sent to the ADC. The final CFD output, when not being used to tune the CFD, is sent to a Tennelec TC526 rate meter, which is monitored for detector safety, and sometimes for intensity information.

The TDC, a Lecroy Model 2228A, and the ADC, a Lecroy Model 2259B, are mounted in a Kinetic Systems Model 1502 CAMAC crate (Computer Automated Measurement And Control.) (Both converters have ~2000 channels. The TDC is set at 100 ns full scale, and the ADC has a full scale of -2 V.) Also in the CAMAC crate are a BiRa Model 3251 NIM Out and a Lecroy Model 2323A Programmable Dual Gate Generator (PDGG). The RF signal, which has been converted to a NIM

pulse in an ORTEC Model 436 100 MHz Discriminator, is delayed in the PDGG and then sent to the TDC (necessary to prevent an overlap of signals in the TDC.) The TDC then uses the time signal as its start, and the RF signal as the stop, and digitizes the quantity ($t_{RF} - t_{detector}$). Both this value and the value of the energy, from the ADC, are transferred to a VAX Workstation by a Kinetic Systems Model 3929 SCSI Crate Controller. Having processed the data, the CAMAC program sends a signal to clear the Latch via the NIM Out module. In this manner, overlapping time signals will be ignored, but they can still pile up in the energy measurement.

3.1.3 A Data Collection and Display Program

The data taking program was written in a collaborative effort by Au, Marti, and the author. The data collection portion is actually a separate program which controls the CAMAC modules from the VAX. A portion of its memory is shared in common with the data display program. Through this 'mailbox' the data display program instructs the data collection program to start, stop, and clear, as well as reading the histogrammed output for data analysis. The graphics output of the data display program is written in GKS and needs X-Windows to run. It has two graphics windows, displaying the current spectra in the top window, and comparing it with up to 10, differently colored, stored spectra in the bottom window. These stored spectra can be current spectra which have previously been stored, or saved spectra which have been read in from the disk. Any of the stored spectra and the current spectra can be written to disk, saving them for subsequent analysis. Interesting portions of the spectra can be expanded to fill the whole window. The data collection can be switched from an accumulative mode, which can accrue sufficient counts to obtain good statistics, to a tuning mode, which speeds up tuning by automatically erasing the old spectra each time the data collection side completes a new histogram

(1024 counts.)

The ease of use of the graphical interface, together with spectra comparisons and the tuning mode, make the data taking and display program a rapid and efficient way of measuring and tuning the time spectra inside the cyclotron. The only drawback is the lengthy set up time required to install the probe containing the detector, and tune the detector electronics. Once this is done, everything else works quickly. A 1 nA $^{40}Ar^{10+}$ beam can be attenuated in the grid system to as low as 206 counts/sec. At this rate a new spectra is accumulated every 5 seconds in tuning mode. (Usually the attenuation is set to obtain several thousand counts/sec. The data collection program is limited to 1 histogram/sec., but it is not slowed down by excess counts, so this allows the beam to be cut by slits without impeding data taking.)

3.1.4 Results with the External Timing Detectors

Measurements taken with the external beam were very promising. Figure 3.2 is from alpha particles that passed through both of the Hamamatsu detectors. The resolution of each detector, including the electronics, was 310 ps FWHM, after correcting the two detector measurement by $1/\sqrt{2}$. This is the equivalent of 1.5° RF for the 13.5 MHz frequency used to accelerate the 40 MeV/u beam.

Figure 3.3 was also taken with these detectors and 40 MeV/u alpha particles. It was taken using the buncher set at several different phases, Φ_b, with respect to the accelerating voltage. They are clean sharp spectra showing distinct structure. With allowances made for the cuts in the beam made by the central region, and the cuts and possible spreading made by the extraction system, they reproduce the bunched beam calculations of Figure 2.29, for the exit of the inflector, very nicely.

These results were sufficiently promising, that the design of an internal timing

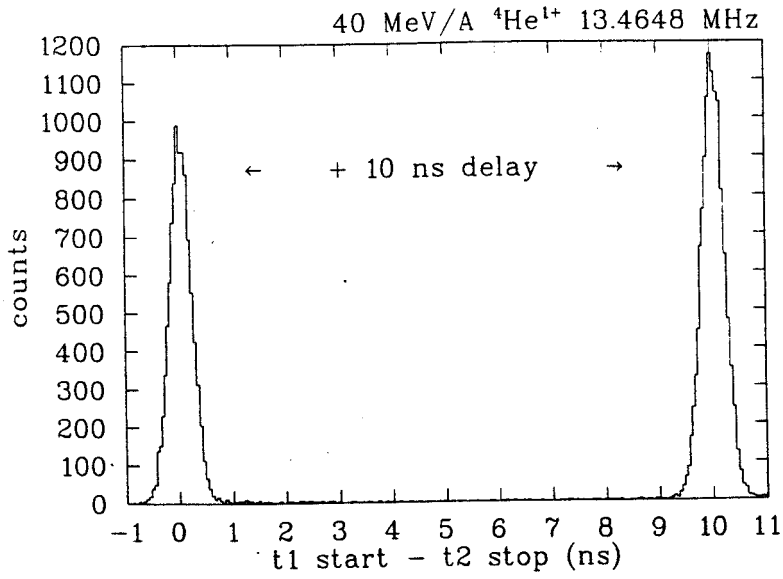

Figure 3.2: Resolution of the Hamamatsu External Detectors.
The resolution of the Hamamatsu detectors was measured to be .31 ns FWHM. The measurement was taken using the signals from α's which pass through both detectors. The signal from the first detector was used as a start, and the signal from the second detector was used as a stop.

probe, using a detector similar to the external detectors, was embarked upon.

3.2 USING THE DETECTORS ON K1200 PROBES

As was depicted in Figure 1.1, the K1200 cyclotron has two radial probe drives, labeled A2 and A5. These were designed such that the probes themselves are interchangeable. There are several current probes, and a TV probe that views a scintillator inserted into the beam[33, 57, 58]. The timing probe complements the existing probes, allowing different aspects of the beam to be tuned and studied.

Figure 3.4 shows the timing probe head. The middle picture is fully assembled, looking at the detector through a hole in the copper shield. The shield was an attempt to hide the detector from the internal RF fields. The hole allows the beam to strike the detector first. The top picture depicts the detector mount, and the bottom picture is a cut away, which shows vacuum seals, signal feed throughs, and

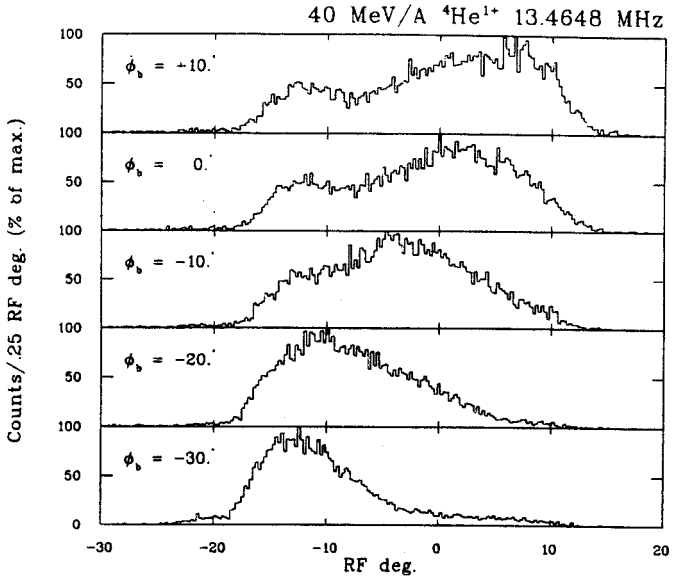

Figure 3.3: Bunched Beam Measured with the Hamamatsu External Detectors.
Beam spectra measured with the external beam using the Hamamatsu detectors. The various spectra have the buncher set at different phases which were calibrated with respect to the accelerating voltage. The RF phase (x-axis) is relative not absolute. Compare these spectra to the calculation in Figure 2.29.

the maximum angle of incidence of the beam on the detector (necessary for the A2 drive.) Since the beam spot is typically only a few millimeters high, the detector has an active area of 1 cm^2.

While it too can work in either drive, for convenience, all the measurements made with the timing probe were done on the A5 drive, depicted in Figure 3.5. The angle of incidence of the beam on this drive is typically 28° to 30° over the whole of its range, which is shorter than the range of the A2 probe.

The path of the A5 probe, instead of being truly radial, would, if extended, pass tangential to a circle of 16.351 inch radius. The center of the dees spiral out at a rate of -4.40737° /in, to 39.2 in, where they curve outwards to maintain a constant azimuth. The time measurements taken with the timing probe need to be corrected from the position of the probe head, to the dee center, which is the phase reference point. To do this, equilibrium orbits are run in the design magnetic fields to get

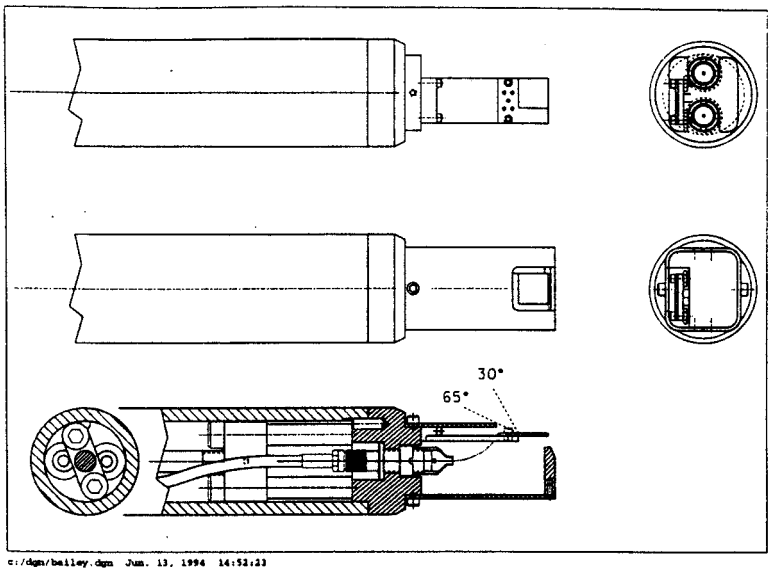

Figure 3.4: The K1200 Timing Probe Head.
Details of the timing probe head assembly are shown. Also included in the picture, are the detector mount, the copper RF shield, the vacuum seals, and the vacuum feed throughs for the detector signals. The angles depicted on the lower cut away show that the beam will clear the shield for the range of incident angles incurred when used in drive A2. In drive A5 it is typically, 28° to 30°.

the time of travel from the center of the dee, assumed always to be a spiral, to the probe. The result is displayed in Figure 3.6. Note that this correction, though used for all measurements, is no longer valid past 39.2 in, where the dees no longer spiral and this correction is overpredicted. The result will be that the corrected ϕ is too small.

3.2.1 Detector Modifications for Use Inside the Cyclotron

Any probe operating in the outer radius of the cyclotron requires an active area which extends nearly to its outermost edge. This is because the beam's radius gain per turn can be as small as .5 mm before crossing $\nu_r = 1$. To overcome this defect, two specially built detectors were purchased from the Senter for Industriforskning in Norway (Center for Industrial Research.) These detectors were built with normal guard rings, and then they were cut, one just outside the innermost guard ring,

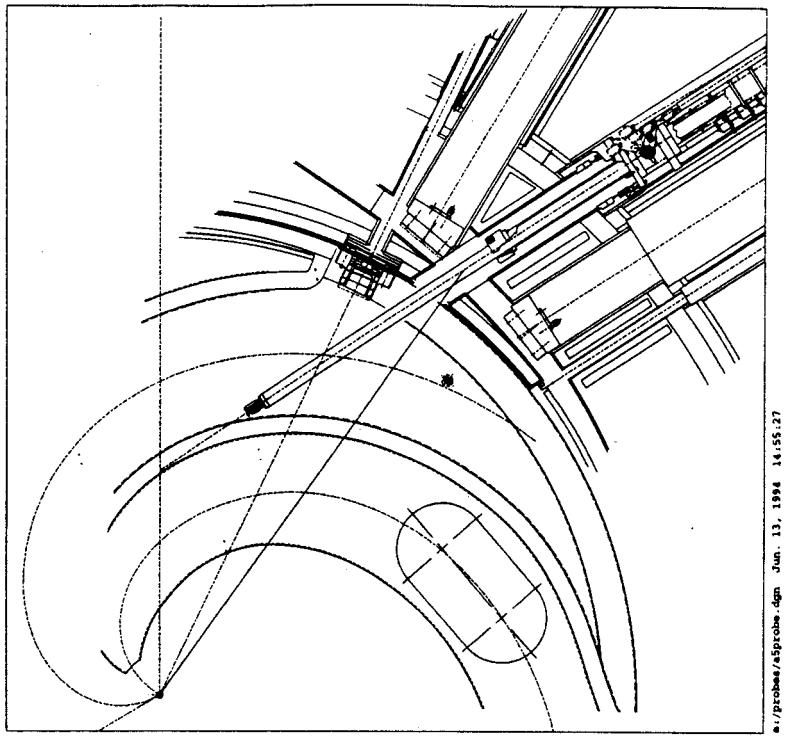

Figure 3.5: The K1200 A5 Probe Drive.
The A5 probe drive is shown with the probe fully extended. It is inserted into the gap between the grounded pole tips. The point in the lower left corner is the machine center, with the two spirals approximating the centers of the dee and hill. Note how the probe approaches the accelerating gap.

the other just inside this same guard ring. These cuts are depicted in Figure 3.7. Table 3.1 lists the detector characteristics before cutting, and Table 3.2 lists these same characteristics after cutting and mounting. Compared to an uncut reference detector, the cuts have raised the leakage current in the guard rings of both detectors by three orders of magnitude. Without the innermost guard ring, the leakage current in the active area has a similar increase. These cuts leave a dead area that is at most 190 μm, sufficiently small enough to detect the beam at any radius.

The detector with the outside cut was tested first. It had the same response as the detectors discussed previously. The fast signal had the same shape, complete with the same 5 ns rise time. A resolution test was not conducted on this detector, but Figure 3.8 is a spectrum that was taken with this detector. It is from an analog,

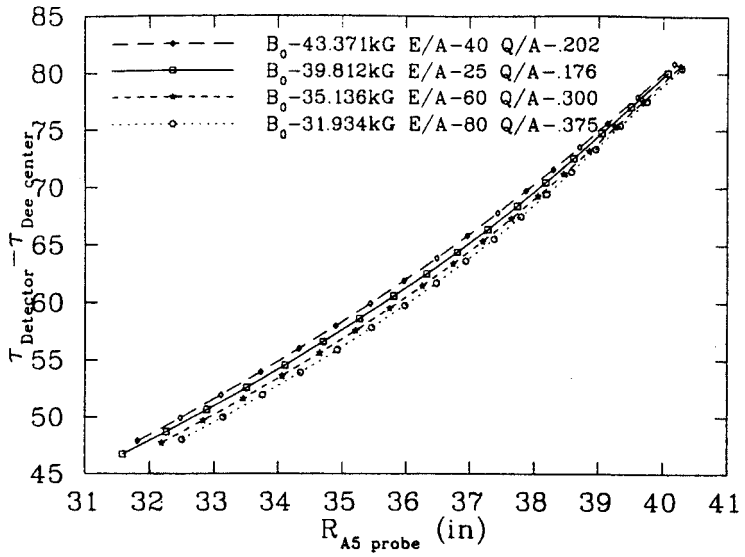

Figure 3.6: Time Corrections for the A5 probe.
The calculated time of travel in RF degrees is presented as a function of the A5 probe radius. The variation of a couple of degrees from different operating points is primarily a function of B_0. With the iron fully saturated, the contribution of the pole tips remains constant. Thus the flutter decreases with increasing B_0, reducing the scalloping of orbits for these settings.

$^{63}Cu^{18+}$, of the intended beam, $^{28}Si^{8+}$. With a slightly different charge to mass ratio, .286079 as opposed to .285995, the copper ions have slipped -80° away from the silicon ions. After one more inch, it will no longer gain sufficient energy to clear the detector's dead area. It is believed that the multiple peaks in Figure 3.8 are a consequence of the beam precessing in radial phase space due to an off centering of the beam. (Only one time can be truly centered at any given radius.) With only a couple of turns of each precessional cycle having sufficient radial separation to clear the dead area, and the turn number at which the ions strike the detector being a function of phase, see Equation 1.2, the result is a multi-peak structure in phase. $d\phi/dn$ at this radius is not large enough to cause this separation, but may be causing an apparent change of the total phase width measured by the detector. Note that many of these peaks have a FWHM of 200 ps, an indication of the detector resolution achievable with this detector. Figure 3.9 shows the full spectra from which these

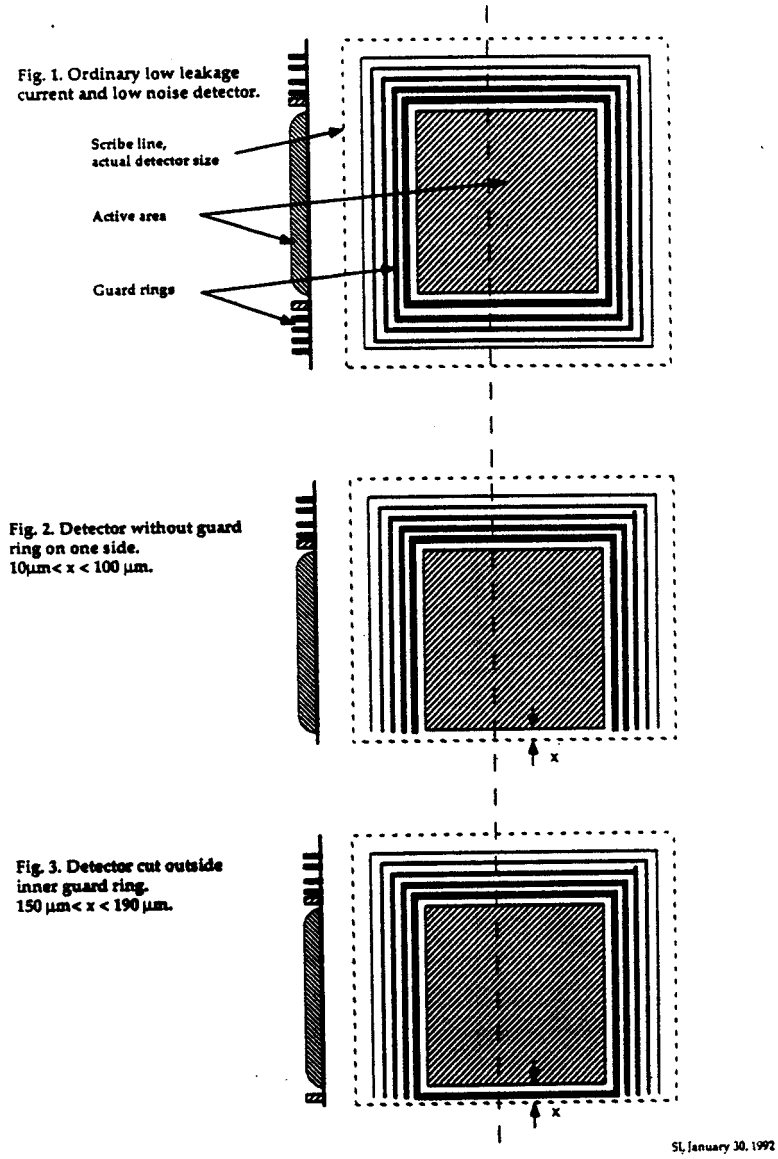

Figure 3.7: Detector Modifications Made by SI for Use Inside the K1200 .
The position of the two different cuts in the detector guard rings are depicted above. These cuts were necessary for use inside the K1200 cyclotron, where the radius gain per turn can be as low as 0.5 mm. Pictures are courtesy of Lars Evenson of the Senter for IndustriForskning, Norway.

Table 3.1: Detector Characteristics Prior to Cutting.
Measurements made prior to the detector modifications for the two specially manufactured detectors and a reference detector. This table courtesy of Lars Evenson of Senter for Industriforskning, Norway

Device	Bias Voltage	Active Current	Guard Current
Uncut	40 V	65 pA	650 pA
Cut outside inner guard ring	50 V	35 pA	509 pA
Cut inside inner guard ring	50 V	65 pA	560 pA

peaks were taken. Using both the phase separation at these radii, and the amplitudes of the energy deposited in the detector, the three peaks were identified as $^{63}Cu^{18+}$, $^{35}Cl^{10+}$, and $^{28}Si^{8+}$ (left to right.)

The detector cut inside the inner most guard ring also proved to be useable. Like the other detector, its fast signal has a rapid rise time, 6 ns. As the peak decayed, though, it had an extended shoulder. It is as if there is a second rapid change in the current occurring shortly after the current begins to be collected at the detector sides. The purpose of the guard ring is to maintain the electric field uniformly throughout the active area, and to reduce the leakage current from the detector active area. The propagation velocity of the electrons and holes are each dependent on the strength of the local electric field, so the collection times will be affected by this change. The CFD works with the leading edge of the signal, so this substructure on the tail does not adversely affect the time measurements. Measurements from both detectors will be used hereafter without distinguishing their source.

Table 3.2: Detector Characteristics after Cutting and Mounting.
Measurements made after the detector modifications for the two specially manufactured detectors and a reference detector. This table courtesy of Lars Evenson of Senter for Industriforskning, Norway

Device	Depletion Voltage	Active Current	Guard Current
Uncut	40 V	1.3 nA	2.4 nA
Cut outside inner guard ring	35 V	38 pA	18 μA
Cut inside inner guard ring	40 V	4.0 μA	4.3 μA

3.2.2 Detector Simulation

A constant fraction discriminator works by inverting and delaying the signal, then adding it to the original signal which has been reduced to a fraction of its original amplitude. The zero crossing then occurs at a constant fraction of the maximum amplitude. This reduces a significant portion of the walk in the signal caused by differing amplitudes. Indeed, for signals of the same shape, this walk is nearly eliminated.

The internal probe can take measurements of the beam over the range of .625 E_{max} to E_{max}, and the beam passes through the detector at an angle. So for various ions and energies, the beam may always punch through the detector, with the deposited energy decreasing as a function of radius. Or, the beam may always stop in the detector, in which case the deposited energy and the depth of penetration will both increase as a function of radius. In this case, the signal shape itself could vary, causing some walk in the CFD. Or, it may be a combination of the two previous cases. For any of the above, some ions will cross through the front

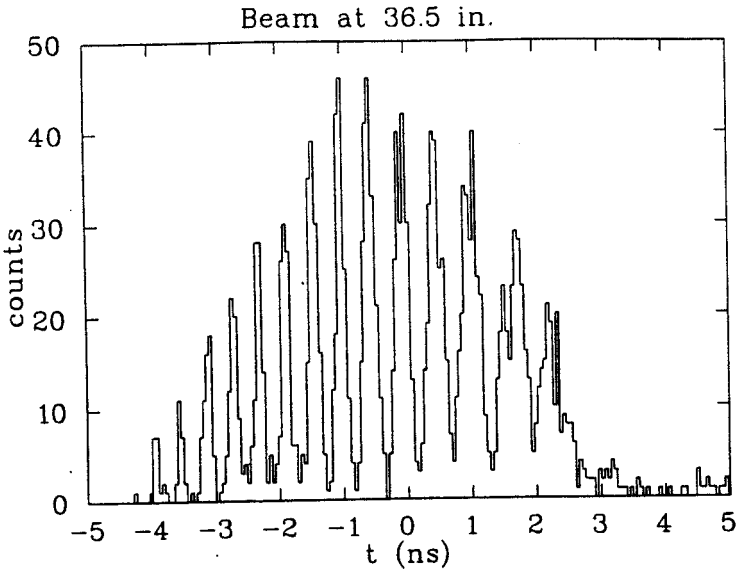

Figure 3.8: Extreme Precessional Effects and Internal Detector Resolution.
A measurement made with the timing probe illustrating that the resolution is at most 200 ps FWHM. This beam is an analog close enough in q/m to the design beam that it survives past 36 in. It is far enough out of phase, giving it a low energy gain per turn, that it needs the betatron precession to clear the dead area at the edge of the detector. This provides thin cuts in time.

corner of the active area, while others can traverse the entire detector thickness.

To simulate these effects, the program ELOSS[59], written by Winger at MSU, was used to obtain the energy loss profile for several different ions incident on the detector with different initial energies. (100 MeV/u $^{36}_{18}Ar^{6+}$, 40 MeV/u $^{40}_{18}Ar^{10+}$, 30 MeV/u $^{129}_{54}Xe^{23+}$, and 25 MeV/u $^{40}_{18}Ar^{7+}$. Each was run from .6 E_{max}/u, just below a radius of 32 in, to E_{max}/u.) A simple model of the detector, developed by Spieler[60], was then used to simulate the collection of charge from the detector.

Approximate the electric field across the fully biased detector as a linearly decreasing field with

$$\mathcal{E}_{min} = \frac{V_b - V_D}{D}, \tag{3.1}$$

where V_b is the bias voltage, V_D is the depletion voltage, and D the thickness of the

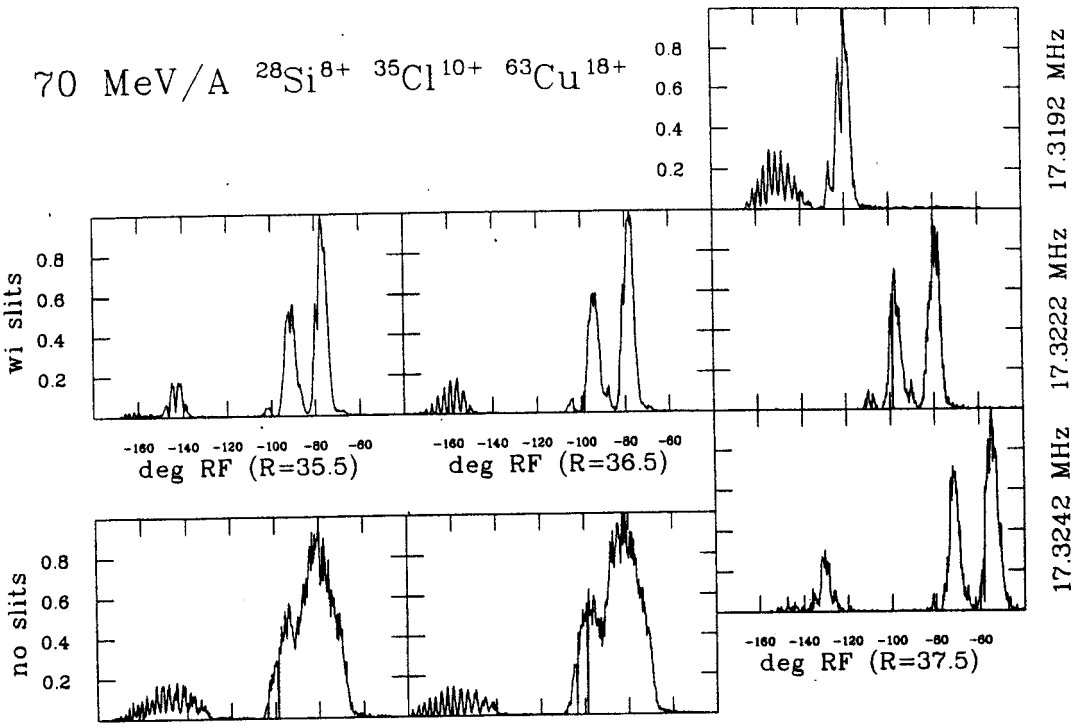

Figure 3.9: Analog Beam Time Spectra.
The full time spectra for 70 MeV/u $^{28}Si^{8+}$ and two analog beams, measured with the internal timing probe. The relative spacing in time, together with relative energy signals enabled the identification of the three peaks, which are from right to left, $^{28}Si^{8+}$, $^{35}Cl^{10+}$, and $^{63}Cu^{18+}$. Figure 3.8 is a close up of the lower left corner of the bottom middle spectra.

detector. The maximum field is then

$$\mathcal{E}_{max} = \frac{2V_D}{D} + \mathcal{E}_{min}. \tag{3.2}$$

The velocity is then $\vec{v}(x) = \mu \cdot \vec{\mathcal{E}}(x)$, where at low fields, $\mathcal{E} \leq 2.5 \cdot 10^3$ V/cm, in room temperature silicon, and μ_- is 1350 cm^2/Vs, and μ_+ is 480 cm^2/Vs[60]. (All of these detectors were operated under these conditions.)

This detector model was then used as a current source in a simple integration circuit to simulate the signal from the detector. These signals, which reproduced the detector fast signal, complete with 5 ns rise time, were input into a CFD simulation with a fraction of .2 and a delay of 3.3 ns. Figure 3.10 shows the calculated time

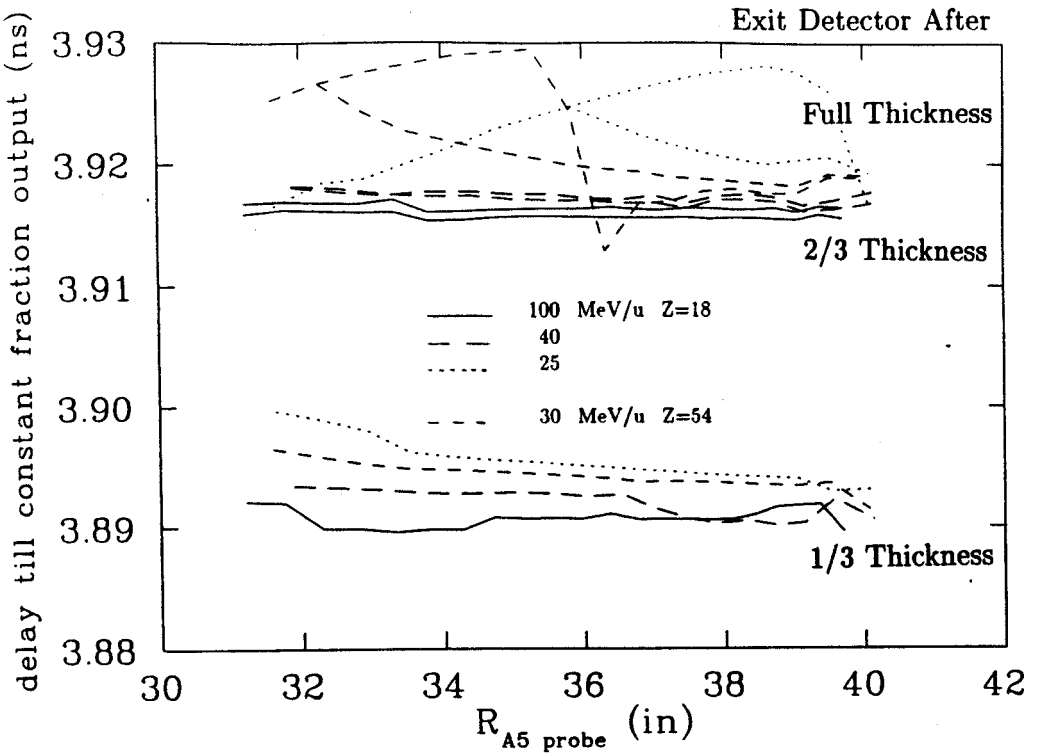

Figure 3.10: Calculated Constant Fraction Output.
The time to reach a .2 constant fraction, including the 3.3 ns delay, for particles leaving the detector after travelling through 1/3rd (lower set), 2/3rds, and 3/3rds (upper two sets) of the detector thickness. Each set uses the internal energies of 100 MeV/u $^{36}_{18}Ar^{6+}$ (solid), 40 MeV/u $^{40}_{18}Ar^{10+}$ (large dash), 30 MeV/u $^{129}_{54}Xe^{23+}$ (small dash), and 25 MeV/u $^{40}_{18}Ar^{7+}$ (dotted) extracted beams. The 2/3rds and 3/3rds cases are practically identical except when the Bragg peak exits the detector. The 1/3rds case will add slightly to the FWHM of a measurement.

delay between the constant fraction input and output signals from this simulation. The solid lines are for the 100 MeV/u, the large dashes for the 40 MeV/u, and the dotted lines for the 25 Mev/u calculations, each of which was for $Z = 18$. The small dashes are for the 30 MeV/u, $Z = 54$ calculation. The lower grouping is for those particles leaving the active area after traversing 1/3rd of the detector thickness, while the upper groupings are for those particles exiting after 2/3rds of, and the full detector thickness. The upper four curves demonstrate the mixed condition, where the particle gains enough energy to punch through the detector. This calculation shows that electronic response will be relatively the same for both

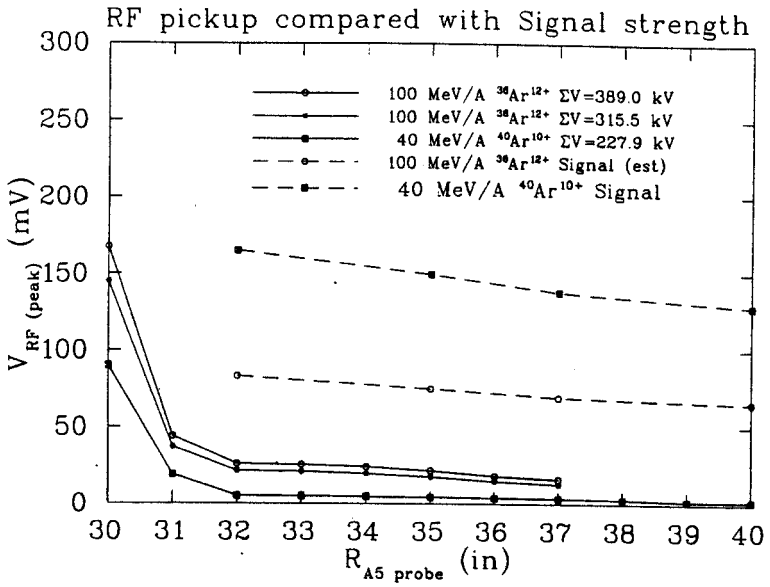

Figure 3.11: Detector RF Pick-Up and Signal Strength.
Measurements of the timing signal and RF pick-up are compared as a function of the A5 probe radius for two beam energies. Inside of 32 in, the RF pick-up increases rapidly, rendering the timing detector useless. Outside of 32 in, the detector works best for low energy heavy ions, but still works over a large fraction of the K1200 operating diagram.

energetic medium sized particles, and slow heavy particles. There will also be a slight broadening caused by the small fraction of particles which pass through the tip of the leading corner.

3.2.3 Signal Variation and RF Pickup

As was previously discussed, the signal strength will vary with radius. A close look at Figure 3.5 shows that the A5 probe approaches an accelerating gap as it travels towards smaller radii. The detector, which is essentially a parallel plate capacitor is open to the electric field which penetrates the vertical gap in the hill. With the accelerating voltage in the range of 50 to 200 kV, even an exponentially attenuated field can be strong enough to mask the signal. Figure 3.11 shows the relative strengths of the RF pick-up signal and the time signal of the detector as a function of the A5 probe radius, measured, after the LBL time pick-off, in the

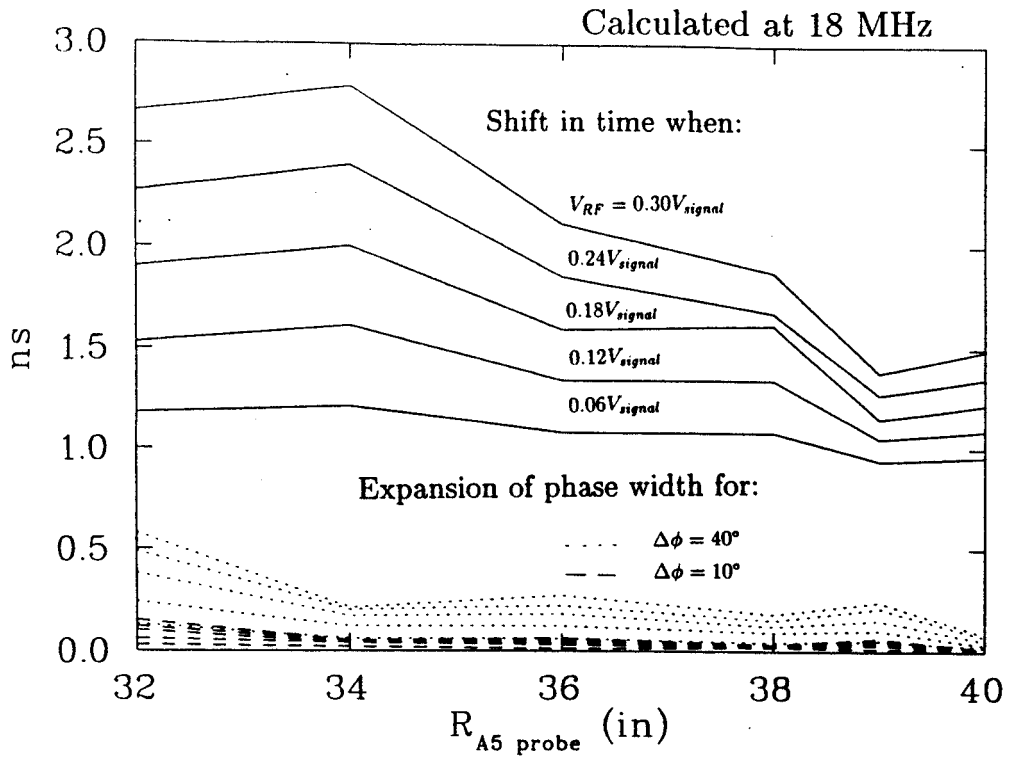

Figure 3.12: Shifts in Time from the RF Pick-Up.
Calculated shifts in time from adding a small sine wave to the detector signal. Calculated at 18 MHz with $V_{RF} = .06 — .30\ V_{signal}$. The solid curves are the net shift, and the lower curves are the relative expansion when $\Delta\phi = 40°$ (dotted line), and $\Delta\phi = 10°$ (dashed line). The radial differences in the net shift from the RF pick-up may need correcting in phase curve measurements. The relative expansion at worst adds 10% to the measured widths.

control room. In all cases, inside of 32 in, the amplitude of the RF pick-up increases exponentially. This makes the region of innermost travel of the A5 probe, 28 in to 32 in, unusable for the timing detector. For the 40 MeV/u measurement, the signal is so much stronger than the pick-up, that the RF has no effect on the measurements. With the signal decreasing and the accelerating voltage increasing as the beam energy goes up, the 100 Mev/u measurement is no longer unaffected. This effect can be calculated, and resolves itself into two components, which are shown in Figure 3.12. The first is a shift in the measured time of the spectra, which because of the path of the probe, together with the radially changing phase curve, is dependent on the probe radius. The change of this shift as a function of radius can distort phase

curve measurements. These signals should always be measured, and when necessary, the correction should be calculated. The second part is a result of different phases in one bunch having different net shifts. This will cause a small expansion of the measured phase widths.

3.2.4 Multi–Turn Collection and Beam Centering

Multi-turn collection on the detector was introduced in an extreme case in Figure 3.8. In that picture, with the number of turns in a precession cycle being $1/|\nu_r - 1|$, and with $\nu_r \approx 1.1$, it took $\sim$150 turns to collect the entire beam bunch. Normally, multi-turn collection is not so drastic. It will still have an effect on the timing measurement, though not so pronounced. Calculations made with central rays spaced every 5° in τ_0, from 185° to 235°, show that at 32 in, it takes $\sim$20 turns for the A5 probe to collect a beam bunch. As the probe is withdrawn, this increases to $\sim$35 turns. (These calculations were made with the 'standard' beam, and were done to get a sense of how the probe works. The results for other operating points will vary.)

To see how precession will change measurements made under normal conditions, the time of arrival on the probe was calculated for these central rays. The central ray with $\tau_0 = 220°$ was centered in these calculations. Figure 3.13 shows the separation in the times at which a few of these starting times strike the detector. The phase width, which was compressed in the central region, shown in Figure 2.20, has remained constant inside the rest of the cyclotron. The sawtooth structure seen in the time spread of the particles is from the precession of the off centered ions. Note that this occurs even for small phase spreads, if the orbits are off centered. At 32 in, the normal $\sin(\phi)$ curve is rising, and at 36 in, it is falling. Comparing the time spreads at these two places, one sees that the measurements will be, respectively, expanded and compressed under these conditions.

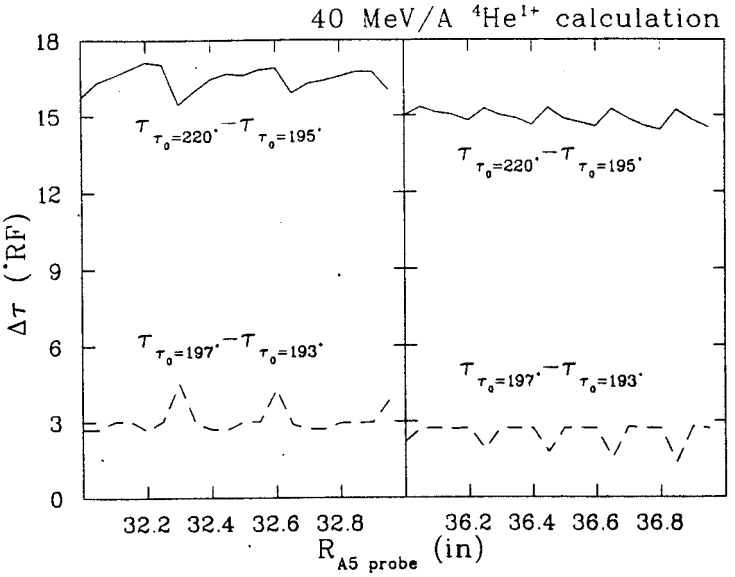

Figure 3.13: Precession Effects on Relative Time Widths.
The betatron precession of off centered times in the beam cause a periodic variation in the measured time separation of ions in the beam. Depending on the location along the phase curve of the measurement, this effect can be compressive or expansive.

These multi-turn and precessional effects will cause a small uncertainty in the width and location of phases measured inside the machine. The precession is a byproduct of the betatron motion, and multi-turn collection is machine dependent. Therefore these effects can occur in measurements made in any cyclotron.

3.3 PHASE CURVE MEASUREMENTS

One of the uses of the timing probe is the measurement of $\phi(r)$. Figure 3.14 is one such measurement. A technique developed by Smith and Garren[56] was employed to turn the relative phase measurements of the timing probe into an absolute phase measurement. Let $\omega_{RF} = (1+\epsilon)\omega_0$, then

$$\acute{\Omega}(E) = \frac{(1+\epsilon)\omega_0}{\omega} - 1 = (1+\epsilon)\Omega(E) + \epsilon. \tag{3.3}$$

Making sure that the beam is not lost at an interior radius, adjust the frequency, ω_{RF}, until half of the initial intensity is lost. Repeat in the opposite direction. Then

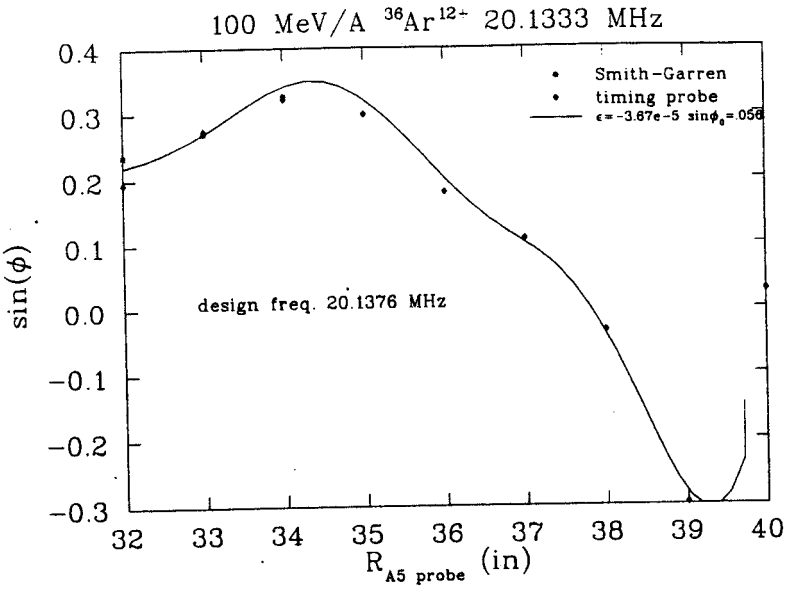

Figure 3.14: A K1200 Measured Phase Curve.
The relative phase curve was measured with the timing probe, and set in absolute coordinates with a Smith-Garren RF detuning measurement. The measured curve was then fit with the output from the design settings in MONSTER, using the frequency error, ϵ, and $\sin(\phi_0)$ as parameters in the fit.

from using $\acute{\Omega}(E)$ and $\phi = \pm 90°$ in Equation 1.6,

$$1 = \sin(\phi_0) + (1+\epsilon_+)\frac{2\pi h}{qV_0}\int \Omega(E)dE + \epsilon_+\frac{2\pi h}{qV_0}\int dE \tag{3.4}$$

$$-1 = \sin(\phi_0) + (1+\epsilon_-)\frac{2\pi h}{qV_0}\int \Omega(E)dE + \epsilon_-\frac{2\pi h}{qV_0}\int dE \tag{3.5}$$

$\sin(\phi(r))$ can now be calculated. It is :

$$\sin(\phi(r)) = -\frac{(\epsilon_+(r)+\epsilon_-(r))}{(\epsilon_+(r)-\epsilon_-(r))} \tag{3.6}$$

This was done for three of the points at which data was taken, and all the data points, which are the spectra centroids, were then shifted accordingly. The solid line through the data points is a fit of $\Omega(E)$ from the magnetic field output by MONSTER, the program used to design the operating settings for this beam. The exact voltage used inside the cyclotron is unknown, but it is approximately the design voltage. Using this voltage, the frequency was slightly lower than optimum,

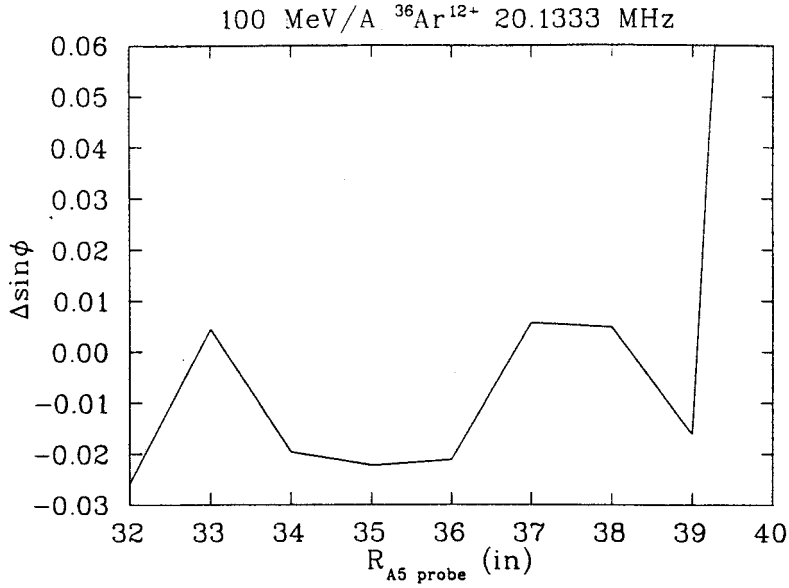

Figure 3.15: Differences in the Measured and Fit Phase Curves.
The difference in the measured and fit $\sin(\phi)$ curves of Figure 3.14. The difference is invalid past 39 in, since the fit curve did not extend to the last measured point (40 in.) The variation in the rest of the curve is $\pm 1°$, so it is unknown if the structure is real, or just random measurement error. The $\sin(\phi)$ measurements are a close fit to the design field.

$\sim$700 Hz. The optimum frequency is 3.6 kHz lower than the design frequency, implying that the magnetic field is 0.018% low.

The fit of the calculated curve to the data is very good. Figure 3.15 shows the differences in these curves. The variation here is from +.3° to -1.5° , except for $r > 39$ in. The calculated and measured magnetic fields are very close in shape. If more data points had been taken, the shape could be derived from the data by,

$$\frac{\Delta B}{B} = \Omega(E) = \frac{qV_0}{2\pi h}\cos(\phi(E))\frac{d\phi}{dE}. \tag{3.7}$$

which is from Section 1.3.

The use of this detector is well understood, and it performs satisfactorily, provided that the ion being studied has sufficient large Z to leave a large signal.

CHAPTER 4

PHASE SLITS

Phase slits, following the design of those used by Milton in MSU's K500 cyclotron were installed in the K1200 cyclotron. The use of these slits in the more stable K1200 , with measurements using the new timing detectors, together with comparisons to the multi-dimensional ray-tracing simulations begun in Chapter 2, has resulted in a confirmation of the manner in which the slits function, and a better understanding of their limitations.

4.1 SLIT PLACEMENT AND DESIGN

The K1200 yoke was machined with 6 vertical access holes in the center of the hills. There is one hole through each upper and lower pole tip, to maintain both the 120° rotational symmetry, as well as the vertical symmetry about the median plane of the magnetic field. The location of these holes, at ~7.00 in radius, was constrained by the spacing between the trim coils. The copper RF liner currently has apertures for only 2 of the vertical hole pairs. The lower hole in one hill is used for a current probe, which is often referred to as the 'phase slit probe', because of its location. To avoid confusion, the radial probe built to measure the phase spectra, see previous chapter, has been labeled as the 'timing probe'. Of the remaining three holes, access to the other lower hole is restricted by a gate valve in the injection line (visible above

the buncher in Figure 2.2.)

Opening the holes in the remaining hill would require the removal and machining of parts of the center plug, which during construction were only machined for the first two hole pairs. (These iron pieces are sufficiently removed from the median plane that they do not significantly impact the 3–fold symmetry in the median plane.) Their use would also require machining new holes in the liner, which also serves as a vacuum liner. These changes could cause hard to trace and hard to fix vacuum leaks, they are time consuming, and would require shutting down the cyclotron. This is considered undesirable, and would be done only if necessary.

This leaves only two holes which could be used to deploy the phase slits. Fortunately, they are on separate hills. Their location above the cyclotron median plane requires that no oils or fluids be used in the drives, since a leak would contaminate the accelerating cavity.

The 'slits' used in the K1200, are Milton's off-centered pins mounted on rotatable shafts, see Section 1.3. The pins are made of tungsten and are soldered onto a removable copper head, allowing pins with different thicknesses to be used on the same shaft. The copper heads are designed such that the outermost edge of the pin is 3/8ths of an inch from the shaft center. The pins used in the present measurements of this study have a diameter of 0.094 in. The radius gain per turn at the position of the phase slits is $\sim$0.16 in.

The shafts, with a 1.00 inch O.D., are hollow stainless steel, with a smaller internal tube that provides cooling water to the shaft head. The water leaves through the outer shaft, which is soldered vacuum tight to protect the K1200 vacuum integrity.

The shaft drive, depicted in Figure 4.1, a slight modification of Milton's design, is mounted on the K1200 cap. On the top is an air cylinder which through the flow

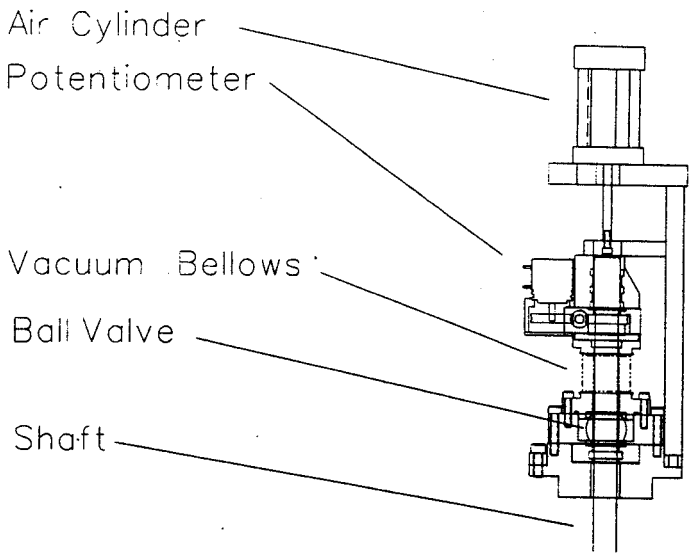

Figure 4.1: K1200 Phase Slit Drive Schematic.
The slit drives have five basic functions. They are to 1) seal this exit of the K1200 vacuum chamber, 2) enable the rapid changing of phase slits while still under vacuum, 3) insert and retract the phase slits, 4) rotate the phase slits, and 5) provide rotational feedback to the control electronics. See the text for a description on how this design accomplishes these goals.

of high pressured air inserts and retracts the shaft. When retracted, the drive can be locked in place, and the air cylinder removed, allowing the removal of the shaft. The drive also provides a vacuum seal for the accelerating cavity. With the shaft installed, an O-ring immediately above the bellows provides the vacuum seal. When removing the shaft, a special fixture is used to stop the shaft before the head clears the O-ring. In this position, the pin is within the bellows, allowing a ball valve to be closed, which maintains the seal on the vacuum. The shaft can then be completely removed. This procedure enables a rapid changing of the pins.

The rotation of the shaft is driven by an external motor, which coupled to a worm gear, simultaneously rotates both the shaft, and a 5–turn potentiometer. The potentiometer provides the location feedback necessary to accurately control and report the angular rotation of the pin. The motor is an electronic stepping motor which is mounted 8 ft above the cap, inside iron shielding. The horizontal section

of the drive shaft uses two coupling bellows to allow for the vertical motion of the slits.

4.2 CALCULATED SLIT PERFORMANCE

The initial studies of the K1200 phase slits, done with Rifuggiatto[35], showed that each individual slit would function in the manner described by Milton[8], cutting the beam on two consecutive turns. Figure 4.2 shows simulations of cuts made on one starting time, $\tau_0 = 216°$, assuming slits on all three hills. The positions and diameters of the pins were selected to completely fill the gap between the r-p_r phase spaces on two consecutive turns of starting time $\tau_0 = 220°$. The ellipses are accelerated equilibrium orbit eigenellipses, with an initial area of 100π mm·mrad , as they appear on successive turns at each hill center. The orbits were calculated by SOMA[26]. The initial conditions of the ellipse were calculated with Equation 2.5, in order to minimize the differences in energy gain within the ellipse. The different shapes and positions of the eigenellipses on each hill are a measure of the nonuniformity of the magnetic field and of the orbit's off centering at this radius.

At the slit radius,

$$\int_{\tau_0=216} \sin(\phi) dE \; < \; \int_{\tau_0=220} \sin(\phi) dE \; < \; 0, \tag{4.1}$$

so the time shown, $\tau_0 = 216°$, has a smaller total energy than that of $\tau_0 = 220°$, and its radial cut is made on the outside edge of the pin. Figure 4.2 also demonstrates a less obvious function of the slit's azimuthal spacing. Orbits bound by focussing forces revolve around a fixed point in phase space. In the case of acceleration, the orbits circulate around the accelerated equilibrium orbits (A.E.O.) The angle subtended by this revolution about the A.E.O as the particle advances an amount $\Delta\theta$, is $\nu_r \frac{\Delta\theta}{2\pi}$. Near the phase slits, $\nu_r \sim 1$, thus between every hill, the particles

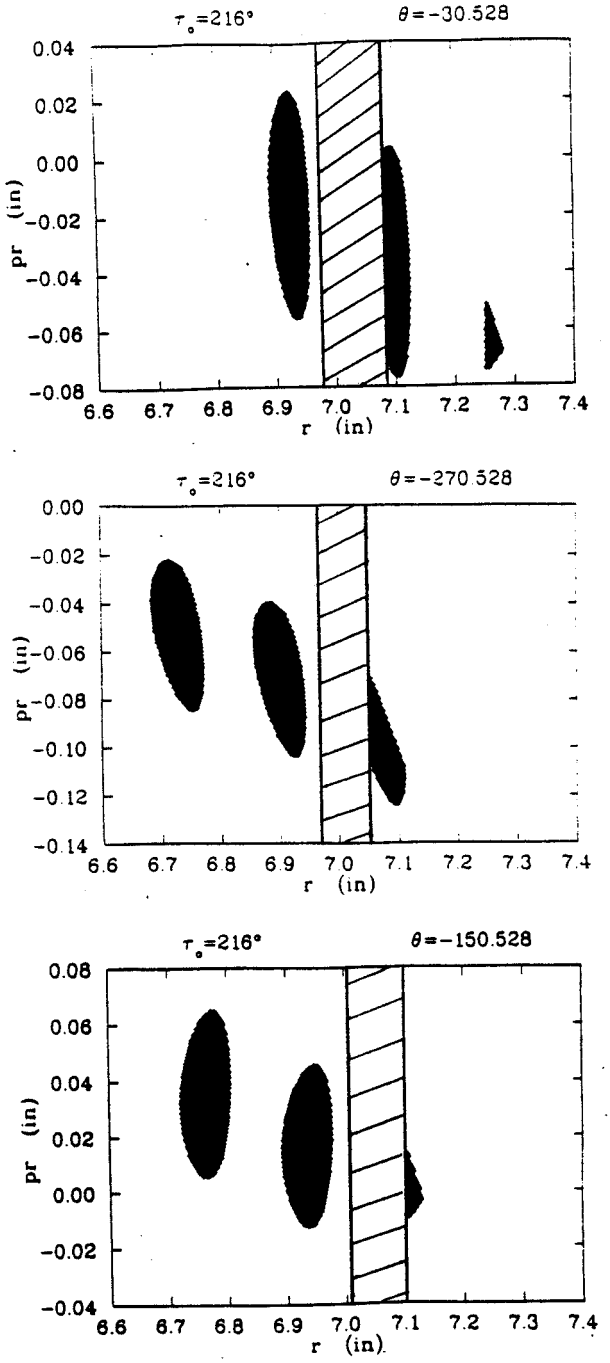

Figure 4.2: Phase Slit Cuts in r-p_r Phase Space.
Calculated cuts in an initially 100 π mm·mrad eigenellipse in r-p_r phase space about the accelerated equilibrium orbit with $\tau_0 = 216°$. A slit was used on each hill, with the position and width of each slit adjusted to barely pass all of the eigenellipse about the $\tau_0 = 220°$ central ray. Notice how the slits each cut a different portion of the ellipse. The angle of rotation of the particles in r-p_r phase space is $\nu_r \Delta\theta$. Here $\Delta\theta = 120°$, and ν_r is near to 1. (Calculation by D. Rifuggiatto)

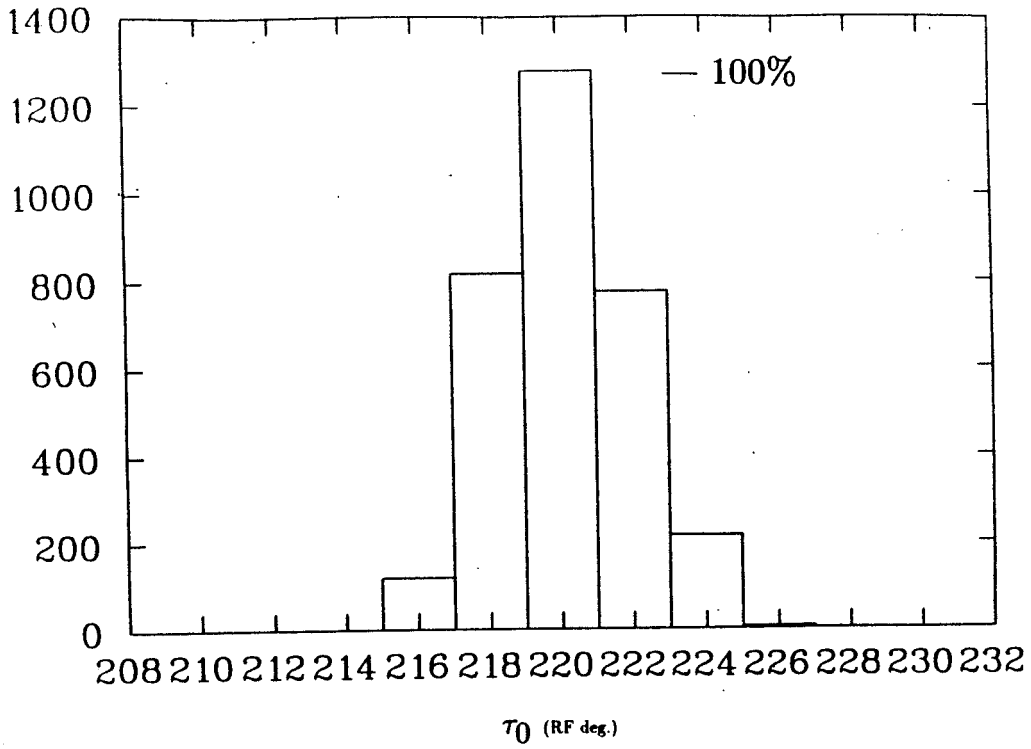

Figure 4.3: Preliminary Calculation of the Slit Transmission.
Total transmission for a range of starting times, $\tau_0 = 210$ to 236, calculated as in Figure 4.2. The slits make a nearly triangular cut in time, with a FWHM of 6° in τ_0. Any further reductions in the phase width will reduce the transmission of the peak. After the central region compression, $\Delta\phi$ is $\sim 4°$ in this calculation. (Calculation by D. Rifuggiatto)

rotate $\sim 120°$, and the next slit cuts a different area of the r-p_r phase space. This means that successive cuts on the same turn can make a cut in time that is sharper than any one slit could make by itself.

The total time cut made by this simulation, ranged over starting times $\tau_0 = 210$ to 236, is shown in Figure 4.3. It shows that this procedure will cut the beam into a nearly triangular distribution with a FWHM of 6° in τ_0. After the central region phase compression, this is 4° in $\Delta\phi$.

To further study, and more accurately simulate the cuts that the slits make in the phase spread of the beam, orbits from the 4-D bunched injection studies of Section 2.4 were continued past the slits. Only the unmatched case was used, since

this approximates the actual conditions currently used in everyday operation of the cyclotron. The radii and phase of the particles were saved at each hill, if the radius was within the range of the phase slits. These were then used in the slit simulation program described in Section 2.2. The program displays the cuts in the phase of some subsequent turn, well clear of the phase slits.

Figure 4.4 is a printout of the graphical display from the slit simulation program. In the upper left corner is the uncut phase spectra, histogrammed in 0.25° bins. Ninit is the number of particles in the calculation, with Ntotal the number of particles surviving in each frame. Nmax from the uncut spectrum is used to scale the histogram in each window. On the right side are the cuts made by each individual slit, including the hypothetical slit C (bottom). On the left side, below the uncut spectrum, are the spectra from the cumulative cuts made by slits A & B (middle), and slits A, B, & C.

Each individual pin makes many cuts in the beam, not just two! In this calculation, the beam takes as many as 6 turns to clear the phase slits. This is made clear in the r-ϕ density plots of Figure 4.5, which are used in the slit program to aid in tuning. The top graph is the distribution at slit A, and the bottom is at slit B. The vertical lines mark the outside edges of the pin settings which were used in Figure 4.4. These density plots should be compared with that in the lower left corner of Figure 2.22(b), which has the same injection settings except that the buncher was off. Note that the bunched beam has a more strongly localized center than the unbunched beam.

Several things can be learned from these two graphs. First, the injected current with the buncher is 20.7%, as opposed to 6.4% without the buncher. Second, this slit thickness, Dslit = 0.094 in, is too large to transmit all the beam of one phase. Third, the multiple peak transmission makes it difficult to obtain just 1 nice peak in

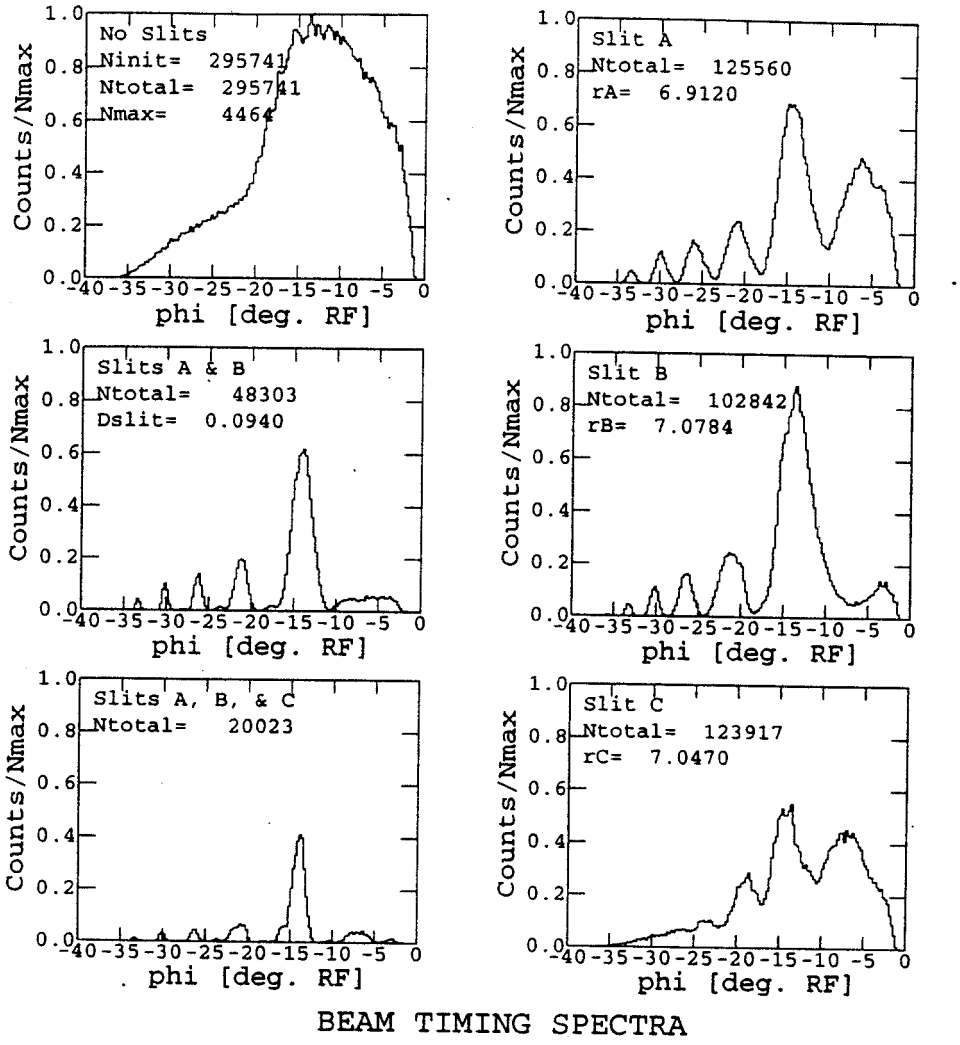

8DKA0:[BAILEY.AXIAL.ALPHA.CENTREG]CRS0B1T210SL4.DAT;1
8DKA0:[BAILEY.AXIAL.ALPHA.CENTREG]CRS0B1T210C.DAT;1

Figure 4.4: Calculated Slit Performance Using the Bunched 4-D Injection.
The phase slit cuts are simulated using the orbits continued from the bunched 4-D injection study. The cuts made by the individual slits (right column) produce multiple peaks, implying multiple turn overlap at 7 in. the phase slits are wide, cutting the peak of the transmitted beam. But, in this simulation, the resulting satellites could not be removed, even with all three slits (left column.) The buncher has increased the uncut transmission from 6.4% to 20.7%.

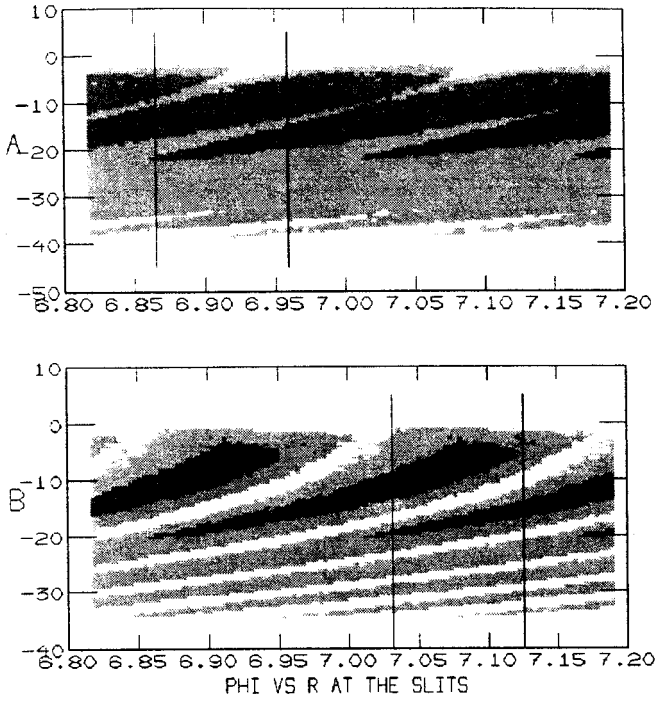

Figure 4.5: r-ϕ Density Plot Showing the Overlap of Turns.
Calculated r-ϕ density plots at the two phase slits. The tight conditions in the superconducting cyclotron have resulted in 6 overlapping turns, in radius, at the location of the phase slit. The vertical lines denote the position of the phase slits used in Figure 4.4.

time. Essentially, the small peaks of one slit need to be aligned with the valleys from the other slit, while still preserving a significant fraction of the overlap in the main peaks. These small peaks are mostly from the tail of the bunched distribution. And fourth, a slit on the third hill could not make cuts as distinctly as the two present slits. The differences are the byproduct of the beam centering. Operational conditions such as nonuniform dee voltages may put this difficulty at one of the other hills. The third slit helps narrow the cuts made with the other two slits, but can not remove the smaller satellites. Finally, narrower slits, while transmitting more of the main peak, transmit more of the satellites. Thicker slits reduce both the satellites, and the main peak transmission.

The great overlap in turns indicates that the central region transmission should

be restricted to a smaller phase width. To be properly done, such a change would require a redesign of the central region. For instance, in Figure 2.4(b) the best place to cut the beam, with nearly uniform separation in time and space for posts, is in the third turn on the hill in the lower left quadrant of the graph. But posts here would change the electric field by more distinctly separating the accelerating gaps on either side of the hill. This would slightly deflect the beam on the previous two orbits, with changes in the orbit centering, and a possible adverse effect of deflecting the beam into the back of the puller. A good slit should also be controllable, or at least capable of rapid insertion and removal for runs where the beam intensity has a higher priority than the phase width. This will be difficult to achieve in the tight confinement and limited access of the K1200 central region.

Slits could be put between the posts on the hill in the upper left quadrant, with smaller changes in the electric field. The beam is separated in time and radius as it passes through this window, but nonuniformly. To observe the general results of central region slits, the radius of the orbits were saved at this position and filtered as if a slit were installed. Figure 4.6 and Figure 4.7 were phase slit studies done with the same buncher settings as Figure 4.4, but with two different central region slit filters.

In the first, Figure 4.6, the filter was set to pass the main peak (everything between 1.35 in and 1.45 in.) The phase slits were then able to make sharp cuts in time, with a resultant two slit peak of 2.3° FWHM. The satellites are still present, but at a reduced intensity. This is because the earlier starting times do not separate much at this central region slit. So, including part of one earlier time includes part of all the earlier times. The later starting times do separate.

In the second, Figure 4.7, the filter has been moved to 1.30 in through 1.40 in. Here, we have cut the earlier times, so the central region cut is sharper, further

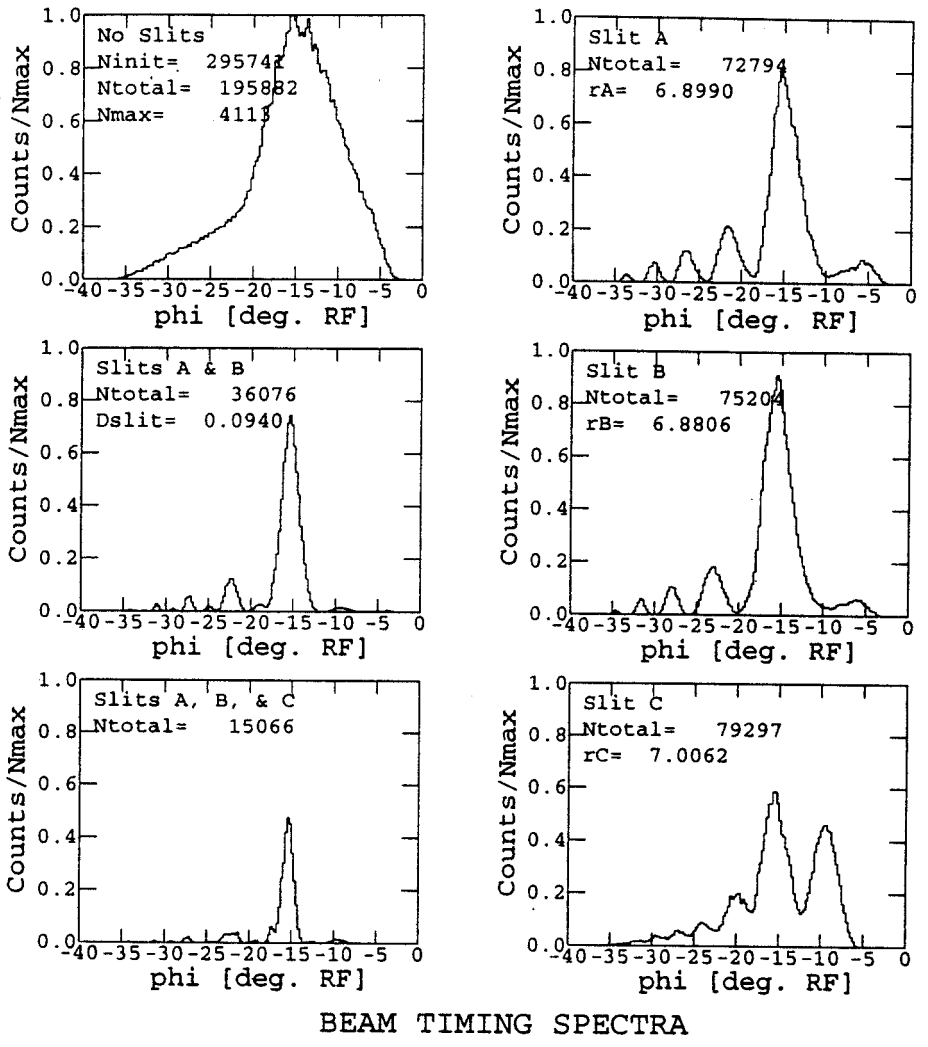

CR Slit 1.35 to 1.45 in

```
$8$DKA0:[BAILEY.AXIAL.ALPHA.CENTREG]CRS0B1T210SL4.DAT;1
$8$DKA0:[BAILEY.AXIAL.ALPHA.CENTREG]CRS0B1T210C.DAT;1
```

Figure 4.6: Calculated Phase Slit Cuts After the First Central Region Cut.
A central region cut has been used to pass the main peak of Figure 4.4. The resultant phase slit cuts transmit a narrower peak with reduced satellites, at a cost of an additional 25% in intensity overall.

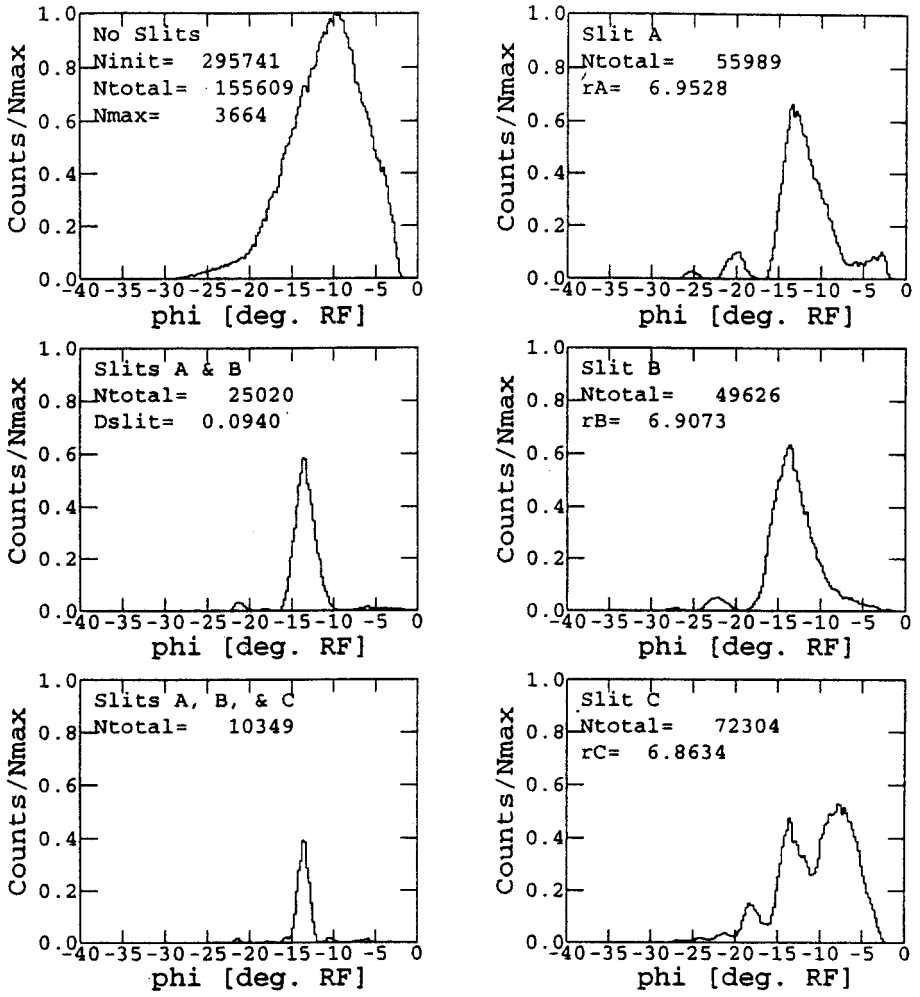

CR Slit 1.30 to 1.40 in

8DKA0:[BAILEY.AXIAL.ALPHA.CENTREG]CRS0B1T210SL4.DAT;1
8DKA0:[BAILEY.AXIAL.ALPHA.CENTREG]CRS0B1T210C.DAT;1

Figure 4.7: Phase Slit Cuts After the Second Central Region Cut.
A central region cut has been used to make a narrower cut than that of Figure 4.6. This results in fewer satellites in the phase slit cuts. The final peak is fatter here than that of the first central region cut. This is because the final position of the transmitted beam in the r-p_r diagram is closer to that of maximum energy gain.

reducing the size of the tail. This makes for fewer satellites in the phase slit cuts, allowing the slits to be positioned to remove most of these particles. This particular set up has another drawback, however, in that the beam remaining after the central region cuts is the portion with smaller values of $|\int \sin(\phi) dE|$ (smaller values of ϕ in Figure 4.5.) Under this condition, the phase slits can not make cuts as sharp as those in Figure 4.6.

A good design for the phase selection system would include the best of both simulations. A central region cut would be made at times which are spread out in radius to produce a well defined beam in time. This cut should also be narrow enough to result in separated turns at the phase slits. 10° should be sufficient. Then the phase slits could be used solely in cutting the main peak. The beam at the phase slit should also be spread out in time, allowing the slits to make sharp cuts in time to refine the phase selection. As will be demonstrated below, this is achievable through changes in the trim coil magnetic field profiles, but note that this makes turn separation at the phase slits more difficult to achieve. Estimating from Figure 4.5, for large values of $|\int \sin(\phi) dE|$, a central region cut to 5° might be necessary to preserve separated turns at the phase slits.

4.3 MEASURED SLIT PERFORMANCE

The features which dominated the phase slit calculations were also found in the measurements, but to a lesser degree. Figure 4.8 has spectra which were measured with the extracted beam at different frequencies. Even after extraction, satellite remnants remain in the beam. The calculation, however, has overestimated the difficulty in minimizing and removing these satellites. This is not conclusive, the extraction channel could be making additional cuts. The final spectra tend to be

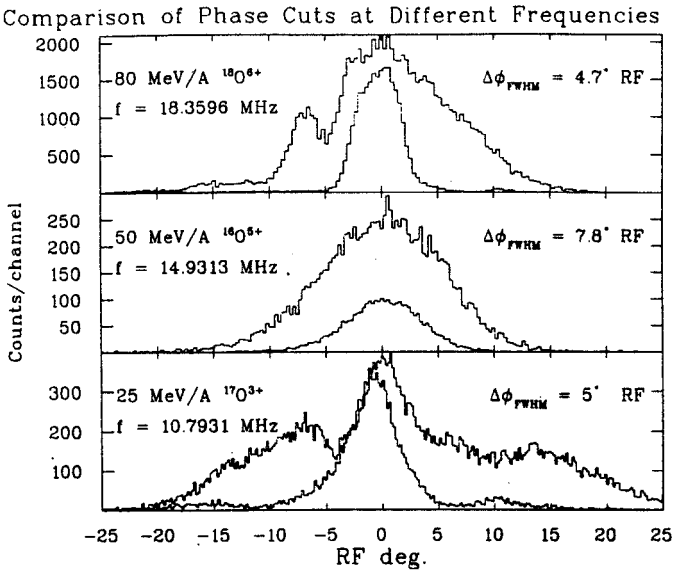

Figure 4.8: Comparison of Phase Cuts at Different Frequencies.
External measurements of the extracted beam phase width, at three different frequencies, with and without phasecuts, expressed as a function of the RF period. The areas of the cut spectra are scaled to those of the uncut spectra, using their relative extracted currents. Each is ~30% of the uncut spectra. The final RF width of the time spectra, as expected, seems to be approximately independent of the operating frequency. Theoretically, one should be able to make identical cuts at every frequency, but the initial conditions vary too widely to prove this.

more like those of the central region cuts in Figures 4.6 & 4.7.

This comparison of extracted beams also shows that the process of phase selection with the slits is relatively independent of the frequency at which the cyclotron is operated. This was an expected result, since the orbit path through the central region is the same for all ions, and the accelerating RF voltage defines most of the time processes in the cyclotron, but it was important to verify. The $\sin(\phi)$ curve in Equation 1.6 depends on the inverse of the voltage gain per turn, as well as the frequency, and the deviations of the magnetic field from isochronism. The magnetic field shape for an isochronous cyclotron does vary with final energy, since it should follow the $\gamma(r)$ curve. Also the operating points are interpolated from a mesh of premeasured fields. These things may make reproducing the $\sin(\phi)$ curve at each operating point difficult. These effects will show up in the timing cuts. There are

Table 4.1: Phase cuts and transmission.
The fractional transmission is presented for several different extracted beams using the phase slits to cut the phase width of the beam. 5° FWHM cuts are easily obtainable with 25% to 30% transmission. These are also relatively easy to maintain.

Ion	Energy (MeV/A)	ϕ_{FWHM} uncut	ϕ_{FWHM} cut	I_{cut}/I_0
$^{17}O^{3+}$	25	15.°RF	5.7°RF	.33
$^{16}O^{5+}$	50	12.7°RF	7.8°RF	.24
			6.6°RF	—
$^{24}Mg^{7+}$	60	11.°RF	2.6°RF	.25
$^{18}O^{6+}$	80	14.5°RF	4.7°RF	.30
$^{28}Si^{9+}$	80	12.°RF	4.6°RF	.23
			3.6°RF	—

other parameters which can also affect the cuts, such as bad centering caused by unbalanced dee voltages.

5° FWHM tends to be an easily reproducible, and easily maintainable phase cut at all frequencies. Table 4.1 shows the transmission for these as well as a few other external measurements. 25% to 30% transmission is easily obtainable with these phase cuts.

The best cut to date is shown in Figure 4.9. This is 2.4° FWHM, and it had a 20% transmission when measured just before extraction, (at 39.5 in.) Presumably extracted transmission would be as good, if not better for this beam. One satellite forms a shoulder on the main peak, the rest are practically gone. Cuts like this have been possible on other measurements, but each has required significantly more effort to achieve and maintain than the cuts to 5° FWHM. Smaller cuts, when achieved, have proven to be highly unstable and unreproducable. They also come at a price of low intensities, transmissions are typically $\leq 1\%$.

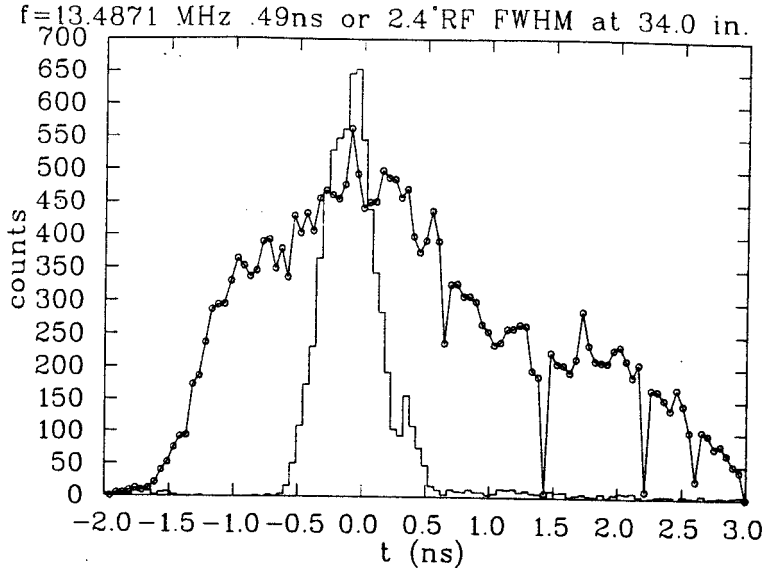

Figure 4.9: The Best Stable Phase Cut.
Internal time spectrum of a cut made to 2.4° FWHM, compared to an uncut spectrum at the same radius. The long flat tail in the cut spectrum consists of real particle signals. The vertical scale, 'counts', has not been scaled to reflect actual currents. The transmitted current with the cuts is 20% of that without cuts. Smaller cuts have been achieved, but as yet none have been found to be stable over time.

4.4 STABILITY

To test the stability of the cuts made with the phase slits, a test was made in a period immediately following a shut down. The cyclotron and the phase slits were tuned. Then the cuts made with the phase slits were followed over a 7 hr period, by taking periodic measurements of the extracted beam time spectra. The result is displayed in Figure 4.10. Figure 4.10(a) tracks the first and second moments of the time spectra, as well as the FWHM of the main peak. No control settings were adjusted in this time period. And at the conclusion of the measurement, no control read outs had changed. The iron yoke is heated by the RF, and is known to warm up after a shutdown. This changes its permeabilty, requiring a fine tuning of the cyclotron by the operators, but the external yoke temperature did not change. (The yoke is cooled externally and the internal temperature can not be measured.)

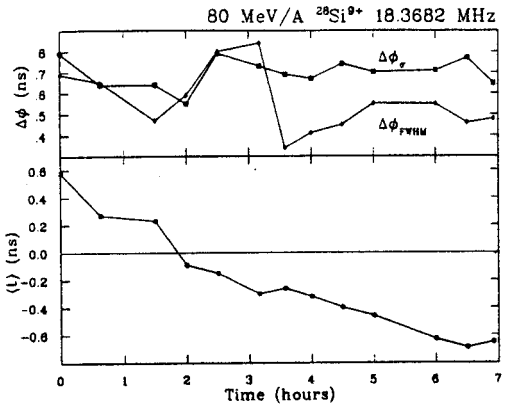

(a) Changes in the First and Second Moments of the Beam Time Spectra.

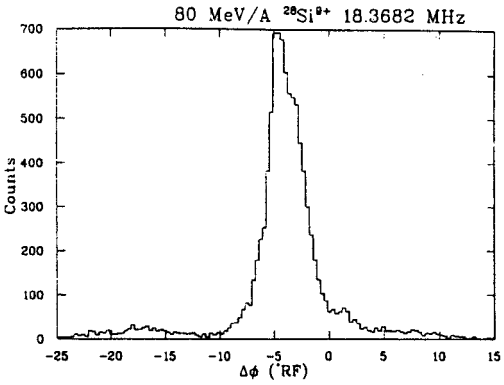

(b) Phase Structure After 5 Hours.

Figure 4.10: A Measurement of Phase Slit Stability.
The structure in time of the extracted cyclotron beam was followed for 7 hours. The centroid experienced a net drift of 1.2 ns. The second moment was relatively stable, but the actual structure drifted, as attested by the rapid fluctuations in the peak width. The peak in Figure 4.10(b) is 3.6° FWHM.

The drift in the first moment was matched by a drift in the uncut spectra, and probably occurred after the phase cuts. This drift is equivalent to a change of 2 parts in 10^5 per turn times the ~800 turns inside the cyclotron. If this drift was caused by heating of the iron yoke, this could be confirmed with NMR measurements at the cyclotron center. Drifts in the centroid can be monitored and corrected for in TOF experiments. The electronics to do this require a time signal from some external detector, were built by Meier, and are currently available for use by the experimenters.

The second moment had small fluctuations, averaging $0.69 \pm .07$ ns, but at the same time, the width of the main peak had much greater variations, averaging $0.57 \pm .16$ ns. These variations are either changes in the phase slit cuts, or the cuts made at extraction. Either way, this implies that the time cuts need to be monitored in the extracted beam.

Experience has shown that the periodic adjustments, needed to retune the cy-

clotron, tend to drift the operating conditions away from the optimum tune. It may sometimes be necessary to search for the optimum, including the extraction system, when maintaining the tune of the phase slits. Changes in the injection line have been known to change the phase cuts, as well as the extraction. The fluctuations had apparently begun to settle down at the end of the stability measurement. If this is true, the amount of retuning should decrease as the temperature stabilizes, and the cyclotron settles in to new operating conditions. External phase measurements could be used by the operators as feedback when making adjustments in the RF frequency and voltage, as well as the magnetic field.

4.5 CONTROLLING PHASE CUTS WITH $\vec{B}(r)$

Equation 1.7, together with Equation 1.6, implies that the magnetic field can be used to improve the phase cuts. It is difficult though to change the phase curve without adversely affecting the orbits. The equation depends on the integral of the phase curve, so it takes a significant change to make a difference at the phase slits.

Figure 4.11(a) shows three phase curves which were developed with the program MONSTER. The solid curve is from the normal operation of the K1200 cyclotron. The location of the phase slits is $\sim$0.03 E/E_{max}. At this location, the dashed curves accumulate lower and higher values of $|\int \sin(\phi) dE|$. These curves were tested in the cyclotron. Each beam was successfully extracted without changing the extraction settings from the normal case. The remaining graphs in Figure 4.11 present cuts using the phase slits for each case. Both slits in the normal case, Figure 4.11(b), leave four peaks in the beam. The phase slits can be adjusted to emphasize one of these peaks, which can be further enhanced over the others by using the buncher. The high case, Figure 4.11(d), works in a similar fashion, except each pin makes

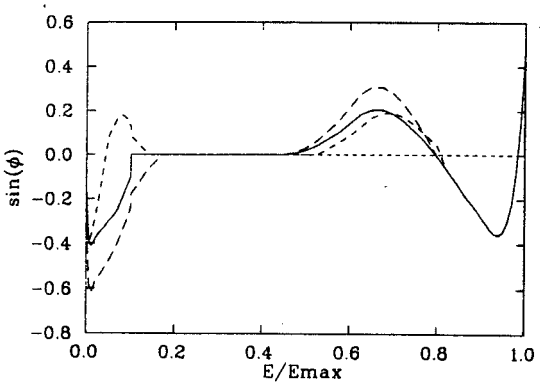

(a) 3 $\sin(\phi)$ Curves. Normal is Solid.

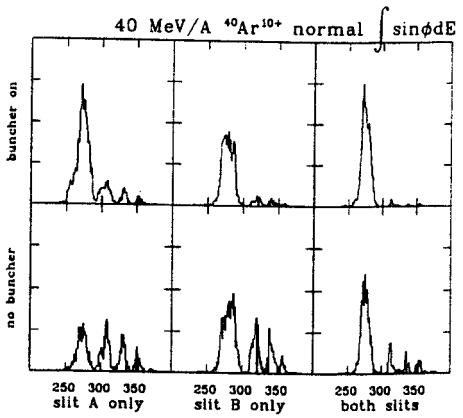

(b) Phase Cuts with Normal $\sin(\phi)$ Curve.

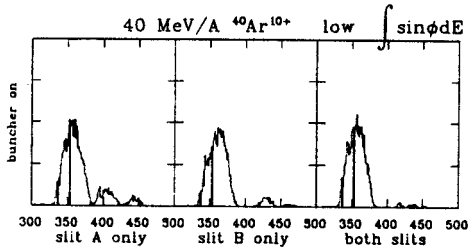

(c) Phase Cuts with Lower $|\int \sin(\phi)dE|$.

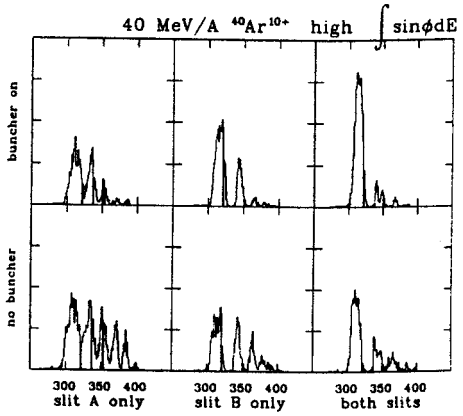

(d) Phase Cuts with Higher $|\int \sin(\phi)dE|$.

Figure 4.11: Controlling Phase Cuts with $B_z(r)$.
Phase cuts were made with the magnetic field set to produce three different phase curves. The width of the phase cuts should be proportional to $|\int \sin(\phi)dE|$, Equation 1.7. Figure 4.11(a) show the three phase curves. The phase slits are at 0.03 E/E_{max}. The smaller dashes are for the low case, and the larger dashes for the high case. Figures 4.11(b) & Figure 4.11(d) show that this equation is true. Figure 4.11(c) straddles $\int \sin(\phi) = 0$, so it is over twice as large as the normal case. The x-axis is channel number measuring $t - t_{RF}$, so smaller channel numbers have a more positive phase.

five peaks, each of which is narrower than those in the normal case. (This is a confirmation of Equation 1.7.) This produces a narrower main peak, but makes it more difficult to eliminate the satellites. The low case, Figure 4.11(c), makes three fatter peaks. The main peak encompasses the particles with maximum energy gain, as well as particles on both sides of the peak energy gain, so it is much wider than the other two cases.

This demonstrates one of the easier methods of obtaining relatively clean phase cuts, so Figure 4.11(b) was recreated in the calculation shown in Figure 4.12. Here the buncher was phased to one side of the acceptance window, then the phase slits were tuned to remove the tail. Comparing the results to those of Figure 4.4, the peak is wider, but the satellites are greatly reduced, making this a cleaner phase cut.

The other easy method of tuning the phase slits is as follows. First, bunch the beam for maximum current. This will place the bunched peak near the center of the acceptance window, like in Figure 4.4. Then scan the transmitted current for each pin individually. Place the pins for maximum transmission, then use the timing detector to fine tune the cuts. This procedure works well for external detectors, and produced the $\sim 5°$ cuts in Figure 4.8.

The discrepancies between the phase slit calculations and measurements could have several simple causes. One would be that the $\sin(\phi)$ curve in the calculation achieves a greater $|\int \sin(\phi) dE|$ than inside the K1200 . This would give fewer, and fatter, peaks in the measurements than in the calculations. At present, these measurements are the closest we can come to measuring $\sin(\phi)$ at this radius. (The Smith–Garren technique, using the 'phase slit probe', which is also at 7.00 in, would require very large frequency changes. Another possibility could be the small differences in the measured and calculated central region acceptance. The calculation

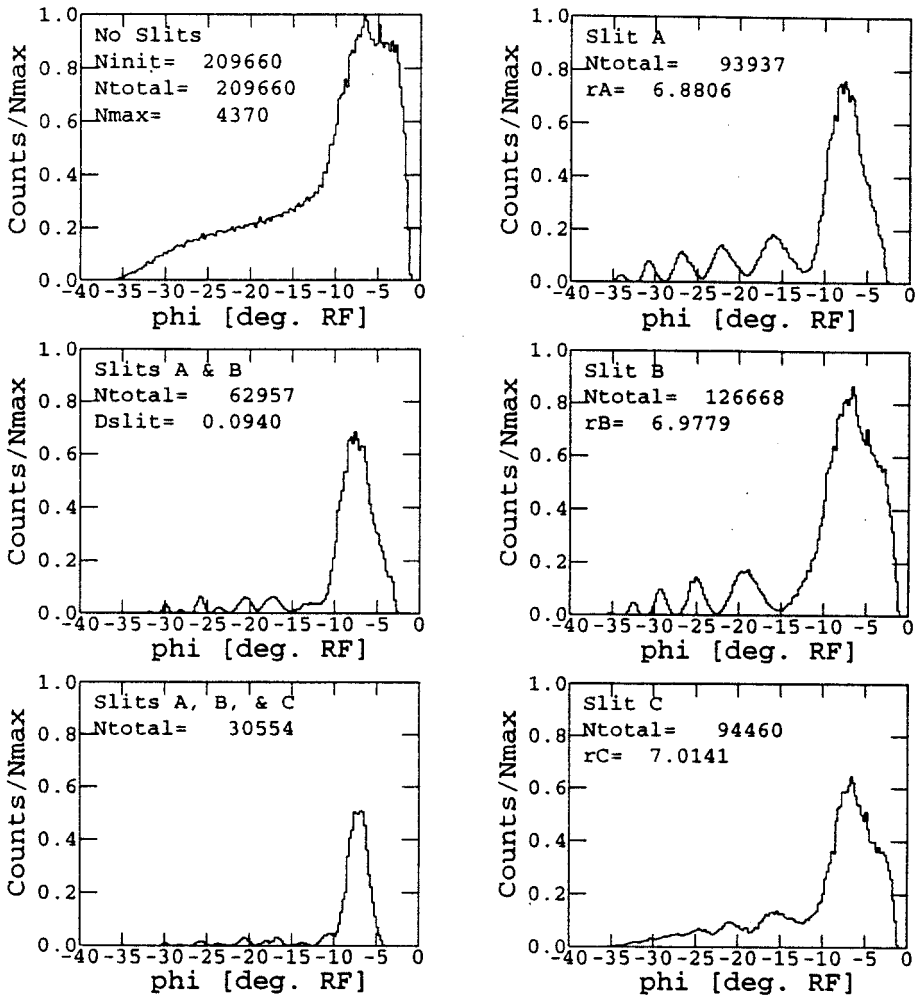

8DKA0:[BAILEY.AXIAL.ALPHA.CENTREG]CRS0B1T225SL4.DAT;1
8DKA0:[BAILEY.AXIAL.ALPHA.CENTREG]CRS0B1T225C.DAT;1

Figure 4.12: Calculation of Cuts Made with the Buncher Tuned to One Edge.
The normal case depicted in Figure 4.11(b) is reproduced by the calculation. This shows that the calculations, while still pessimistic, successfully reproduce the beam conditions at the slits.

has a 45° acceptance window, with small phase space losses, accepting 12% of the injected beam. The measured acceptance is 10%, which means that the acceptance window could be as narrow as 36°. This would also result in fewer peaks in the measurements. It should also be remembered that the calculation used a uniform 100 π mm·mrad initial ellipse. This is an assumption which affects beam spot size and density. A smaller spot, or a spot whose center is denser will make sharper cuts (thinner peaks) which are easier to remove.

CHAPTER 5

EXTRACTION AND PHASE CUTS

One of the purposes of using the phase slits was to achieve single turn extraction, and if not, to improve extraction efficiency. There are many benefits of single turn extraction, clean extraction, narrow spreads in time and energy, etc. Improving the extraction efficiency would still have some benefits: it would reduce the radioactive activation of cyclotron parts, and would increase the total extracted current for beams which are limited by beam current on the electrostatic deflector. This chapter presents the progress made towards these goals, and suggests methods of achieving them.

5.1 SINGLE TURN EXTRACTION

A simple method of estimating if single turn extraction is possible, is to estimate the spread in ϕ which will fill the useable portion of the extraction aperture. With the accelerating frequency and voltage, and the magnetic field tuned so that $\int \sin(\phi) dE = 0$, the radius of the particles follows a cosine curve in ϕ. Then for small ϕ at extraction,

$$r_\phi = r_0 + \Delta r_{ext}(1 - \frac{N\phi^2}{2}), \tag{5.1}$$

where r_0 is the radius before extraction of the central ray with $\phi = 0$, N is the turn number when extraction takes place, and Δr_{ext} is the radius gain between turns N and N-1. The radius will also be modified by the fluctuations in the accelerating voltage. The K1200 voltages are regulated to 1 part in 10^4[61]. This changes the formula to

$$r_\phi = r_0 + \Delta r_{ext}(1 - \frac{N\phi^2}{2} + \frac{N\Delta V}{V}). \tag{5.2}$$

Since the beam has a finite spot size, $\Delta r_{p.s.}$, adjust the septum so that

$$r_t = r_0 + \frac{\Delta r_{p.s.}}{2}. \tag{5.3}$$

Then assuming the deflector aperture is wider than Δr_{ext}, and that no beam is lost on the septum, whose thickness is t, then the minimum possible value of r_ϕ is

$$r_{\phi_{min}} = r_t + t + \frac{\Delta r_{p.s.}}{2}. \tag{5.4}$$

Then solving for ϕ, the phase width must be restricted to

$$|\phi| \leq \sqrt{2\left(\frac{1}{N}(1 - \frac{\Delta r_{p.s.} + t}{\Delta r_{ext}}) - \frac{\Delta V}{V}\right)}. \tag{5.5}$$

In the K1200 , $t = .01$ in., $\Delta r_{ext} \simeq .15$ in., and $N \approx 800$ turns. In the injection calculation for the 'standard beam', the magnetic field started at 700 G, and increased to 36.4 kG. Under these conditions, a beam occupying a circular spot with a 10 mm radius will be reduced to $\Delta r_{p.s.} \approx .11$ in. (That is for a 100 π mm·mrad initial emittance. A 25 π mm·mrad will reduce to a .05 in spot.) Presuming that the beam is not significantly expanded while crossing any resonances, accelerating the beam

will reduce the divergence, but not the spot size. So, for clean single turn extraction, it is necessary to restrict the phases of every surviving particle so that,

$$\begin{aligned} |\phi| &< 1^\circ, \qquad 100\pi \text{ mm} \cdot \text{ mrad} \\ &< 2^\circ, \qquad 25\pi \text{ mm} \cdot \text{ mrad}. \end{aligned}$$

A quicker method is to assume that $\Delta\phi$ occupies no more than 1/4th the energy spacing between turns. Then,

$$|\phi| < \left(\frac{1}{2N}\right)^{\frac{1}{2}} \approx 1.4^\circ \tag{5.6}$$

would be the maximum allowable value of ϕ. These back of the envelope calculations restrict the total spread in phase to 2° to 4° at the base before single turn extraction is possible.

One major restriction remains to be discussed. When Welton first talked about longitudinal space charge[62], he remarked that the leading particles would be accelerated, and the trailing particles decelerated by the electrical repulsion between them. He also suggested that this could be corrected by detuning the RF. Formulas for working with longitudinal space charge within a cyclotron, were first derived and experimentally demonstrated by Gordon at MSU[63]. It does increase the energy spread of the beam but in a non-linear fashion. The particles rotate in a 'vortex' motion. Gordon demonstrated on the K50, that this energy spread can be partially cancelled out by shifting the RF frequency. Adam showed that with sufficient current that the vortex motion will develop into a spiral instability[64]. Joho demonstrated that accelerating cavities operated at high multiples of the accelerating frequency can correct part of the nonlinear spreading[41]. The K1200 is not equipped to do the latter, but can correct the linear portion. This will still leave a spreading in the

energy, and thereby the radius, of the beam at extraction. The net effect of this spreading will be an upper limit on the single turn extracted current, at which the phase cut will need to be narrower than those above.

Further progress towards single turn extraction will be aided by extraction orbit studies which will refine the estimates above. These studies should include space charge calculations. Central region cuts, and magnetic field profiles could then be designed so that the phase slits produce the necessary clean phase cuts. It may also be necessary to restrict the initial emittance. This should also be learned in the extraction studies.

5.2 EXTRACTION MEASUREMENTS

Clearly we have not yet achieved a phase cut where single turn extraction is possible. The best cut, in Figure 4.9, has a base of 6° and a few particles are even further from the peak. If the extraction were tuned properly, it should be possible to improve the extraction efficiency by using this peak.

The first extraction measurement using the slits seemed to confirm this, with the extraction efficiency improving from 45% to 65%, when comparing the current measured on the 1 finger probe in the A2 drive at 39.5 in with that measured by the same probe in the extraction channel. Outside the cyclotron, on the A-012 Faraday cup, the efficiency improved from 35% to 55%. For a beam that is limited by losses on the deflector[65], an improvement in the extraction efficiency can increase the total current extracted. In the case of this extraction measurement, assuming a 20% transmission through the phase slits, the extracted beam could be increased by 240%, provided that the injected current could be increased by 780%. For experiments where high intensities are not needed, (most of the 4π

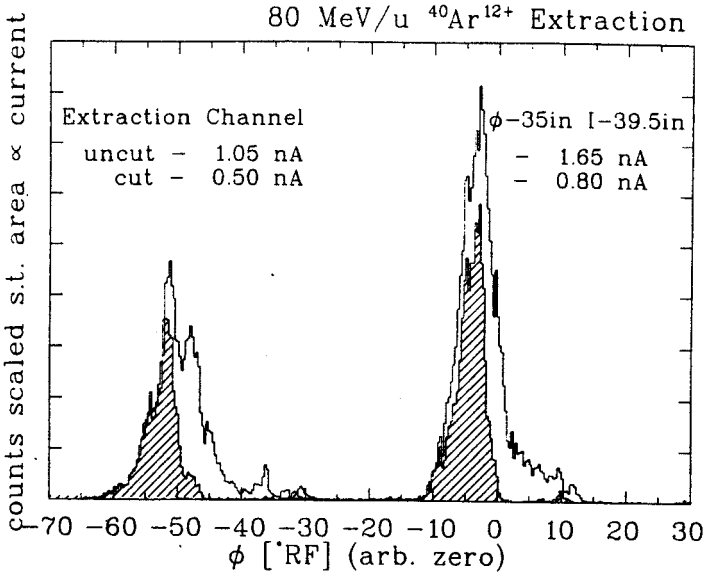

Figure 5.1: Phase Spectra from the Extraction Measurement.
An extraction measurement was made where both the cut and uncut beams had ~65% extraction efficiencies. The phase spectra of this measurement are displayed above, measured in the extraction channel, and at 35 in. The shaded peaks are with the phase slit cuts. Amazingly, the uncut beam was bunched to 6.4° FWHM, thus it could be extracted at an efficiency comparable to that of cut beams. The cut beam is 3.6° FWHM.

nuclear physics detectors,) using the slits will reduce the activation of the extraction elements, (often the 'hottest' parts when the cyclotron is opened.)

This initial success was confused by the second extraction measurement. After examining how various controls affected extraction, a very careful search found settings where the uncut bunched beam had a 65% extraction comparing 39.5 in to the extraction channel. Using the phase slits could not improve this efficiency. The external efficiency, though, was only 35% in both cases. (The magnetic channels were left alone, and may not have been optimized.) The first measurement was with 40 MeV/u $^{40}Ar^{10+}$, and used the cut and uncut beams in Figure 4.9. The second was on 80 MeV/u $^{40}Ar^{12+}$, and is shown in Figure 5.1. This result contradicts the idea that phase cuts can always improve the extraction efficiency. A closer look though shows that the uncut beam was bunched to 6.4° FWHM. It was extracted at a 65% efficiency because it was already very narrow in phase. 65% seems to be

the present limit. This could possibly be from transverse spot size. As with the single turn extraction, improvements should come with smaller beam emittances, and narrower phase cuts.

For practical purposes, when a beam is limited by losses on the deflectors, a measurement of the extraction efficiency should be made. If the efficiency measured with the A2 probe is significantly less than 65%, and the source can provide currents that are an order of magnitude, or more, higher, then the phase slits should be used to increase the total extracted current. Caution is advised when using the A5 probe for the current measurements. It intercepts the extraction channel at a greater radius, and the beam passes several extraction elements between the two probes. Presuming that there is no calibration problem between the 1 finger probe, and the A-012 Faraday cup, the beam will suffer losses after the A2 probe, some of which may occur between the two probes. So the maximum extraction efficiency may be lower on the A5 drive than on the A2 drive.

CHAPTER 6

SUMMARY, CONCLUSIONS, AND RECOMMENDATIONS

Phase slits have been introduced into the K1200 cyclotron which are capable of producing narrow peaks in time, FWHM of 3° to 5° RF, with a few particles from times outside the peak which can always get past the slits. The processes by which these phase slits cut the beam are clearly understood, with calculations that are capable of reproducing the details found in the measurements. These cuts are capable of improving the extraction efficiency, and while not yet sufficient for single turn extraction, the improvements outlined below should make this possible.

A detector has also been designed and deployed in the K1200 which is capable of measuring the time spectra inside the cyclotron. It has a resolution of 200-300 ps. 200 ps is 2° RF at 27 MHz, our maximum operating frequency, and 300 ps is 2° RF at 18 MHz. This resolution will aid in obtaining the $\pm 1°$ cuts necessary for single turn extraction. While this detector measures only at extremely low intensities, these measurements can still be used to measure the time cuts which will be necessary for single turn extraction in preparation for when space charge is introduced. This detector can also be used to measure time processes in the beam as it is accelerated to different radii, as well as the $\sin(\phi)$ curve inside the cyclotron. It is limited, though, to the outer 8 in, and use with heavier ions.

Even though a cyclotron's acceptance is defined mostly by apertures, and not

stability regions, the stability regions still define the shape of the optimum injected ellipse. This study has found that matching the injected ellipse reduces the size of the beam core as well as that of the beam halo. Furthermore, it reduces the debunching of the beam, in time, incurred when traversing the yoke and the spiral inflector, which increases the amount of current which can be bunched into the peak selected by the phase slits. It will also minimize distortions produced in the vertical phase space of the beam at injection, as well as minimize the correlations induced by the inflector.

The focussing solenoid in the axial injection line is also of great importance in injecting the beam. Its main function is to maximize the initial acceptance of the spiral inflector. Without it, the calculations showed a possible reduction of almost 50% in the injected current. Like matching the injected ellipses, the focussing solenoid can be used to minimize the debunching in the yoke and the spiral inflector, and the distortions in the injected vertical phase space. Also, it reduces the blow up in the beam incurred as the injected beam crosses the non-adiabatic regions in the yoke. Using the solenoid, though, exacts the price of a larger internal beam spot.

Together, focussing with the solenoid, and matching the injected beam will greatly improve the cyclotron beam, improving the performance of the buncher and the phase slits, as well as aiding in traversing resonances and extracting the beam. Our present inability to do these things is a handicap which when overcome will enhance the performance of the K1200 cyclotron.

The present work has shown that the most important improvement needed to produce clean cuts, as well as narrower cuts, is a central region slit. The effectiveness of the slits is presently hampered by the large number of turns needed for the beam to clear the slits. Using a central region slit to introduce an initial cut which will produce separated turns at the phase slits will free the slits from the task of

minimizing the satellites, allowing them to be used in optimizing the phase cut. It will also allow the use of the specially designed magnetic fields which enhance the effectiveness of the phase slits.

Some effort should also be directed towards finding and producing an optimum initial emittance for injection into the cyclotron. This study started with the beam at the ECR, where it is extracted with a large emittance, 50-400 π mm·mrad . It next looked at the inflector which may accept as much as 170 π mm·mrad , but which clearly accepts most of 100 π mm·mrad . It followed the beam from the inflector, through the central region, to the slits, which make cleaner cuts in time when cutting smaller emittances. It then looked at the deflector, where the maximum radius gain is .15 in. A 170 π mm·mrad initial emittance will produce a .14 in diameter beam spot. The reduction in size achieved by using superconducting magnets is also reducing the optimum beam size at these critical points. Depending upon ones needs, i.e. single turn extraction, much of the beam from the source may need to be discarded. But this reduces the beam current. A reduced beam size during injection will also eliminate the particles which suffered greater debunching in the yoke and spiral inflector, effectively enhancing the performance of the buncher. All of this will need to be quantified in order to optimize transmission when single turn extraction is achieved.

BIBLIOGRAPHY

[1] H.G. Blosser et al. Advances in superconducting cyclotrons at MSU. In *Proc. of the 11th Intl. Cyclotron Conf.*, pages 157–167, Ionics, Tokyo, 1986.

[2] J.A. Nolen et al. Commissioning experience with the NSCL K1200 superconducting cyclotron. In *Proc. of the 12th International Conference on Cyclotrons*, pages 5–8, Berlin, 1989.

[3] P. Miller et al. Peformance of the K1200 cyclotron at MSU. In *Proceed. of the 13th Intl. Conf. on Cyclotrons*, pages 86–89, Vancouver, BC, 1993.

[4] MSU/NSCL. Beamlist, March 1993.

[5] P. Miller. Annual Report, MSU/NSCL, 1994.

[6] B.F. Milton et al. Design of a beam phase measurement and selection system for the MSU K500 cyclotron. In *Proc. 10th Intl. Conf. on Cyclotrons and Their Applications*, pages 55–58, IEEE, New York, 1984.

[7] B.F. Milton et al. A gamma ray probe for internal beam phase measurements. In *Proc. 11th Intl. Conf. on Cyclotrons and Their Applications*, pages 468–469, Ionics, Tokyo, 1986.

[8] B.F. Milton. *Phase Selection in the K500 Cyclotron and the Development of a Non-Linear Transfer Matrix Program.* PhD thesis, Michigan State University, 1986.

[9] F. Marti and A. Gavalya. Axial injection in the K500 superconducting cyclotron. In *Proc. of the 11th Intl. Cyclotron Conf.*, pages 484–487, Ionics, Tokyo, 1986.

[10] L.H. Harwood et al. Magnetic field measurements of the NSCL K500 cyclotron magnet. In *Proc. 11th Intl. Conf. on Cyclotrons and Their Applications*, pages 315–317, Ionics, Tokyo, 1986.

[11] L.H. Harwood et al. Beam extraction from the NSCL K800 cyclotron. In *Proc. 11th Intl. Conf. on Cyclotrons and Their Applications*, pages 473–475, Ionics, Tokyo, 1986.

[12] D. Poe, 1994. private communication.

[13] H.G. Blosser. Optimisation of the cyclotron central region for the nuclear physics user. In *Fifth Intl. Cyclotron Conf.*, pages 257–273, Butterworths,London, 1971.

[14] H.G. Blosser. Problems and performance in the cyclotron central region. *IEEE Trans. Nucl. Sc.*, NS-13(4):1–14, 1966.

[15] S.J. Burger et al. On the design of the central region of an 8 MeV injector cyclotron. In *Proc. 10th Intl. Conf. on Cyclotrons and Their Applications*, pages 67–70, IEEE, New York, 1984.

[16] M.M. Gordon. Single turn extraction. *IEEE Trans. Nucl. Sc.*, NS-13(4):48–53, 1966.

[17] E. Kashy G.F. Trentelman and R.K. Jolly. High resolution nuclear studies using cyclotron beams. In *Fifth Intl. Cyclotron Conf.*, pages 380–387, Butterworths,London, 1971.

[18] D. Clark. Beam diagnostics and instrumentation. *IEEE Trans. Nucl. Sc.*, NS-13(4):15–23, 1966.

[19] L. Rezzonico. Beam diagnostics at SIN. In *Proc. 11th Intl. Conf. on Cyclotrons and Their Applications*, pages 457–460, Ionics, Tokyo, 1986.

[20] F. Loyer. On line beam diagnostics at GANIL. In *Proc. 11th Intl. Conf. on Cyclotrons and Their Applications*, pages 449–452, Ionics, Tokyo, 1986.

[21] T. Itahashi et al. Beam diagnostics in the RCNP ring cyclotron. In *Proc. 13th Intl. Conf. on Cyclotrons and Their Applications*, pages 491–494, World Scientific,Singapore, 1993.

[22] W.R. Rawnsley et al. The production and measurement of 150 ps beam pulses from the TRIUMF cyclotron. In *Proc. 10th Intl. Conf. on Cyclotrons and Their Applications*, pages 237–240, IEEE, New York, 1984.

[23] J.C. Collins. *Phase Selection Mechanisms in Isochronous Cyclotrons Producing High Resolution Beams.* PhD thesis, Michigan State University, 1973.

[24] M.M. Gordon and F. Marti. Radial-longitudinal coupling in cyclotrons and focusing complementarity. *Particle Accelerators*, 12:13–26, 1982.

[25] M.M. Gordon. The electric gap crossing resonance in a three sector cyclotron. In *Proc. of the International Conference on Sector-Focused Cyclotrons*, pages 268–280, 1962.

[26] B.F. Milton et al. A cyclotron orbit code using second order transfer matrices. In *Proc. 11th Intl. Conf. on Cyclotrons and Their Applications*, pages 240–243, Ionics, Tokyo, 1986.

[27] R.M. Ronningen et al. Test of an avalanche diode as a detector for measuring beam phase width. Annual Report, MSU/NSCL, 1988.

[28] D. Johnson. Technical Report MSUCP-44, MSU/NSCL, 1985. unpublished.

[29] E. Fabrici, D. Johnson, and F.G. Resmini. The extraction system for the K500 cyclotron at MSU. *Nucl. Instruments and Methods*, 184:301, 1981.

[30] G. Bellomo et al. Magnetic field mapping of the K500 cyclotron at MSU. *Nucl. Instruments and Methods*, 180:285, 1981.

[31] G. Bellomo. Final design of the K800 magnetic field. Technical Report MSUCP-35, MSU/NSCL, 1981. unpublished.

[32] R. Baartman and W. Kleeven. A canonical treatment of the spiral inflector for cyclotrons. Technical Report TRI-PP-93-8, TRIUMF, Feb. 1993. preprint to Particle Accelerators.

[33] F. Marti and S. Snyder. Internal beam dynamics studies with a TV probe. In *Proceedings of the 13th Intl. Conf. on Cyclotrons*, Vancouver,BC, 1993.

[34] F. Marti, R. Blue, J. Kuchar, J.A. Nolen, B. Sherrill, and J. Yurkon. A CCD camera probe for a superconducting cyclotron. In *Proceedings of the 1991 IEEE Particle Accelerator Conference*, pages 1163–1165, San Francisco, 1991.

[35] J. Bailey et al. Selection and measurement of RF phase width of the K1200 cyclotron beam. In *Proc. 13th Intl. Conf. on Cyclotrons and Their Applications*, pages 431–434, World Scientific,Singapore, 1993.

[36] F. Marti, J. Griffin, and V. Taivassalo. Design of the axial injection system for the NSCL cyclotrons. *IEEE Transactions on Nuclear Science*, NS-32:2450–2452, 1985.

[37] Z.Q. Xie. *The Effect of Space Charge Force on Beams Extracted from ECR Ion Sources.* PhD thesis, MIchigan State University, East Lansing, MI 48824, September 1989.

[38] T.A. Antaya. Nonlinear beam transport effects in highly charged positive ion beams extracted from ECR ion sources. In *Proc. of the Intl. Workshop on Nonlinear Problems in Accelerator Physics*, pages 97–112, Institute of Physics, London, 1993.

[39] D. Cole et al. ECR operation summary. Annual Report, MSU/NSCL, 1990.

[40] H.G. Blosser and M.M. Gordon. Performance estimates for injector cyclotrons. *Nuclear Instruments and Methods*, 13:101–117, 1961.

[41] W. Joho. Space charge effects in cyclotrons. Presented at the Int. Accelerator School, Dubna, USSR, September 1988.

[42] J.L. Belmont and J.L. Pabot. Study of axial injection for the Grenoble cyclotron. *IEEE Trans. Nucl. Sc.*, NS-13:191–193, 1966.

[43] F. Marti and A. Gavalya. Axial injection in the K500 superconducting cyclotron. In *Proc. 11th Intl. Conf. on Cyclotrons and Their Applications*, pages 484–487, Ionics, Tokyo, 1987.

[44] L.H. Harwood et al. Analysis and transport of beams from the ECR ion source to the NSCL K500 and K800 cyclotrons. In *Proc. 11th Intl. Conf. on Cyclotrons and Their Applications*, pages 488–490, Ionics, Tokyo, 1986.

[45] L.H. Harwood. Status of integrated software project for cyclotron design. Annual Report, MSU/NSCL, 1986.

[46] K. Halbach and R.F. Holsinger. unpublished.

[47] A.M. Winslow. Numerical solution of the quasilinear poisson equation in a nonuniform triangular mesh. *Joural of Computational Physics*, 2:149–172, 1967.

[48] Computer program POISSON. Technical Report LA-UR-87-126.9, Los Alamos National Lab.

[49] H. Houtman and C.J. Kost. A Fortran Program (RELAX3D) to solve the 3-D Poisson (Laplace) Equation. In *Proc. of the Europhysics Conference, Computing in Accelerator Design and Operation*, pages 98–103, Berlin, 1983. Springer Verlag, Lect. Notes in Physics 215.

[50] F. Marti, M.M. Gordon, M.B. Chen, C. Salgado, T. Antaya, and E. Liukkonen. Design calculations for the central region of the NSCL 500 MeV superconducting cyclotron. In *Proc. 9th Intl. Conf. on Cyclotrons and Their Applications*, pages 465–468, Caen, France, 1981.

[51] D.R. Nicholson. *Introduction to Plasma Theory*, chapter 2. Single Particle Motion, pages 20–23. John Wiley & Sons, New York, 1983.

[52] F.J. Lynch et al. Beam buncher for heavy ions. *Nuclear Instruments and Methods*, 159:245, 1979.

[53] R.M. Ronningen et al. Phase probe tests. Annual Report, MSU/NSCL, 1986.

[54] G.F. Knoll. *Radiation Detection and Measurement*, chapter 11. Semiconductor Diode Detectors. John Wiley & Sons, New York, 1979.

[55] S. Cheng et al. Branching ration for the m1 decay of the 2 $^2s_{1/2}$ state in one–electron krypton. *Phys. Rev.*, A47:903, 1993.

[56] Garren and Smith. Diagnosis and correction of beam behavior in an isochronous cyclotron. In *Intl. Conf. on Sector Focused Cyclotrons and Meson Factories*, Cern, 1963.

[57] F. Marti et al. A CCD camera probe for a superconducting cyclotron. In *Conf. Record of the 1991 IEEE Particle Accelerator Conf.*, pages 1163–1165, IEEE, New York, 1991.

[58] F. Marti et al. Beam diagnostics developments at NSCL. In *Proc. of the 12th International Conference on Cyclotrons*, pages 268–277, Berlin, 1989.

[59] J.A. Winger et al. *Nuclear Instruments and Methods*, B70:380, 1992.

[60] H. Spieler. Fast timing methods for semiconductor detectors. *IEEE Trans. Nucl. Sc.*, NS-29(3):1142–1157, 1982.

[61] R.E. Laxdal. Lists of cyclotrons and cooler-booster rings. In *Proc. 13th Intl. Conf. on Cyclotrons and Their Applications*, pages 771–935, World Scientific,Singapore, 1993.

[62] T.A. Welton. Factors affecting beam quality. *Nucl. Sci. Ser. Report No. 26*, (NAS-NRC-656):192–198, 1959.

[63] M.M. Gordon. The longitudinal space charge effect and energy resolution. In *Fifth Intl. Cyclotron Conf.*, pages 305–317, Butterworths,London, 1971.

[64] S. Adam. Calculation of space charge effects in isochronous cyclotron. In *Proc. of the 1985 IEEE Particle Accelerator Conference*, Vancouver, 1985. Poster U43.

[65] T. Antaya. K1200 cyclotron deflector development. Annual Report, MSU/NSCL, 1992.